

2D DYNAMIC STALL SIMULATIONS WITH TIME-VARYING FREESTREAM  
REPRESENTATIVE OF HELICOPTER FLIGHT

by

Daniel J. M. Gosselin

A thesis submitted to the Faculty of Graduate and Postdoctoral Affairs  
in partial fulfilment of the requirements for the degree of

Master of Applied Science

in Aerospace Engineering

Ottawa-Carleton Institute for Mechanical & Aerospace Engineering

Department of Mechanical & Aerospace Engineering

Carleton University

Ottawa, Ontario, Canada

© Daniel J. M. Gosselin

September 2014

# Abstract

Dynamic stall of helicopter rotor blades occurs predominantly on the retreating rotor blade in high-speed forward flight. It occurs at very fast (or dynamic) change of the angle of attack of an airfoil, leading to lift, drag and pitching moment loads greatly exceeding those at slow (or quasi-steady) changing of angle of attack. The aerodynamic loads generated during dynamic stall are a major source of blade vibration, such that their magnitude limits the forward flight speed of a helicopter. Due to the very nature of rotorcraft flight, dynamic stall occurs at time-varying freestream on helicopter main rotors. However, due to the difficulties in reproducing a time-varying freestream experimentally or computationally, current dynamic stall models used in the industry neglect the unsteady nature of the freestream. This thesis examined the influence of unsteady freestream on the mechanism of dynamic stall and aimed to determine whether time-varying freestream effects are important for predicting dynamic stall loads for helicopter applications.

Two test cases were compared using two-dimensional unsteady Reynolds-averaged

Navier-Stokes computational fluid dynamics simulations. The first case represented dynamic stall simulation of the “classical” steady freestream condition and was used for validation purposes against experimental results. The second case represented a dynamic stall simulation with time-varying freestream reflecting actual helicopter flight, by changing the inlet velocity boundary condition as a function of time. Both cases featured 15 degrees mean angle of attack with oscillations of 10 degrees of amplitude. The freestream Mach number for the first case was 0.29, whereas for the varying freestream it was varying between Mach 0.18 – 0.78.

The variable freestream was observed to have had a qualitative influence on the dynamic stall mechanism, by exhibiting transonic effects and flow separation even at angles of attack below the static stall angle of attack, as well as delaying stall to later azimuth angles and enhancing the influence of the trailing-edge vortex. Quantitative changes were also present, increasing the lift, drag and pitching moment substantially with respect to the steady freestream case. Some of these effects were attributed the difference in Mach number, Reynolds number and reduced frequency at the extremes of the pitch oscillation. However new features to the overall mechanism of dynamic stall were also observed, suggesting that the time-varying nature of the freestream is an important factor in modelling dynamic stall for helicopter aeromechanics purposes.

*Dedicated to my wife*

*Chantelle*

# Acknowledgements

I would like to acknowledge my thesis advisor, Dr. Daniel Feszty, for his support and encouragement throughout the course of the present work.

There were many researchers, namely Kobra Gharali, Peter Gerontakos, Guillaume Martinat, Louis Gagnon who were kind enough to correspond with me about their work, which became the foundation of my own.

I would also like to thank the OpenFOAM community, without whom the use of this software would not have been possible. The documentation of this software is very limited, as is the number of people with experience using it, and as a result new users are heavily dependent on the kindness of strangers on the message boards to decipher how to use the software. To the numerous anonymous users who assisted me: I hope that I can in turn pay it forward with the knowledge I have gained.

Many thanks to Neil McFadyen for setting up a cluster for my cases to run remotely, and Nancy Powell for her assistance throughout the duration of this degree.

I also wish to acknowledge the financial support of the Department of National

Defence which provided funding for the coursework element of this degree.

Finally I wish to recognize the unconditional support of my family, especially my wife Chantelle. Without her support and understanding, this work would not have been possible.

# Table of Contents

<b>Abstract</b>	<b>ii</b>
<b>Acknowledgements</b>	<b>v</b>
<b>List of Tables</b>	<b>xii</b>
<b>List of Figures</b>	<b>xiv</b>
<b>Nomenclature</b>	<b>xx</b>
<b>Chapter 1 Introduction</b>	<b>1</b>
1.1 Rotorcraft Aerodynamics.....	1
1.1.1 Helicopters in Hovering Flight.....	2
1.1.2 Helicopters in Forward Flight.....	4
1.1.3 Rotor Control.....	6
1.2 Static and Dynamic Stall.....	9
1.2.1 Static Stall.....	10

1.2.2	Dynamic Stall.....	11
1.2.3	Dynamic Stall: the State of the Art.....	17
1.3	Thesis Objectives.....	18
<b>Chapter 2 Background and Literature Review</b>		<b>20</b>
2.1	Mechanisms of Formation of Dynamic Stall.....	21
2.2	Stall Flutter.....	25
2.3	Factors Influencing Dynamic Stall.....	28
2.3.1	Geometric Similitude.....	28
2.3.2	Dynamic Similitude.....	34
2.3.3	Kinematic Similitude.....	37
2.3.4	Fluidelastic Similitude.....	49
2.4	Numerical Modelling of Dynamic Stall.....	50
2.4.1	Comprehensive Rotor Analysis.....	50
2.4.2	Theoretical and Semi-Empirical Approaches.....	51
2.4.3	Navier-Stokes Solutions.....	55
2.5	Summary of Literature Review and Motivation for Research.....	58
<b>Chapter 3 Numerical Method</b>		<b>61</b>
3.1	Test Cases.....	61
3.2	OpenFOAM.....	64
3.3	Governing Equations.....	66
3.3.1	Conservation and Auxiliary Equations.....	66

3.3.2	Turbulence Modelling.....	69
3.4	Solution Method.....	74
3.4.1	Discretization Schemes.....	74
3.4.2	Solver Algorithm.....	79
3.4.3	Solution of Discretized Equations.....	79
3.5	Computational Setup.....	80
3.5.1	Computational Domain.....	81
3.5.2	Boundary Conditions.....	82
3.5.3	Physical Properties.....	87
3.5.4	Spatial Discretization.....	89
3.5.5	Parallel Processing.....	92
3.5.6	Temporal Discretization.....	94
3.5.7	Solution Convergence.....	96
3.6	Solution Fidelity.....	96
3.6.1	Verification.....	97
3.6.2	Validation.....	98
3.7	Post-Processing and Data Reduction.....	100
3.7.1	Flow Visualization.....	102
3.7.2	Data Reduction.....	102
<b>Chapter 4 Results</b>		<b>108</b>
4.1	Steady Freestream Case.....	108
4.1.1	Boundary Conditions.....	109

4.1.2	Convergence.....	110
4.1.3	Aerodynamic Loads.....	110
4.1.4	Mechanism of Dynamic Stall at Steady Freestream.....	113
4.2	Time-Varying Freestream Velocity Case.....	120
4.2.1	Boundary Conditions.....	120
4.2.2	Convergence.....	123
4.2.3	Aerodynamic Loads.....	123
4.2.4	Mechanism of Dynamic Stall at Variable Freestream.....	128
4.2.5	Comparison of Steady and Variable Freestream Mechanisms....	136
<b>Chapter 5 Conclusions and Recommendations</b>		<b>147</b>
5.1	Conclusions.....	147
5.2	Recommendations for Future Work.....	150
<b>References</b>		<b>152</b>
<b>Appendix A OpenFOAM Input Files</b>		<b>170</b>
A.1	Contents of File vin.dat.....	172
A.2	Contents of File \0\k.....	173
A.3	Contents of File \0\omega.....	174
A.4	Contents of File \0\mut.....	175
A.5	Contents of File \0\p.....	176
A.6	Contents of File \0\T.....	177
A.7	Contents of File \0\U.....	178

A.8	Contents of File \0\rho.....	179
A.9	Contents of File \constant\RASProperties.....	180
A.10	Contents of File \constant\thermodynamicProperties.....	181
A.11	Contents of File \constant\thermophysicalProperties.....	182
A.12	Contents of File \constant\transportProperties.....	183
A.13	Contents of File \constant\turbulenceProperties.....	184
A.14	Contents of File \constant\polyMesh\blockMeshDict.....	185
A.15	Contents of File \system\controlDict.....	189
A.16	Contents of File \system\decomposeParDict.....	190
A.17	Contents of File \system\fvSchemes.....	191
A.18	Contents of File \system\fvSolution.....	192
A.19	Contents of File \system\sampleDict.....	193

**Appendix B Flow Visualization Animations** **194**

# List of Tables

Table 2.1: Relative importance of parameters affecting dynamic stall, adapted from McCroskey et al. (1976).....	29
Table 2.2: Summary of test conditions for variable freestream investigations.....	49
Table 3.1: Test case conditions.....	63
Table 3.2: k- $\omega$ SST turbulence model constants.....	72
Table 3.3: k- $\omega$ SST turbulence model boundary condition values.....	74
Table 3.4: Summary of discretization schemes selected within OpenFOAM for the simulations of this thesis.....	80
Table 3.5: Summary of Solution Methods.....	81
Table 3.6: Initial and boundary conditions applied. The constants indicated by the symbols in this table are provided for each case in Table 3.7.....	83
Table 3.7: Boundary and initial conditions: constants.....	83
Table 3.8: Thermophysical model.....	88
Table 3.9: Thermophysical constants.....	89
Table 3.10: Mesh data.....	92

Table 4.1: Comparison of CFD results to experimental data, both for the steady freestream case. Arrows next to the angles of attack indicate upstroke or downstroke.....	113
Table 4.2: Comparison of variable freestream CFD results to steady freestream experimental data. Arrows next to angle of attack figures indicate upstroke or downstroke.....	126
Table A.1: List of files and folder structure for the variable freestream OpenFOAM case. .....	171

# List of Figures

Figure 1.1: (a) Top-view of rotor blades showing the distribution of incident velocity as a function of azimuth in hovering flight, adapted from Leishman (2006). (b) Side view of rotor shaft and blades showing coning angle and tip path plane.	3
Figure 1.2: Top-view of rotor blades showing the distribution of incident velocity as a function of azimuth in forward flight, with notional values for the tip and forward speeds. Adapted from Leishman (2006).....	4
Figure 1.3: Regions of reverse flow and compressibility effects. Reproduced from Leishman (2006).....	6
Figure 1.4: Diagram of flapping, feathering and lead-lag motions on a rotor blade. Reproduced from Leishman (2006).....	8
Figure 1.5: Diagram of an articulated hub, reproduced from FAA (2008).....	9
Figure 1.6: Boundary layer of NACA 0012 airfoil between 6 degrees AOA and static stall angle, reproduced from Gerontakos (2008).....	10
Figure 1.7: Airflow in the vicinity of a laminar separation bubble, reproduced from Ward (1963).....	11

Figure 1.8: UH-60 dynamic stall rotor map. Points on map indicate convection of LEV past the rotor blade mid-chord. Quadrants are numbered 1-4 counter-clockwise from the 0-90° azimuth range which is quadrant 1. Adapted from Bousman (1998).....	13
Figure 1.9: Comparison of reverse flow conditions on (a) static and (b) unsteady airfoils. Reproduced from Carr et al. (1977).....	14
Figure 1.10: Helicopter design constraints on forward speed and main rotor tip speed. Adapted from Leishman (2006).....	16
Figure 2.1: Dynamic Stall Events on the NACA 0012 Airfoil. Reproduced from Carr et al. (1977).....	21
Figure 2.2: Frequency induced camber, reproduced from Ericsson and Reding (1972)..	22
Figure 2.3: Unsteady airloads at various depths of dynamic stall, $M = 0.3$ , $\alpha = \alpha_0 + 10^\circ \cos \Omega t$ , $k = 0.1$ . $\alpha_0 = 4^\circ, 5^\circ$ and $10^\circ$ for the stall onset, light stall and deep stall plots, respectively. Reproduced from McCroskey (1982). The solid line indicates the upstroke, the dashed line indicates the downstroke, and the dotted line is static airfoil data.....	27
Figure 2.4: Comparison of (a) model rotor and (b) UH-60A rotor blade movement to ramp and sinusoidal rotation. Reproduced from (a) McCroskey and Fisher (1972) and (b) Kerho (2007).....	41
Figure 2.5: (a) Plunging and (b) pitching airfoil motion, reproduced from Leishman (2006).....	42
Figure 3.1: Variation of freestream magnitude and angle of attack as a function of	

azimuth for Case 2. Top image: solid lines indicates angle of attack, dashed line indicates freestream speed. Second and third images: solid lines indicate data at the airfoil, dashed lines indicate data at the inlet.....	65
Figure 3.2: Variation of freestream magnitude and angle of attack as a function of azimuth for Case 1. Top image: solid lines indicates angle of attack, dashed line indicates freestream speed. Second and third images: solid lines indicate data at the airfoil, dashed lines indicate data at the inlet.....	65
Figure 3.3: Computational domain, patches and domain size indicated.....	82
Figure 3.4: Layout of blocks that form the mesh.....	90
Figure 3.5: Layout of blocks that form the mesh. The sizes of blocks 1-3, 7 & 8 are exaggerated to illustrate the layout.....	90
Figure 3.6: Computational mesh.....	93
Figure 3.7: Computational mesh: zoom on airfoil.....	93
Figure 3.8: Computational mesh: zoom on leading edge boundary layer resolution.....	93
Figure 3.9: Decomposition of domain into four sub-domains for parallel processing using Scotch.....	94
Figure 3.10: Mesh independence results, NACA0012 airfoil at Mach 0.30, Reynolds Number $6.1 \times 10^6$ , $k = 0$ and angle of attack $9.0^\circ$ . Experimental data from Ladson et al. (1987).....	98
Figure 3.11: Timestep independence comparison of (a) lift, (b) pitching moment and (c) drag results, Case 1.....	99
Figure 3.12: $C_p$ vs $x/c$ , NACA0012 airfoil at Mach 0.30, Reynolds Number $6.1 \times 10^6$ , and	

angle of attack $13.0^\circ$ . Experimental data from Ladson et al. (1987).....	100
Figure 3.13: Coefficient of (a) lift, (b) pitching moment and (c) drag versus angle of attack for static angle of attack, NACA 0012 airfoil, Mach 0.3, Reynolds number $5.93 \times 10^6$ . Experimental data from Ladson (1988).....	101
Figure 4.1: Vector plot showing boundary conditions at high angle of attack, $233^\circ$ azimuth.....	109
Figure 4.2: Time-history of aerodynamic loads, steady freestream case (Case 1). Each cycle begins at $154^\circ$ azimuth at the airfoil.....	111
Figure 4.3: Comparison of (a) lift, (b) pitching moment and (c) drag coefficients from quasi-steady and dynamic experimental results from McAlister et al. (1982) as well as of CFD results of this work. The flow conditions correspond to $M = 0.301$ , $Re = 3.91 \times 10^6$ and $\alpha = 15^\circ \pm 10^\circ$ . Quasi-static results are shown for a slow ramp-up in angle of attack between 5 and 20 degrees.....	112
Figure 4.4: Positions of images in Figure 4.5 indicated on coefficient of (a) lift and (b) pitching moment coefficient CFD results for Case 1. Solid line indicates upstroke, dashed line indicates downstroke. (c) Azimuthal positions of images in Figure 4.5. Dashed line is speed, solid line is angle of attack.....	114
Figure 4.5: Velocity vector plots and pressure contours (left column) and Mach contours and streamline plots (right column), rows corresponding to points indicated in Figure 4.4 respectively. Pressure contours show a minimum of 25 kPa, a maximum of 120 kPa, with 76 contours at intervals of 1.25 kPa. Mach contours show a minimum of $M 0$ , a maximum of $M 1.5$ , with 25 contours at	

intervals of  $M = 0.06$ . The data is taken from Case 1:  $\alpha = 15^\circ \pm 10^\circ \sin(\Omega t + \pi)$ ,  
 $k = 0.101$ ,  $M = 0.292$ ,  $Re = 3.76 \times 10^6$ .....120

Figure 4.6: Vector plot showing (a) velocity boundary conditions and (b) vorticity contours during reverse flow,  $232^\circ$  azimuth.....122

Figure 4.7: Time-history of aerodynamic loads, Case 2 variable freestream. Each cycle begins at  $169^\circ$  azimuth measured at the airfoil.....124

Figure 4.8: Comparison of (a) lift, (b) pitching moment and (c) drag coefficients from Cases 1 and 2 of this work. The flow conditions correspond to  $M = 0.292$ ,  $Re = 3.76 \times 10^6$ ,  $\alpha = 15 \pm 10$  degrees and  $k = 0.1$  for Case 1 (steady freestream);  $M = 0.48 \pm 0.3$ ,  $Re = 3.3 \times 10^6 \pm 2.1 \times 10^6$ ,  $\alpha = 15 \pm 10$  degrees and  $k = 0.018 - 0.078$  for Case 2 (variable freestream).....125

Figure 4.9: Positions of images in Figure 4.10 indicated on coefficient of (a) lift and (b) pitching moment CFD results for Case 2. The solid line indicates the upstroke and the dashed line indicates the downstroke. (c) Azimuthal positions of images of Figure 4.10. dashed line is speed, solid line is the angle of attack. ....129

Figure 4.10: Velocity vector plots and pressure contours (left column) and Mach contours and streamline plots (right column), corresponding to the positions of the points indicated in Figure 4.9, respectively. Pressure contours show a minimum of 12.5 kPa, a maximum of 250 kPa, with 76 contours at intervals of 3.125 kPa. Mach contours show a minimum of  $M = 0$ , a maximum of  $M = 1.75$ , with 25 contours at intervals of  $M = 0.07$ . The data is taken from Case

2:  $\alpha = 15^\circ \pm 10^\circ \sin(\Omega t + \pi)$ ,  $k_{avg} = 0.0293$ ,  $M = 0.48 \pm 0.3 \sin \Omega t$ ,  $Re_{avg} = 3.31 \times 10^6$ .....136

Figure 4.11: Positions of images in Figure 4.12 indicated on (a) coefficient of lift and (b) pitching moment CFD results for Case 1. The solid line indicates the upstroke and the dashed line indicates the downstroke.....137

Figure 4.12: Comparison of steady freestream (left column) and variable freestream (right column) pressure contours and velocity vector data, corresponding to the positions of the points indicated in Figure 4.11, respectively. The scales and units of the images in this figure are consistent with those presented in Figure 4.5 and Figure 4.10.....143

# Nomenclature

Symbol	Definition [units]
$a$	Speed of sound [m/s]
	Element of matrix $A$
$a_l$	Constant of SST turbulence model [-]
$A$	Wing area [m <sup>2</sup> ]
	Amplitude of oscillation [m]
	Area of integration [m <sup>2</sup> ]
	Coefficient matrix, definition of CFD problem
$A_s$	Coefficient for Sutherland's formula [kg / (m·s·K <sup>1/2</sup> )]
$b$	Source vector, CFD problems
	Element of matrix $B$
$c$	Chord length [m]

<b>Symbol</b>	<b>Definition [units]</b>
$c_t$	Constant of SST turbulence model [-]
$C_d$	Sectional coefficient of drag [-]
$C_f$	Coefficient of friction [-]
$C_l$	Section coefficient of lift [-]
$C_M$	Coefficient of pitching moment [-]
$C_p$	Constant pressure specific heat capacity [J/(g·K)] Coefficient of pressure [-]
$C_T$	Coefficient of thrust [-]
$C_v$	Constant volume specific heat capacity [J/(g·K)]
$C_w$	Coefficient of work [-]
$Co$	Courant number [-]
$C_\mu$	Constant of wall function [-]
$d$	Vector between cell of interest and neighbouring cell [m] Distance along airfoil surface upon which the force at a node acts [m]
$D$	Sectional drag force [N/m]
$e$	Specific internal energy [J/kg]
$E$	Turbulence model constant [-]
$f_x$	Ratio of distances between cell face and center to cell center and neighbouring cell center

<b>Symbol</b>	<b>Definition [units]</b>
$h_0$	Specific enthalpy [J/kg]
$H_f$	Specific heat of fusion [kJ/kg]
$I$	Turbulence intensity
$k$	Reduced frequency [-] Turbulent kinetic energy [J/kg]
$l$	Mesh edge length [m]
$L$	Sectional lift force [N/m]
$M$	Mach number [-] Sectional pitching moment [N·m/m]
$n$	Number of equations and unknowns Number of cells
$P$	Pressure [Pa]
$\hat{P}$	Direction of application of pressure force
$P_k$	Source term, turbulent energy dissipation [Pa/s]
$\widetilde{P}_k$	Source term, turbulent kinetic energy [Pa/s]
$Pr$	Prandtl number [-]
$Pr_t$	Turbulent Prandtl number [-]

<b>Symbol</b>	<b>Definition [units]</b>
$r$	Radial position along rotor blade span, measured from the hub [m]
	Ratio of upwind- to downwind-side gradient [-]
	Mesh expansion ratio [-]
$R$	Rotor blade span [m]
	Specific gas constant [J/(kg·K)]
	Ratio of first to last cell size along an edge of a mesh [-]
$Re$	Reynolds number [-]
$S$	Invariant measure of the strain rate [1/s]
	Surface of integration [m <sup>2</sup> ]
$S_e$	Source term, energy equation
$S_u$	Source term, $x$ -momentum equation
$S_v$	Source term, $y$ -momentum equation
$S_w$	Source term, $z$ -momentum equation
$S_E$	Source term considering potential energy effects
$S_M$	Source term, considering body forces and viscous stresses
$S_I$	Source term, continuity equation
$S_\phi$	Source of quantity $\phi$

<b>Symbol</b>	<b>Definition [units]</b>
$t$	Time [s]
	Airfoil chord thickness [m]
$T$	Force of thrust [N]
	Temperature [K]
$T_s$	Coefficient for Sutherland's formula [K]
$u_\tau$	Friction velocity [m/s]
$U$	Airflow speed [m/s]
$V$	Volume of integration [m <sup>3</sup> ]
$x$	Column vector of dependent variables for CFD problem
	Element of matrix $X$
$y$	Distance from a cell to the nearest wall [m]
$y_l$	Distance of cell center to wall [m]
$y^+$	Dimensionless wall distance [-]
$y^*$	Dimensionless wall distance [-]
$\alpha$	Angle of attack [degrees]
	Relaxation factor [-]
$\alpha_l$	Amplitude of angle of attack oscillation [degrees or radians]
$\beta_l$	Constant of wall function [-]

<b>Symbol</b>	<b>Definition [units]</b>
$\beta_k$	Constant of SST turbulence model [-]
$\beta_\omega$	Constant of SST turbulence model [-]
$\beta^*$	Constant of SST turbulence model [-]
$\gamma$	Isentropic expansion factor; the ratio of specific heats of a gas at a constant-pressure to that of the same gas at a constant-volume [-]
$\gamma_1$	Constant of SST turbulence model [-]
$\gamma_2$	Constant of SST turbulence model [-]
$\Gamma$	Coefficient of diffusion
$\delta t$	Timestep [s]
$\delta x$	Mesh node spacing [m]
$\varepsilon$	Energy dissipation [J/(kg·s)]
$\zeta$	Aerodynamic torsional damping factor [-], counterclockwise is positive
$\kappa$	Constant of SST turbulence model [-], von Kármán's constant
$\lambda$	Reduced Amplitude [-]
$\lambda_s$	Characteristic speed of a wave travelling in the direction of the airflow [m/s]
$\mu$	Dynamic viscosity [Pa·s]  Advance ratio [-]
$\mu_{eff}$	Effective viscosity

<b>Symbol</b>	<b>Definition [units]</b>
$\mu_t$	Eddy viscosity [Pa·s]
$\nu$	Kinematic viscosity [m <sup>2</sup> /s]
$\rho$	Air density [kg/m <sup>3</sup> ]
$\sigma_k$	Constant of SST turbulence model [-]
$\sigma_\omega$	Constant of SST turbulence model [-]
$\tau$	Shear Stress [Pa]
$\varphi$	Phase shift [degrees]
$\phi$	General variable representing a quantity transported by a transport equation
	Momentum flux [kg/(m <sup>2</sup> ·s <sup>2</sup> )]
$\Phi$	Dissipation function in the energy equation
$\psi$	Rotor blade azimuth angle [degrees]
$\omega$	Specific turbulent dissipation rate [1/s]
$\Omega$	Frequency of rotation of rotor blade [rad/s]

### **Subscripts**

<i>airfoil</i>	Associated with the airfoil boundary
<i>drag</i>	Vertical projection in airfoil coordinates
<i>e</i>	Face to the east of the cell center
<i>eff</i>	Airfoil surface along which a force acts

<b>Symbol</b>	<b>Definition [units]</b>
$E$	Cell to the east of the cell of interest
$f$	Values at a cell face
$fwd$	Forward speed of helicopter component of rotor blade relative airflow
$i$	Einstein (index) notation
	Indication of equation being solved in Gauss-Seidel point-iterative method
$inlet(t)$	Associated with the inlet boundary at time $t$
$j$	Einstein (index) notation
	Indication of equation being solved in Gauss-Seidel point-iterative method
$k$	Einstein (index) notation
$lag$	Associated with time lag
$lift$	Horizontal projection in airfoil coordinates
$max$	Maximum over a cycle of blade rotation
$N$	Neighbouring cell
$P$	Cell of interest
$rot$	Conditions of rotation
$ss$	Static stall
$TIP$	Conditions at the rotor blade tip

<b>Symbol</b>	<b>Definition [units]</b>
---------------	---------------------------

$w$	Data at wall
$x$	Drag component of coefficient of friction
$y$	Lift component of coefficient of friction
$\infty$	Freestream conditions
	Helicopter forward flight speed

### **Superscripts**

$k$	Iteration number
$n$	The timestep being solved
$o$	Data stored from the previous timestep
$oo$	Data stored from a timestep before the last time step
$'$	Turbulent (fluctuating) component of a quantity

### **Mathematical Descriptions**

$\bar{\phi}$	Quantity $\phi$ normalized by chord length
--------------	--

### **Abbreviations**

AOA	Angle of Attack [degrees]
BEMT	Blade Element Momentum Theory
BVI	Blade-Vortex Interaction

<b>Symbol</b>	<b>Definition [units]</b>
CAMRAD	Comprehensive Analytical Model of Rotorcraft Aerodynamics and Dynamics
CFD	Computational Fluid Dynamics
CV	Control Volume
DNS	Direct Numerical Simulation
EDLIN	Équations différentielles linéaires
LES	Large-Eddy Simulation
LEV	Leading-Edge Vortex (Dynamic Stall Vortex is used analogously in some references)
LLR	Local Linear Realizable
LODI	Locally One-Dimensional Inviscid
LSB	Laminar Separation Bubble
NACA	National Advisory Committee for Aeronautics
NSCBC	Navier-Stokes Characteristic Boundary Condition
OpenFOAM	Open Field Operation and Manipulation
OES	Organized Eddy Simulation
ONERA	Office national d'études et de recherches aérospatiales
SST	Shear Stress Transport
STOL	Short Takeoff and Landing

<b>Symbol</b>	<b>Definition [units]</b>
S-A	Spalart-Allmaras
TEV	Trailing-Edge Vortex
TVD	Total Variation Diminishing
URANS	Unsteady Reynolds-averaged Navier-Stokes
VTOL	Vertical Takeoff and Landing

# **Chapter 1**

## **Introduction**

Helicopters are widely used for civilian and military applications due to their unique ability to take-off and land vertically. They are complex machines which face many design challenges that are unique to this type of aircraft. This chapter describes the general operating conditions of helicopters, introduces the phenomenon of dynamic stall and defines the objectives of this thesis.

### **1.1 Rotorcraft Aerodynamics**

Flight vehicles, at the most general level, can be categorized as heavier-than-air or lighter-than-air vehicles. Within the heavier-than-air category are fixed-wing and rotary-wing vehicles. Rotary-wing vehicles are well known for their vertical takeoff and landing (VTOL) or very-short takeoff and landing (STOL) capabilities and hence offer unique capabilities for certain missions. Depending on the power delivered to the rotary wings,

we can distinguish between autogiros and helicopters. On autogiros, the main rotor is unpowered or freely rotating due to its unique design and setup relative to the freestream (i.e. it works just like a windmill). This provides lift while the propulsive force is generated by a powered propeller. Helicopters – on the other hand – generate both lift and propulsive force from the powered main rotor. Thus, on a helicopter a single rotor fulfils both functions at the same time. Although there are several configurations of helicopters, notably different in their means of counteracting the torque generated by the rotation of the main rotor and controlling yaw, the description of their aerodynamics presented here will consider the most common configuration: that of the single main rotor and single tail rotor design.

### 1.1.1 Helicopters in Hovering Flight

As shown in Figure 1.1*a*, in hovering flight, the rotor blades have a constant angle of attack with the relative airflow throughout the azimuth,  $\psi$ , with  $180^\circ$  defined as the forward direction of the helicopter. The speed of the relative airflow of a blade section due to rotor blade rotation,  $U_{rot}$ , given by

$$U_{rot} = r \Omega \quad (1.1)$$

is a function of rotational speed of the rotor blade,  $\Omega$ , and radial distance from the hub of the blade section,  $r$ , which varies in value from zero to  $R$ , the rotor blade length.

The rotation of the rotor blades subject them to a number of forces which affects their behaviour. The lift force generated by the rotor will tend to draw the blade upward, at a

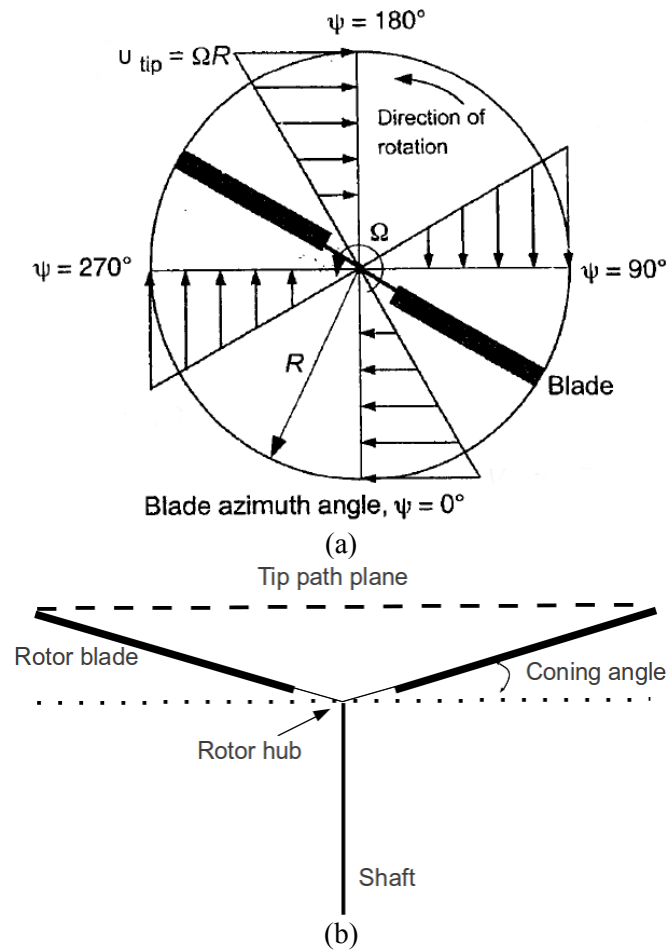


**Figure 1.1:** (a) Top-view of rotor blades showing the distribution of incident velocity as a function of azimuth in hovering flight, adapted from Leishman (2006). (b) Side view of rotor shaft and blades showing coning angle and tip path plane.

coning angle, which places the tip path plane above the rotor hub as shown in Figure 1.1*b*. The drag force on the blades causes the tip of the blade to lag slightly behind the root of the blade in azimuth angle. The centrifugal force or inertia of the rotating blades will tend to counteract the coning and lag forces. Note that helicopter rotors feature a “rotor hub” to allow for these type of motion via hinges or flexures, explained in greater detail later.

### 1.1.2 Helicopters in Forward Flight

Forward flight at a speed of  $U_\infty$  adds a component of velocity that varies as a function of azimuth in the reference frame of the rotating blade element, as shown in Figure 1.2, given by

$$U_{fwd} = U_\infty \sin \psi = U_\infty \sin \Omega t \quad (1.2)$$

where the azimuth of rotation is given by the product of the rotor blade rotational speed and time,  $t$ .

The sum of both the rotational and forward speed components give the resultant relative airflow, which in the reference frame of the rotor blade is given by

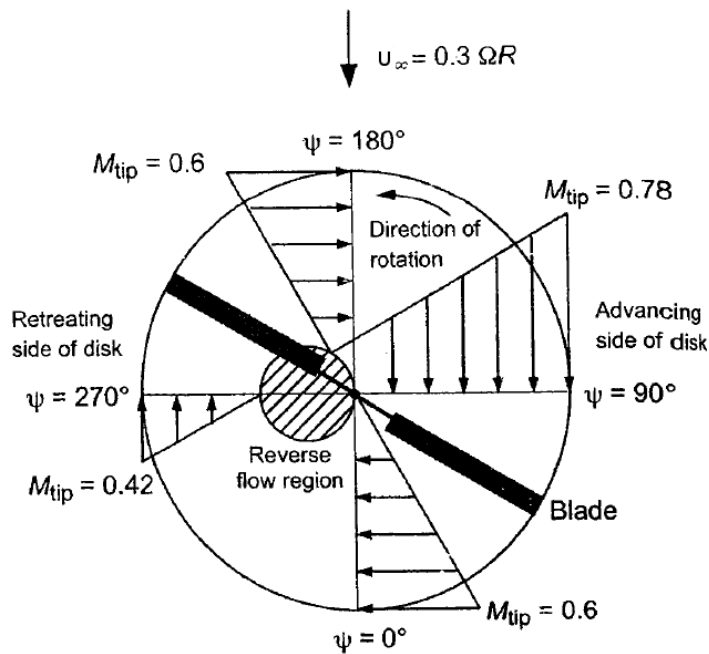


**Figure 1.2:** Top-view of rotor blades showing the distribution of incident velocity as a function of azimuth in forward flight, with notional values for the tip and forward speeds. Adapted from Leishman (2006).

$$U = U_{fwd} + U_{rot} \quad (1.3)$$

by substituting Equations (1.1) and (1.2) into (1.3), we obtain

$$U = U_{\infty} \sin \psi + \Omega r \quad (1.4)$$

The forward flight speed of a helicopter is most often expressed by the non-dimensional term “advance ratio”, which is the ratio of the aircraft's forward flight speed to the blade tip speed,  $U_{TIP}$ , i.e.

$$\mu = \frac{U_{\infty}}{U_{TIP}} = \frac{U_{\infty}}{R \Omega} \quad (1.5)$$

Advance ratio is a very revelatory parameter for helicopters, since it also describes the size of the reversed flow region on helicopter blades in forward flight. Note from Figure 1.2 that the reverse flow region is a perfect circle. Interestingly enough, the diameter of this circle is exactly equal to the product  $\mu R$ . Typical advance ratios for helicopters range between 0.2-0.4 in cruise, which means that 20-40% of the blade does not generate lift at at  $\psi = 270^\circ$ , since it experiences reversed flow (i.e. the resultant airstream “blows” from the trailing edge and not from the leading edge). One of the main findings of this thesis is – as the reader will see later – that reversed flow can occur outside of this region too.

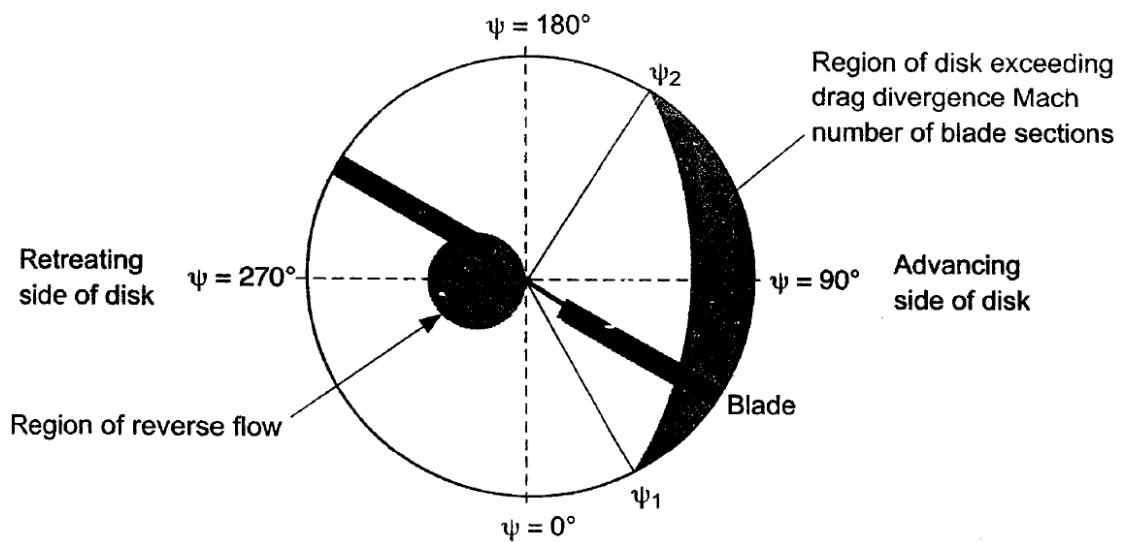
As the advance ratio increases, complex flow phenomena begin to appear on both the advancing and retreating sides of the rotor disc. The advancing blades, which see the fastest relative airflow, may experience transonic effects including shock waves. The retreating blades, as explained earlier, will see reversed flow, as shown in Figure 1.2 and

Figure 1.3.

### 1.1.3 Rotor Control

The magnitude of the aerodynamic force generated by the main rotor is controlled by changing the angle of attack on all rotors collectively by actuating the pitch links in unison. Changing the collective is the only input used in hover. In horizontal flight, however, the angle of the aerodynamic force generated by the rotor must be tilted to create a horizontal component of thrust, called the propulsive force. The direction of the aerodynamic force is controlled by applying a sinusoidal (or “cyclic”) distribution to the angle of attack of the rotor blades as they travel the azimuth of rotation.

Varying the angle of attack during the rotor blade revolution is especially important in forward flight, to address the problem of dissymmetry of lift caused by the difference in airspeed seen by the advancing side of the rotor disk compared to the retreating side. The



**Figure 1.3:** Regions of reverse flow and compressibility effects. Reproduced from Leishman (2006).

higher airspeed creates greater lift on the advancing side, generating a rolling moment on the aircraft that is compensated by varying the resultant angle of attack (AOA) along the azimuth, i.e. increasing AOA when the resultant freestream is low and decreasing AOA when the resultant freestream is high. This can be achieved in two ways: either by allowing the blades to flap vertically due to the varying lift load - “plunging (or flapping) motion” - or by introducing a periodic change of the AOA throughout the azimuth - “pitching motion”. The result of either motion is that the AOA varies in the opposite sense as the resultant freestream. In reality, a combination of “plunging” and “pitching” occurs, although this does not change the fundamental principle: that the AOA is changing periodically within each revolution.

**Plunging motion** can be enabled by allowing the blades to flap up and down freely. This can be achieved by introducing a “flapping hinge” or flexure at the blade root, allowing out-of-plane bending (or flapping) of the blades. Another option is to increase the flexibility of the blades, though this might raise strength issues.

**Pitching motion**, on the other hand, is enabled via the cyclic variation of the blade pitch angle within one revolution. Such motion requires freedom of rotation of the blades to be enabled along their quarter-chord line, which can be achieved by introducing a “feathering hinge” at the blade root.

In addition to the flapping and feathering hinges, a “lead-lag” hinge must also be introduced, to relieve the in-plane bending moments generated by the Coriolis forces caused by the flapping motion. These motions with respect to the blade rotor are shown

in Figure 1.4.

A rotor hub featuring all three of these hinges, “flapping”, “lead-lag” and “feathering”, is termed a “fully articulated hub”. When the role of the hinges is performed by blade flexures, then we talk about a “hingeless” or “bearingless” rotor hub. In both cases, the blades are allowed three degrees of freedom motion at the blade root, of which only one is controlled by the pilot: the pitching motion. An example of an articulated hub is shown in Figure 1.5.

The frequency at which the above change in the resultant AOA occurs corresponds to the rotational frequency of the rotor, i.e. once per revolution. The rotational frequency of helicopter rotors is typically in the 3-5 Hz range (note that rotor frequency is constant for helicopters, and dictated by maintaining a blade tip speed around Mach 0.6), which is going to be the frequency of the resultant blade section angle of attack change, i.e. that of the so-called “dynamic stall” phenomenon too. Dynamic stall is a phenomenon where the airflow over the blade upper surface remains attached beyond the static stall angle, leading to a temporary increase in both lift and pitching moment until they both stall in a

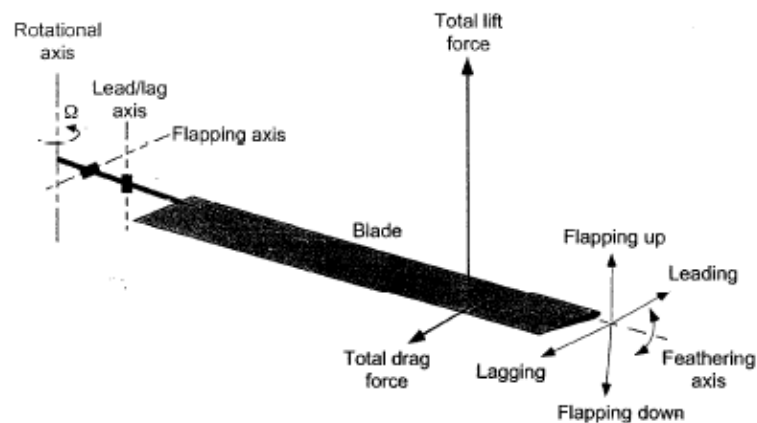


**Figure 1.4:** Diagram of flapping, feathering and lead-lag motions on a rotor blade. Reproduced from Leishman (2006).

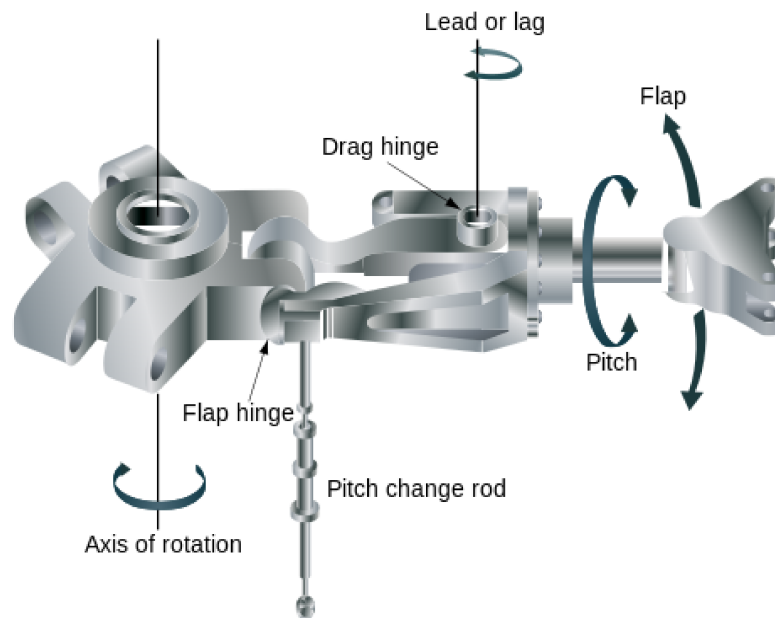


**Figure 1.5:** Diagram of an articulated hub, reproduced from FAA (2008).

rather dramatic fashion at the point of dynamic stall. It is caused by the cyclic change in AOA which can be achieved by pure flapping (plunging motion), pure pitching (cyclic control), or a combination of both. The result is that the AOA becomes very large at a point where the relative airflow seen by the rotor section is very slow. Dynamic stall is common toward the outboard section of the rotor blade with the notable exception of the tip region, and is most pronounced typically between  $r = 0.77R$  to  $0.92R$  (Leishman, 2006), and discussed in further detail below.

## 1.2 Static and Dynamic Stall

The high-lift, high-forward speed portion of the flight envelope of a helicopter is limited by two phenomena: drag due to compressibility effects on the advancing rotor



airfoil causes flow separation at low angles of attack. The boundary layer may reattach, in a turbulent state, forming a laminar separation bubble (LSB) of short-bubble type. Transition takes place at the maximum height of the bubble as shown in Figure 1.7; reattachment is made possible by the entrainment of the turbulent flow (Ward, 1963). As the angle of attack increases, this bubble moves forward toward the leading edge until reattachment of the boundary layer is no longer possible and stall takes place abruptly as the majority of the boundary layer separates at once. The third and final mechanism of static stall is the thin-airfoil stall, whereby a laminar separation bubble of long-bubble type is formed and the reattachment point moves aft with increasing angle of attack until reattachment fails to take place, known as “bursting” of the LSB (Ward, 1963), and stall occurs. All three of the static stall processes are quite different when the rate of change of angle of attack is no longer quasi-steady, and dynamic stall takes place.

## 1.2.2 Dynamic Stall

The nature of dynamic stall is quite different from that of static stall as a result of the rapid pitching motion and the increase of the peak angle of attack beyond the static stall

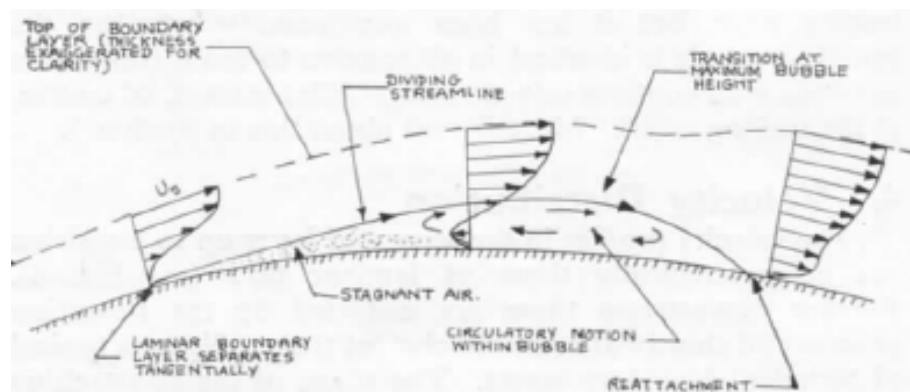


**Figure 1.7:** Airflow in the vicinity of a laminar separation bubble, reproduced from Ward (1963).

angle. This peak angle defines the “depth” of dynamic stall; as the depth increases, the flow characteristics differ to a greater extent from those of static stall.

Dynamic stall occurs when helicopter rotor blades are at a high advance ratio and a high thrust coefficient as defined below, where the angle of attack is high and the speed seen by the retreating rotor blades is low. These conditions are found on the rotor disk during high speed forward flight or during manoeuvres where high blade loading is required such as a symmetric pull-up or a high-speed diving turn, maneuvers which represent design conditions for helicopters such as the UH-60 (Bousman, 1998). Bousman observed, on flight tests of the UH-60 helicopter in various maneuvers, that multiple dynamic stall cycles were observed on the rotor disk as indicated on the rotor azimuth in Figure 1.8.

The effect of high advance ratios was described above, their effect on the retreating side of the blade azimuth being relevant for dynamic stall. The coefficient of thrust, adapted from Leishman (2006) is given by

$$C_T = \frac{T}{\rho A (\Omega R)^2} \quad (1.6)$$

where  $\rho$  is air density,  $T$  is the force of thrust and  $A$  is the blade area. A high  $C_T$  is indicative of a high angle of attack since the thrust is dependent on the collective and greater thrust requires a higher angle of attack. The effects of dynamic stall are more pronounced at higher angles of attack where the blade angle exceeds the static stall angle.

Compared to a static stalling airfoil, Gerontakos (2008) observed that boundary layer

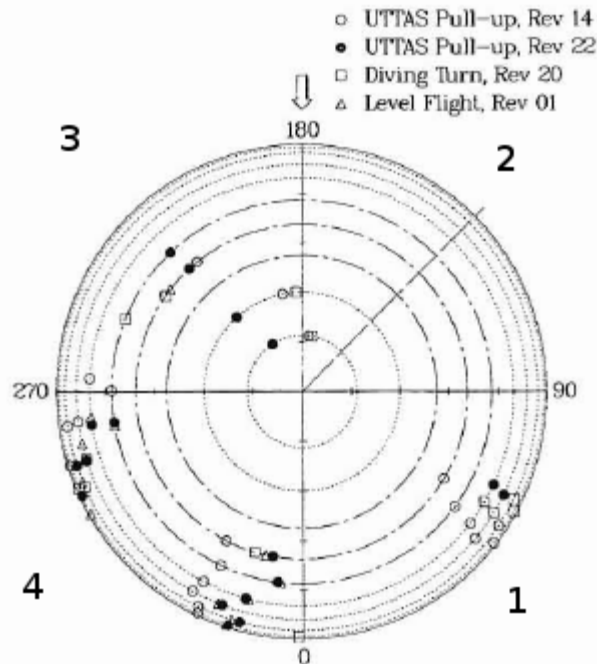


**Figure 1.8:** UH-60 dynamic stall rotor map. Points on map indicate convection of LEV past the rotor blade mid-chord. Quadrants are numbered 1-4 counter-clockwise from the 0-90° azimuth range which is quadrant 1. Adapted from Bousman (1998).

transition was delayed and progressed upstream more slowly on a dynamically stalling airfoil. The presence of the LSB was observed, consistent with static stall behaviour. It was also observed that the boundary layer was thinner, and flow reversal was delayed to larger angles of attack; observations attributed to the dynamic motion. Different regimes of flow exist depending on the maximum angle of attack,  $\alpha$ , attained.

### 1.2.2.1 Attached Flow: $\alpha_{max} \leq \alpha_{ss}$

When the maximum angle of attack,  $\alpha_{max}$ , is below the static stall angle,  $\alpha_{ss}$ , flow remains attached throughout the motion, and hysteresis and aerodynamic loads do not differ significantly from static values.

### 1.2.2.2 Light Stall: $\alpha_{\max} > \alpha_{ss}$ , LEV Shedding at $\alpha_{\max}$

Light dynamic stall takes place when the maximum airfoil angle of attack exceeds the static stall angle, the angle of attack reaches its maximum before the onset of stall, and the change in pitch direction causes the shedding of the leading edge vortex (LEV) (Mulleners and Raffel, 2012). A thin layer of reversed flow may be present over the airfoil, lifting the boundary layer from the surface – however the boundary layer continues to follow the airfoil curvature therefore the flow is not considered to be separated. As a result, the presence of reverse flow is not always indicative of flow separation, unlike with static stall where they always coincide, as shown in Figure 1.9 (Carr *et al.*, 1977). The pre-stall layer of flow reversal can exist with little impact to the boundary layer thickness and little distortion to the freestream. At the top of the upstroke,

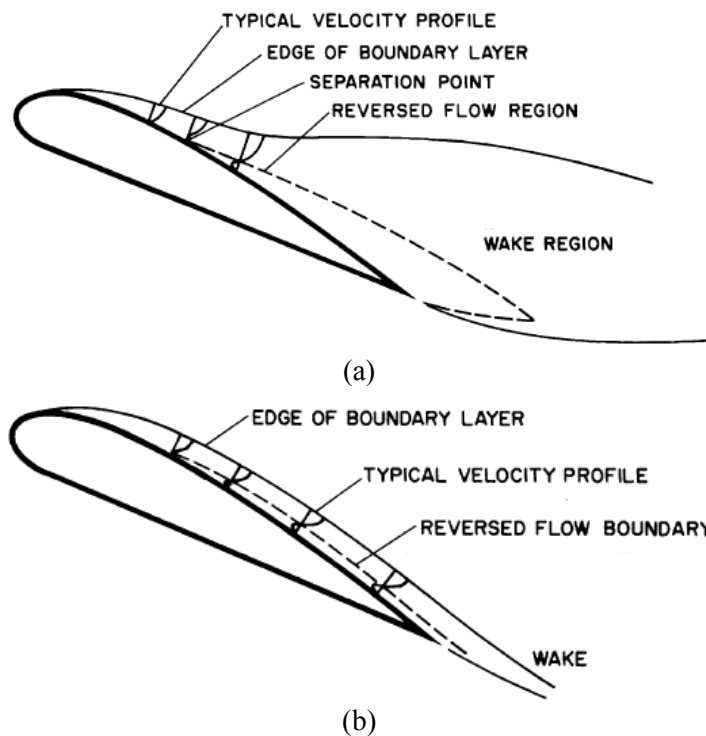


**Figure 1.9:** Comparison of reverse flow conditions on (a) static and (b) unsteady airfoils. Reproduced from Carr *et al.* (1977).

deceleration of the airfoil causes a LEV, also referred to as the dynamic stall vortex in other sources, to be formed – the defining feature of dynamic stall, and a key difference between dynamic and static stall. The downstroke motion causes a smaller separation region and weaker LEV than in the deep stall case, as discussed below. McCroskey *et al.* (1976) determined that the mechanism of dynamic stall, and LEV generation, was rapid turbulent boundary layer separation and not bursting of the LSB. This is an important point since it differentiates the mechanisms of static and dynamic stall, and also explains how dynamic stall occurs when a LSB is not formed. The LEV grows and is convected aft over the airfoil chord, leading to hysteresis and increases in the aerodynamic loads, a nose-down pitching moment, and a negative work coefficient (negative aerodynamic damping). The net effect of these is to create a favourable increase in lift generated and attached flow maximum angle of attack, and several unfavourable effects including high torsional blade loading, blade vibration, and large pitch link loads. High loads can exceed fatigue or endurance limits of components, making dynamic stall a design condition which, along with compressibility effects on the advancing side of the rotor disc, effectively limit helicopter forward speed, as shown in Figure 1.10. Westland Helicopters considers the influence of retreating blade dynamic stall in sizing the main rotor blade area (Isaacs and Harrison, 1989), and helicopter model wind tunnel tests (McHugh, 1978) found that the maximum lift limit of a helicopter is defined by dynamic stall. Perry (1987) wrote that dynamic stall is acceptable for transient maneuvers but not for steady-state flight conditions such as cruise.

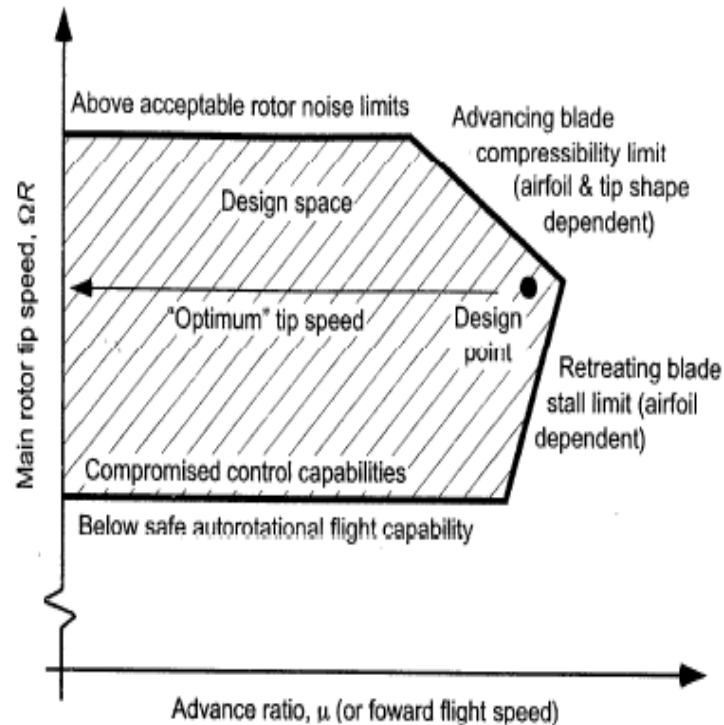


**Figure 1.10:** Helicopter design constraints on forward speed and main rotor tip speed. Adapted from Leishman (2006).

### 1.2.2.3 Deep Stall: $\alpha_{\max} \gg \alpha_{ss}$ , LEV Shedding During Upstroke

When the maximum airfoil pitch angle exceeds the static stall angle by a greater margin than light stall, the onset of stall typically occurs prior to reaching the maximum angle of attack, and deep dynamic stall is said to take place (Mulleners and Raffel, 2012). With increasing angle of attack, a stronger LEV is formed than in the light stall case, exacerbating the effects of light stall: increasing the aerodynamic load peaks, delaying stall to a higher angle of attack, and increased loads loop hysteresis.

Thus, dynamic stall is a complex phenomenon whose behaviour is influenced by the Mach and Reynolds number, frequency and magnitude of airfoil pitch oscillation, three-dimensional effects and the variable freestream conditions in which dynamic stall is

native. Due to the complexities of modelling all of these effects, either experimentally or numerically, modelling and simulation of this phenomenon have so far been confined to less than representative conditions.

### 1.2.3 Dynamic Stall: the State of the Art

Despite the importance of dynamic stall as a major design constraint for helicopters, and the significant amount of research conducted on dynamic stall in general, there has been surprisingly little research carried out at conditions representative of helicopter flight. Dynamic stall is a complex phenomenon which involves not only the rapid variation of AOA, but necessarily also with a rapid variation of the Mach number of the rotor blade. However, as will be discussed further in Chapter 2, it is difficult to model both of these conditions simultaneously either experimentally or numerically.

Although some 2D experimental studies have been completed, so far none have been able to reproduce the time-variation of the freestream in the range that is typical for helicopters (Favier *et al.*, 1992, Gompertz *et al.*, 2012). There have been some recent CFD studies that have combined the two motions (Martinat *et al.*, 2009, Gharali and Johnson, 2013), though only one has studies realistically high AOA and freestream variation simultaneously, and this study was carried out on an uncommon airfoil (Kerho, 2007). These references will be explained in detail in Chapter 2.

For this reason, the aim of this thesis is to examine the effect of variable freestream on 2D dynamic stall – with realistic AOA and Mach number ranges – and to determine whether using constant freestream results is acceptable for aeromechanic codes. The

---

literature review in the next chapter will provide more details and clear pointers to the reader into why studying this phenomenon is timely and appropriate.

### **1.3 Thesis Objectives**

This thesis aims to demonstrate, through the use of Computational Fluid Dynamics (CFD), the effects of a time-varying freestream on dynamic stall at flight conditions that are representative of those in which dynamic stall would occur on a helicopter in flight. Leishman (2006) stated in his book “Principles of Helicopter Aerodynamics” that “The issue of time-varying incident flow velocity, unfortunately, has not yet been studied in detail using the various mathematical models of dynamic stall, and it would seem to be an ideal problem whose investigation is overdue.” The main purpose of this thesis is to address this overdue problem, specifically to determine whether the mechanism of dynamic stall changes in the presence of a time-varying freestream velocity magnitude, and therefore whether models that do not consider a time-varying freestream are valid for dynamic stall modelling.

CFD as a modelling tool is suitable for predicting the flow field of this problem, due to its flexibility in assigning boundary conditions that are not necessarily easily reproduced experimentally. However, the previous statement must be qualified by the fact that flow separation remains an area that requires improvement in CFD. This thesis will generate results under flow conditions for which no experimental results exist, and validation will be carried out for conditions resembling those of interest as closely as

possible. The assumption will be made that the model will remain valid for the difference between the two sets of conditions.

## **Chapter 2**

# **Background and Literature Review**

Dynamic stall behaviour is far more complex than the stall behaviour of a static airfoil. A great deal of analytical, experimental, and numerical studies have been conducted to study its effects, a body of work whose size alone is an indication of the complexity and importance of the issue. This literature review is organized into five sections. The first section describes the mechanism of dynamic stall. This is followed by a section that describes the nature and impact of stall flutter. The third section identifies the parameters which affect dynamic stall and their impact on its mechanism. The fourth section is a description of the numerical modelling completed by other researchers. The fifth and final section summarizes the key points of the other sections and demonstrates how it supports the motivation for the research.

## 2.1 Mechanisms of Formation of Dynamic Stall

Leishman (2006) describes the dynamic stall process as having five stages which regroup the qualitative events defining the phenomenon, as illustrated in Figure 2.1. In the section that follows, the letters in brackets refer to the events as shown in that figure. More thorough descriptions of dynamic stall are discussed by McCroskey (1973, 1982), McCroskey *et al.* (1976), Carta (1971), Carr *et al.* (1977) and McAlister *et al.* (1978).

In stage one, dynamic stall begins as the angle of attack exceeds the static stall angle of the airfoil (a). Rapid pitch-up motion of the airfoil delays the onset of boundary layer separation to higher angles of attack, including angles beyond  $\alpha_{ss}$  under certain conditions. The delay in the onset of boundary layer separation is caused by three

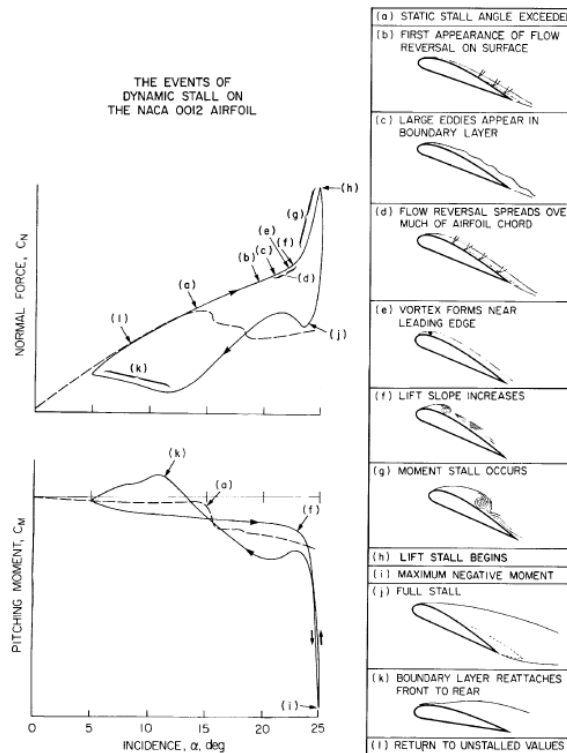


**Figure 2.1:** Dynamic Stall Events on the NACA 0012 Airfoil. Reproduced from Carr *et al.* (1977).

unsteady effects. First, there is a reduction in the adverse pressure gradient on the suction surface compared to a static airfoil at the same angle of attack. This reduction is caused by the kinematics of the positive pitch rate, known as induced camber and is illustrated in Figure 2.2. Second, the time-varying angle of attack sheds circulation from the trailing edge of the airfoil, decreasing the adverse pressure gradient on the suction surface of the airfoil and as a result, the lift generated by the airfoil. Third, external pressure gradients cause unsteady effects in the boundary layer including reverse flow prior to flow separation, which delays the onset of stall (Leishman, 2006, and Davis, 2006). This delay in flow separation causes a desirable increase in lift, however this comes at a cost of less desirable effects in the latter stages of dynamic stall.

Unlike static stall, where the lift and moment stalls occur simultaneously, in dynamic stall the pitching moment stall occurs first and is followed by the lift stall at higher angle of attack. The second stage begins as a shear layer forms downstream of the leading edge where high adverse pressure gradients cause flow separation to take place (b-d). The shear layer then forms a vortex that is shed from the leading edge region of the airfoil (e), known as the Leading Edge Vortex (LEV) – a defining feature of dynamic stall. The LEV

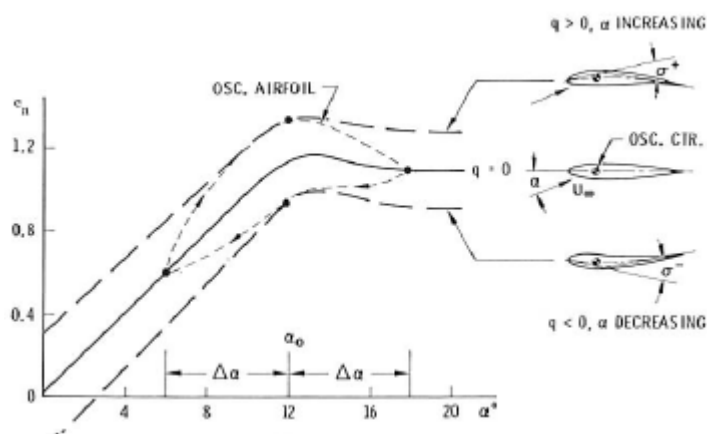


**Figure 2.2:** Frequency induced camber, reproduced from Ericsson and Reding (1972).

reduces the pressure on the upper surface of the airfoil and the leading-edge pressure gradients, increasing lift beyond that which could be created by a quasi-static airfoil at the same angles of attack and delaying separation to higher angles of attack. Carr (1977) has observed an increase in the lift-curve slope (f) following formation of the LEV. This increase in lift is accompanied by a significant increase in nose-down pitching moment, the moment stall (g), resulting from the center of pressure moving aft as the LEV is convected downstream. The effect of the nose-down pitching moment is manifested on a helicopter as high torsional air loads on the blades, which may also introduce aeroelastic problems including stall flutter, as discussed below. The LEV grows as it convects aft over the airfoil at a speed less than that of the freestream, quantified differently in various references (Gerontakos, 2008, and Maresca, 1981) but generally within the range of  $0.25-0.55 U_\infty$ .

The third stage is the period in which the LEV is convected over the airfoil and into its wake, culminating in the peak lift value (h) followed by the sudden loss of lift and peak values of pitching moment and drag associated with lift stall (i). There is also a loss of dynamic lift on the helicopter associated with dynamic stall, though this effect is not as significant as that of the pitching moment, since the majority of a helicopter's lift is generated between 65% and 85% of the rotor span at the fore and aft arcs of the rotor disc (Feszty, 2004), away from the area where dynamic stall and the loss of lift take place. Feszty (2004) and Panda (1994) observed that, as the clockwise rotating LEV is shed from the leading edge in left-to-right flow, an anti-clockwise rotating trailing-edge vortex (TEV) is generated as a result of the low pressure of the LEV. As the LEV convects

downstream, the TEV becomes stronger and grows in size causing a second suction peak over the trailing edge of the airfoil that contributes significantly to the negative pitching moment. The LEV convects away from the surface of the airfoil and over the TEV as it moves beyond the trailing edge of the airfoil (Feszty, 2004). A third vortex has been observed by Visbal (1989) to form in low-Reynolds number flow near the mid-chord, though this does not occur at flight Reynolds numbers.

In stage four, the LEV has become entrained in the turbulent wake downstream of the airfoil, and the flow on the upper surface of the airfoil progresses to a state of full separation (j). Galbraith (1986) suggested that when an airfoil is fully stalled, it behaves as a bluff body and the flow loses its dependency on the airfoil in favour of the freestream, and that the model motion also loses influence. It was observed that there are constant dimensionless time delays between stall initiation and completion that are independent of pitch rate.

In stage five, the flow reattaches at low angles of attack, typically well below the normal static stall angle. Green (1995) studied the recovery of the airflow on the downstroke following dynamic stall. It was observed that reattachment followed a high rate of decrease in suction, and that the area of this high rate of decrease of suction travels downstream over the chord and is known as a “ramp-down wave”, which travels downstream at a rate of half of the freestream speed. Leishman (2006) explained that the lag in reattachment is caused by an induced camber effect on the leading edge pressure gradient, a result of the nose-down pitch rate as described above. The lag generates hysteresis loops in the pitch, drag and lift; these loops are the source of reduced

aerodynamic damping, which can lead to aeroelastic problems on the rotor such as stall flutter (Leishman, 2006). Aerodynamic damping and its effects are discussed in additional detail below.

## 2.2 Stall Flutter

Flutter is a dynamic aeroelastic effect, whereby divergent oscillations are caused by positive feedback between aerodynamic loads and the motion of an elastic structure, such as a helicopter rotor blade. When flutter occurs on an aircraft, the loads can quickly increase to the point of being catastrophic to the air vehicle in the absence of a rapid exit from the flight condition which excites the structure. In a helicopter, it is the pitch links that control angle of attack of the rotor blades and are exposed to failure under conditions of stall flutter. The avoidance of conditions that can generate stall flutter are a design condition for the flight envelope of the helicopter (Feszty, 2004). If the oscillations are caused by flow separation, the phenomenon is called stall flutter. Stall flutter is distinguished from dynamic stall by a smaller amplitude of oscillation, and the cause of the motion induced by the airflow rather than forced motion as with dynamic stall (McCroskey *et al.*, 1982).

The highly nonlinear air loads and negative aerodynamic torsional damping generated by a rotor blade section undergoing dynamic stall can introduce aeroelastic stability problems onto an otherwise stable rotor blade vibration mode such as high amplitude limit cycle oscillation or stall flutter. The aerodynamic torsional damping factor provides

an indication of the vibration-damping ability of the blade due to aerodynamic loads on the blade (McCroskey *et al.*, 1982), and is defined as a function of the work done by the pitching moment during one cycle of oscillation, given by Carta (1967):

$$\zeta = \frac{-C_W}{\pi \alpha_1^2} = \frac{-\oint C_M(\alpha) d\alpha}{\pi \alpha_1^2} \quad (2.1)$$

where  $C_W$  is the coefficient of work,  $C_M$  is the pitching moment coefficient,  $\alpha_1$  is the oscillatory amplitude.  $\zeta$  is positive for a counterclockwise loop in the pitching moment graph, which attenuates any vibration. Negative  $\zeta$  indicates that the airfoil extracts energy from the airflow, and the magnitude of any oscillations will increase (McCroskey *et al.*, 1982). The loops in the  $C_M$ - $\alpha$  curve are indications of the presence of hysteresis in the pitching moment, for both boundary layer separation and reattachment and, to a lesser extent, to boundary layer transition and relaminarization (McCroskey and Philippe, 1975). As discussed above, time lag and improvement to the boundary layer during the upstroke delay both separation and transition to higher angles of attack than the quasi-steady case. The down stroke also delays reattachment and relaminarization to lower angles of attack for reasons discussed above, the combination of the delays in separation on both the up- and down-strokes being to create hysteresis and the loops in the  $C_M$ - $\alpha$  curve.

Figure 2.3 illustrates the hysteresis loops as a function of the depth of dynamic stall. In attached flow,  $\alpha_{max} < \alpha_{ss}$ , damping is positive and the counter-clockwise loop increases in size as  $\alpha_{avg}$  increases toward  $\alpha_{ss}$ . Carr *et al.* (1977) observed hysteresis was only present when the airfoil oscillations extended above and below  $\alpha_{ss}$ , however Gerontakos (2008)

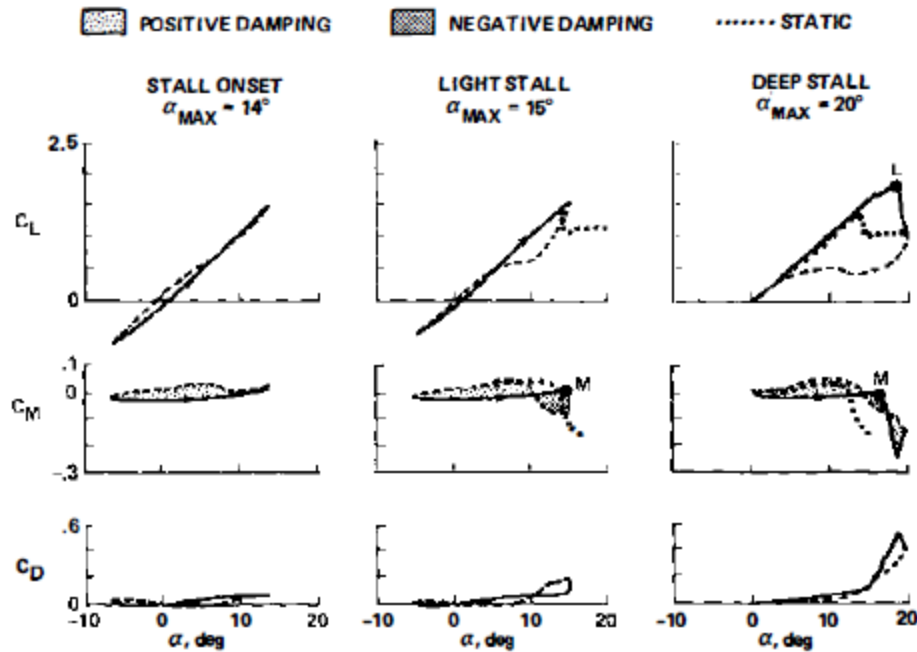


**Figure 2.3:** Unsteady airloads at various depths of dynamic stall,  $M = 0.3$ ,  $\alpha = \alpha_0 + 10^\circ \cos \Omega t$ ,  $k = 0.1$ .  $\alpha_0 = 4^\circ$ ,  $5^\circ$  and  $10^\circ$  for the stall onset, light stall and deep stall plots, respectively. Reproduced from McCroskey (1982). The solid line indicates the upstroke, the dashed line indicates the downstroke, and the dotted line is static airfoil data.

and McAlister *et al.* (1982) observed hysteresis under attached flow conditions as well. As  $\alpha_{max}$  begins to exceed  $\alpha_{ss}$  indicating the onset of light stall, a second loop forms in the  $C_M$ - $\alpha$  curve, this one clockwise making the curve resemble a figure-eight. Overall damping is reduced as this negative damping second loop grows in size with increasing depth of light stall, when damping can become negative (Leishman, 2006). As  $\alpha_{max}$  continues to increase into the deep stall regime, the peak moment occurs prior to the maximum angle of attack causing a third loop to appear in the  $C_M$ - $\alpha$  curve, this one counterclockwise, increasing the damping as the depth of stall increases further. The amount of aerodynamic damping can be influenced by manipulating the average angle of attack, the reduced frequency and the type of motion, as discussed in the next section.

## 2.3 Factors Influencing Dynamic Stall

With any simulation or experiment, similitude between the model and the flow being modelled can be obtained by matching the geometry, dynamics and kinematics of the flow, as well as the fluidelastic response of the rotor blade to the flow. The parameters in these categories affect the onset of flow separation, as well as the depth of stall, air load peak magnitudes and hysteresis. The effects of these parameters on dynamic stall are described in further detail in the subsections that follow, a summary of which is presented in Table 2.1. It is important to note that these parameters do not have an effect on the sequence of events in the stages of dynamic stall described above, but may affect the aerodynamic loading and the angle at which the events occur – a quantitative but not qualitative influence (Gerontakos, 2008).

### 2.3.1 Geometric Similitude

The shape of an airfoil has important effects on static stall characteristics; it also has an effect on dynamic stall characteristics. Since an airfoil section is but a two-dimensional cross-section of the true three-dimensional rotor blade, the assumptions present in two-dimensional modelling must be considered.

#### 2.3.1.1 Effect of Airfoil Shape

Experiments by McCroskey and Pucci (1982), Carr *et al.* (1977), and McCroskey *et al.* (1976) have shown that differences in airfoil shapes can significantly change the loads but have little influence over the mechanism of dynamic stall. Essentially, a change in

**Table 2.1:** Relative importance of parameters affecting dynamic stall, adapted from McCroskey *et al.* (1976).

	<b>Parameter</b>	<b>Effect</b>
Geometric	Airfoil Shape	May influence the type of stall
	3D Effects	Reduce LEV convection speed
	Pitch Axis Location	Affects pressure distribution on airfoil and aerodynamic damping
Dynamic	Reynolds Number	Minimal effect
	Compressibility	Small below Mach 0.2/0.3; above this separation is promoted
Kinematic	Reduced Frequency	Contributes to depth of stall
	Mean Angle, Amplitude	Contributes to depth of stall.
	Type of Motion	Plunging does not model all features of dynamic stall and underpredicts negative aerodynamic damping
	Time-Varying Speed	Further increase to $C_{max}$ , possible shock wave – boundary layer interaction effects can promote flow separation at low AOA
	Fluidelastic	Incidence of dynamic stall at additional locations of rotor disk

airfoil shape can influence the type of stall encountered (trailing-edge, leading-edge, thin-airfoil), as can changes in other parameters.

Airfoils with high static lift will generally enter dynamic stall at higher angles of attack than airfoils with low static lift, and better behaviour during static stall is an indication that better behaviour is likely to occur as well during dynamic stall (Gerontakos, 2008). However, airfoils designed for low static pitching moments will not necessarily exhibit low dynamic pitching moments. Leishman (2006) illustrated further that the effect of airfoil shape influences the timing of the moment stall and the depth of the moment break at moment stall. The NACA 0012 airfoil will be used in this research

because of the widely available results in literature for that airfoil, and its relevance to helicopter rotor blade applications due to its good compromise between high  $C_{lmax}$ , low pitching moment, and high drag divergence Mach number (Leishman, 2006). The high drag divergence Mach number is necessary to ensure that the airflow over the advancing blade does not limit the helicopter's performance more than the dynamic stall on the retreating blade. Despite the good performance of the NACA 0012 airfoil, other airfoils tested by McCroskey and Pucci (1982) showed significant advantages compared to it. Changes to the airfoil shape by means of flow control devices such as flaps or slats have been shown to be effective in mitigating the negative effects of dynamic stall, and are discussed below.

### **2.3.1.2 Three-Dimensional Effects**

Dynamic stall is a 3D phenomenon which occurs over different parts of the blade at different azimuth angles as shown in Figure 1.8, making the resulting flow very complicated, with more complex flow structures than 2D flow can model (Gardner, 2012). Three-dimensional effects include rotor blade sweep effects, the blade tip vortex, blade-vortex interaction and interference of the helicopter non-rotor blade wake. Leishman (2006) explains that apart from swept flow, 3D effects are still poorly understood. The research in this thesis does not consider 3D effects, since the experimental data available for comparison does not consider this effect and due to the computational expense and complication of modelling the complete rotor blade system.

A sweep angle is imparted on the flow by centrifugal effects caused by blade rotation, the Mach number gradient across the rotor blade span, flapping motion caused by the

Coriolis force (conservation of angular momentum) on the rotating blades in forward flight, and the component of the forward airspeed parallel to the rotor blade which is especially strong in high-speed forward flight at the forward and aft positions in the azimuth where the rotor blade approaches parallel with the freestream. These combined effects may cause a significant radial component of the relative wind velocity, resulting in a local sweep or yaw angle (Leishman, 2006). Although Maresca (1981) and McCroskey and Fisher (1972) stated that the crossflow component had a negligible effect on the qualitative aspects of dynamic stall, Leishman (2006) and Gardner (2012), the latter of whom conducted simulations with 2D and 3D code and also wind tunnel experiments, described some important quantitative effects. Leishman (2006) described how when the crossflow conditions described above are combined with a high angle of attack, these larger sweep angles have favourable effects on the spanwise development of the boundary layer, which tend to delay the onset of flow separation to higher angles of attack, reduce the strength of the LEV, produce much higher lift coefficients and promote flow reattachment on the down stroke. Gardner (2012) found that a stronger trailing-edge vortex in the rotating case caused the reduction in strength of the LEV. The effects associated with wing sweep are only significant in the separated flow regime, the overall effect being to provide an increase in rotor thrust. Moment stall was observed to take place at the same angle of attack, but the minimum pitching moment was reduced in magnitude by 25% and delayed to a higher angle of attack. The delay in moment peak suggests that the delay in dynamic lift stall in swept flow is due in part to the lower speed at which the LEV is convected over the chord, which reduces the slope of the lift curve

and increases the lift peak magnitude. The lift peak took place earlier than the moment peaks and was separated further in time than the non-rotating case (Gardner, 2012).

Near the blade tip, the tip vortex effectively reduces the angle of attack, inducing a gradual reduction in lift curve slope along with a decrease in the depth of dynamic stall which is effective in the outboard third of the rotor (Gardner, 2012), with increasing effectiveness at the outboard end is approached. While modelling of the tip vortex would require a 3D rotor blade, this has been found by McCroskey and Fisher (1972) to be unnecessary as the dynamic stall characteristics of 3D finite wings are qualitatively similar to those of oscillating 2D airfoils. However, Shreck and Pack (1994) found that a finite wing had a marked impact on LEV convection, resulting in no convection at the tip and faster convection at the blade root. Bousman (1998) supported these observations of stall occurring at different locations on the azimuth for the first stall cycle, but noted that the second and third stall cycles occurred at the same azimuth across the blade as shown in Figure 1.8, Spentzos *et al.* (2005) also found evidence of interaction between the tip vortex and LEV, and that a 2D model only approximates 3D results near the middle of the rotor blade span.

Blade-vortex interaction (BVI) considers the rotor blades interacting with the wakes of other blades during rotation, and represent another field of research due to the complexities involved in that phenomenon. Modelling of BVI requires the entirety of the helicopter rotor to be modelled, and is not practical for the type of simulation being considered in this research.

Bousman (1998) found that the general sequence of dynamic stall was the same in 2D models as in flight conditions of the UH-60. It is believed that the first stall cycle begins inboard on the blade due to an increase of the angle of attack caused by airflow over the forward fuselage, though there is no evidence of an influence of the fuselage on dynamic stall in the downstream quadrants of the rotor azimuth. The wake of the remainder of the helicopter, including fuselage and rotor hub but also interaction between the main rotor blades and tail rotor vortices, also have an effect which is not modelled in this simulation.

### **2.3.1.3 Pitch Axis Location**

The pitch axis location determines the proportion of the airfoil that is moving against the relative airflow, which influences the pressure distribution on the airfoil and whether the airfoil extracts energy from the flow or does work on the flow (Visbal and Shang, 1989). Most research considers a pitch axis location of 1/4-chord aft of the leading edge, as this is the position of the aerodynamic center for angles of attack below static stall, about which pitch is constant with a value of zero for symmetric airfoils in the linear range of the lift curve (Brandt *et al.*, 1997). Therefore, the aerodynamic center is the optimal location for the pitch axis since it minimizes loads on the rotor pitch links. McAlister *et al.* (1978) noted that although the center of pressure location coincides with the aerodynamic center at angles below stall, as the angle of attack approaches stall the center of pressure, the point at which moment is zero, moves toward the mid-chord, then forward of the pitch axis during stall recovery. Jumper *et al.* (1989) and Visbal and Shang (1989) found that stall can be delayed by displacing the pitch axis aft, and that this delay is proportional to the pitch rate. Stall delay due to pitch axis location also reduced

the strength of the LEV and the magnitude of the aerodynamic forces including  $C_{lmax}$ . The position of the pitch axis also determines if the  $C_{lmax}$  increases or decreases with increases in  $k$ , however it does not affect the LEV convection speed.

### 2.3.2 Dynamic Similitude

Traditional Reynolds Number and Mach Number similarity, required for all CFD simulations, are required for dynamic stall simulations as well. However, they are secondary in importance relative to airfoil motion parameters.

#### 2.3.2.1 Reynolds Number Similarity

The Reynolds number, the ratio of inertial to viscous forces, is given by Reynolds (1883) as

$$Re = \frac{Uc}{\nu} = \frac{\rho Uc}{\mu} \quad (2.2)$$

Where  $c$  is the airfoil chord, and  $\mu$  and  $\nu$  are the dynamic and kinematic viscosity of the fluid, respectively. The Reynolds number influences whether the LSB will form or not, as can tripping of the boundary layer either deliberately or otherwise to simulate higher  $Re$ , by means of such disturbances as vibration, surfaces discontinuities, or surface contamination (Saxena *et al.*,1978). Sharma and Poddar (2010) identified the effect of increasing  $Re$  was to reduce the size of the LSB, the boundary layer transition takes place closer to the separation point, the strength of the transition is reduced, and the reattachment point is promoted upstream. Changing the  $Re$  had no effect on the separation point location. These observations have consequences for the boundary layer

and LSB, however, the LSB has been shown to have minimal impact on the aerodynamic loads at flight Reynolds number and frequency (Carr *et al.*, 1977), and Feszty *et al.* (2004), McCroskey *et al.* (1976), Carr *et al.* (1977), Panda and Zaman (1994), and Saxena *et al.* (1978) found that the mechanism of dynamic stall (i.e., the formation of the LEV) is largely independent of  $Re$ . Martin *et al.* (1974) found that quantitatively, increases in  $Re$  increase peak lift and pitching moment magnitudes, and delays dynamic stall. A study of Reynolds number effects was not conducted as part of this research since flight Reynolds conditions could be duplicated numerically, to be representative of actual helicopter rotor blade airflow. Chandrasekhara and Carr (1994) found that any tripping of the boundary layer increased the momentum thickness of the boundary layer, reducing the adverse pressure gradient that can be withstood before stall – a factor that must be considered in experiments.

### 2.3.2.2 Boundary Layer Transition

Leishman (2006) stressed that accurate prediction of boundary layer transition is a key issue, a position supported by Barla *et al.* (2005) who suggested that transition effects have non-negligible effects on unsteady flow characteristics for  $Re < 10^5$ . Geissler *et al.* (2005) and Ekaterinaris and Menter (1994) also found that transition modelling. may have an important effect on simulated data, and noticed improvements when even simple transition modelling. was used. McCroskey *et al.* (1976) and Carr *et al.* (1977) studied airfoils with both clean and tripped boundary layers and found that neither the qualitative flow characteristics nor the quantitative loads were greatly different, though the time-history of the breakdown of the leading-edge flow and aerodynamic loads, and the stall

angle were affected by the state of the boundary layer and the presence of a LSB. It was also observed that the onset of stall was more irregular in the presence of a boundary layer trip.

### 2.3.2.3 Compressibility Effects

The Mach number must match the flow being simulated in compressible flows, and is given by

$$M = \frac{U}{a} = \frac{U}{\sqrt{\gamma RT}} \quad (2.3)$$

where  $a$  is the speed of sound,  $\gamma$  is the ratio of specific heats,  $R$  is the specific gas constant and  $T$  is the temperature. Dynamic stall occurs over a range of Mach numbers, from below 0.3 for the first cycle to over 0.8 for the third cycle (Bousman, 1998). Compressibility effects appear at Mach numbers as low as 0.2-0.3 (Carr and Chandrasekhara, 1996, Chandrasekhara and Carr, 1990 and 1994). Leishman (2006) indicated that while qualitative features of dynamic stall do not change significantly over a range of Mach numbers, there are variations in the quantitative behaviour, variations which are amplified for different airfoil shapes and under 3D conditions. Carr and Chandrasekhara (1996) explained that the physics of the stall process can change significantly between low and high Mach numbers, casting doubt over the applicability of low speed testing to high speed applications.

Quantitatively, as Mach number increases the magnitude of the critical adverse pressure gradient is reduced, promoting flow separation, LEV formation and dynamic stall to lower angles of attack, thereby reducing LEV strength and  $C_{lmax}$  (Lorber and

Carta, 1987, Chandrasekhara and Carr, 1990 and 1994, and Gompertz *et al.*, 2012). At higher Mach numbers, shock waves near the leading edge can cause flow separation to take place and increase the complexity of center of pressure behaviour during boundary layer separation and reattachment (Leishman, 2006).

Bowles *et al.* (2012) used a Hilbert transform to time-resolve the pitching moment recorded from experiment, and found periods of negative aerodynamic damping in flow conditions previously thought to have been positive in cycle-integrated damping. For instance, attached flow, which was identified above as having positive damping regardless of Mach number, however the time-resolved analysis showed there was negative damping during the pitch-up motion at low  $k$  and compressible Mach numbers. A travelling lambda shock wave on the upper airfoil surface was responsible for the negative damping, not only in attached flow but also in light and deep dynamic stall. Bowles *et al.* (2012) also observed that at the beginning of the pitch-up motion, formation and the start of convection of the LEV produced negative damping, until the LEV reaches the pitching axis where its effect becomes stabilizing. Convection of the LEV into the wake begins a period of positive damping which reaches a maximum when the flow fully reattaches. The time-resolved damping coefficient was very sensitive to the leading-edge roughness that was tested.

### 2.3.3 Kinematic Similitude

Kinematic similitude requires that a model and the application it is modelling. are exposed to similar unsteady motions. This is accomplished by matching the amplitude

and frequency of oscillation (the reduced frequency), the type of motion and the variable freestream. These parameters are generally more dominant in terms of their effect on the airflow than the parameters described in the preceding sections.

### 2.3.3.1 Angle of Attack: Mean, and Oscillation Amplitude

The combination of the mean and oscillatory amplitudes to the maximum angle of attack is to influence the depth of stall, moving from attached flow to light and finally deep stall as the maximum angle of attack increases, with the accompanying effects as described above. Lee and Gerontakos (2004) found that the peak aerodynamic loads did not change significantly as a function of oscillation amplitude when the maximum angle of attack remained constant. The influence of mean angle of attack on torsional damping depends greatly on the stall regime; in attached flow, increasing the mean angle of attack increases positive damping. Once light stall begins, increasing the angle of attack decreases damping. At the onset of deep stall, damping increases with an increase in angle of attack.

### 2.3.3.2 Frequency of Oscillation

The frequency of oscillation of the airfoil, one of the most significant parameters affecting dynamic stall (McAlister *et al.*, 1978), is measured by the dimensionless parameter known as reduced frequency, an indication of a measure of unsteadiness of a motion, which is given by

$$k = \frac{\Omega c}{2U} \quad (2.4)$$

where  $\Omega$  is the rotational frequency of the airfoil. Airflow is steady at  $k = 0$ , and becomes increasingly unsteady as  $k$  is increased. Dynamic stall begins to occur outside of the quasi-steady regime, defined as  $k < 0.05$  (Leishman, 2006).

The pitching motion of the airfoil influences dynamic stall by inducing a linear distribution of velocity normal to the chord, as opposed to plunging motion which has a constant distribution across the chord. The effect of the linear distribution is known as induced camber, which delays dynamic stall formation (Leishman, 2006). An increase in the reduced frequency will delay the onset of stall due to an increase in the magnitude of the critical adverse pressure gradient (Chandrasekhara and Carr, 1995) and reduce flow separation. Induced camber and LEV shedding affect the flow in that increasing the reduced frequency increases LEV strength, peak load magnitudes, hysteresis and dynamic stall angles. Increased reduced frequency also delays the formation and shedding of the LEV and flow reattachment and relaminarization. Carta *et al.* (1977) found that, at high mean angles of attack, aerodynamic damping increases with an increase in  $k$ , then decreases before continuing to increase again. This is consistent with the passage from attached flow to light stall and then deep dynamic stall. A high enough frequency can prevent flow separation altogether (Gerontakos, 2008). McAlister *et al.* (1978) suggested that LEV strength could be related to airfoil circulation at the instant of formation, which is consistent with the statements above since either an increase in reduced frequency or a delay in LEV formation to a higher angle of attack (for a sinusoidally variable pitch angle) will result in an increase in pitch rate, increasing circulation.

Martin *et al.* (1974) observed through experimental testing that the LEV shedding occurred at  $\alpha_{max}$  for low-amplitude, high-frequency oscillations, and suggested that this type of behaviour is not consistent with conditions representative of helicopter flight. This conclusion emphasizes the importance of accurately modelling the pitch rate in any research on dynamic stall. For an airfoil with a linear as opposed to sinusoidal change in pitch, the pitch rate replaces the reduced frequency as the measure of unsteadiness, and increase in pitch rate causes similar effects as an increase in  $k$ . Francis and Keesee (1985) conducted an experimental investigation that showed that increases in pitch rate had the effect of increasing the lift-curve slope, contrary to the results of Lorber and Carta (1987) and Jumper *et al.* (1987) who determined that the slope should be depressed with increasing pitch rate.

### 2.3.3.3 Types of Motion

As discussed in the introduction, a helicopter rotor blade is constantly moving along multiple axes: rotation about the hub and, in forward flight with a fully-articulated rotor, flapping, lead/lag, and pitching about the blade root. The superposition of these motions is periodic and complex, as shown in Figure 2.4. Two types of motion must be selected in modelling actual airfoil behaviour: the means of generating the time-variable change in pitch, and the motion schedule for that change in pitch.

### 2.3.3.4 Variable Pitch: Motion Schedule

The motion schedule is typically a linearly variable (ramping) or sinusoidal oscillatory change in angle of attack with respect to time. Figure 2.4a shows the ability of

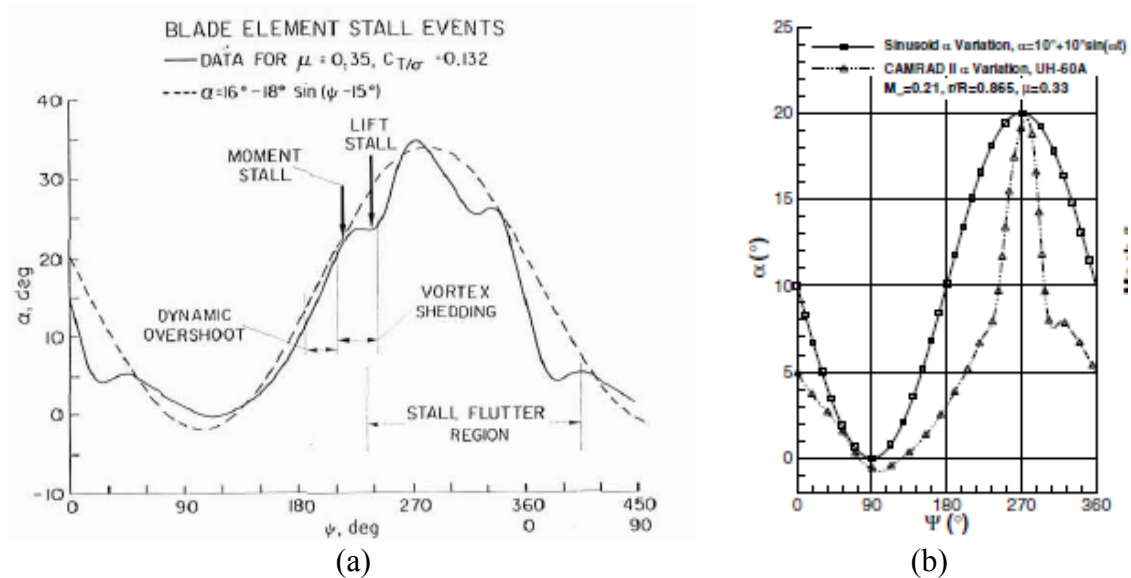


**Figure 2.4:** Comparison of (a) model rotor and (b) UH-60A rotor blade movement to ramp and sinusoidal rotation. Reproduced from (a) McCroskey and Fisher (1972) and (b) Kerho (2007).

sinusoidal angular motion to model the behaviour of a model rotor. It is clear from the figure that while the airfoil pitch behaviour approximates linear ramp motion for some of the pitch-up motion, sinusoidal motion is a superior model for the entire azimuth of rotation.

Oscillating motion is the more complex of the two due to the variable pitch rate and time history effects, the latter of which being a result of the down stroke motion. Kerho (2007) also compared sinusoidal motion to the motion of a real helicopter blade, a UH-60. It was found that, as shown in Figure 2.4b, throughout the majority of the azimuth the reduced frequency of the UH-60 airfoil was effectively lower than that of the reference sinusoid. The notable exception was between approximately  $\psi = 225^\circ$  and  $\psi = 315^\circ$  where the reduced frequency of the UH-60 airfoil was effectively triple that of the sinusoid. The effect of this change in schedule is similar to a change brought about by an

increase in reduced frequency. The induced camber effect discussed above is only applicable to a motion schedule with a variable pitch rate.

### 2.3.3.5 Variable Pitch: Translation Versus Rotation

A helicopter rotor blade realistically undergoes both plunging motion and pitching motion, due to blade flapping and cyclic input, respectively. In numerical and experimental models, the pitch variability is typically generated by either vertically translating an airfoil section (also known as pure pitching or plunging motion) with constant incidence or by varying the pitch without translating the airfoil. The differences between these two types of motion are shown in Figure 2.5.

Carta (1979) conducted experiments to compare the response of the airflow caused by pitching and plunging airfoil motion. In attached flow where hysteresis was present, it was found that the damping was positive for pitch and negative for plunge motion. The hysteresis loops grew more rapidly for plunge motion below stall penetration. In conditions of light stall, the plunging response differed in shape and magnitude from the pitching case; the pitching case produced larger loops and the plunging case did not show signs of dynamic stall. The plunge lift-curve slopes were also greater than those of the pitching motion, resulting in overprediction of the lift by up to 50%. In conditions of deep stall, dynamic stall effects are not present near the leading edge during plunging

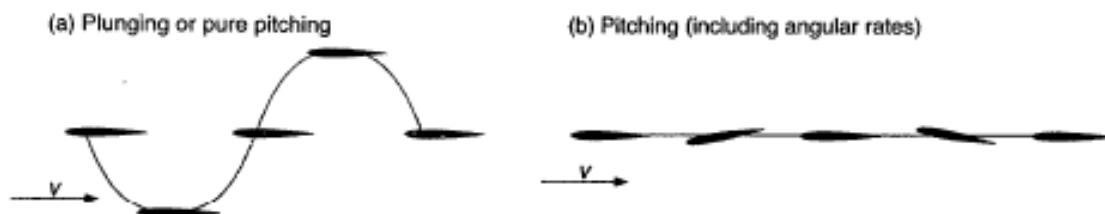


**Figure 2.5:** (a) Plunging and (b) pitching airfoil motion, reproduced from Leishman (2006).

motion, though the responses in the aft section of the airfoil under both types of motion are similar. The time histories are substantially different in the deep stall regime as well. Ericsson and Reding (1988) identified the lack of accelerated flow effect in plunging motion as being responsible for some of the difference in behaviour, described in additional detail below.

The selection of the type of airfoil motion used to induce a variable angle of attack – either pitching motion or plunging motion – has an influence on the aerodynamic damping. The pitch rate effects in pitching motion contribute to non-circulatory moment, increasing the size of the counterclockwise pitching moment loop in attached flow compared to that of a plunging motion (Leishman, 2006).

Plunging motion is used for eliminating the effect of pitch acceleration (Leishman, 2006), and despite this simplification which does not consider downstroke motion time history, it still displays many dynamic stall characteristics and was used by Gerontakos (2008). Regardless of the motion schedule selected, Leishman (2006) wrote that the qualitative flow features do not change significantly. Maresca *et al.* (1981) elaborated further that for low  $k$  and reduced amplitude, (plunging) results are comparable to pitching airfoil.

The freestream airspeed variability is measured using the reduced amplitude parameter,  $\lambda$ , for a plunging airfoil is given by

$$\lambda = \frac{A \Omega}{U} \quad (2.5)$$

where  $A$  is the amplitude of oscillation. For a pitching airfoil, the reduced amplitude is given by

$$\lambda = \frac{U_{\infty}}{U_{rot}} \quad (2.6)$$

In both cases, the variable freestream speed is given by

$$\frac{U(t)}{U_{rot}} = 1 + \lambda \sin \Omega t \quad (2.7)$$

### 2.3.3.6 Time-Varying Velocity

In forward flight, the combination of rotational and incident airspeed cause a blade element to encounter a time-varying incident velocity with additional unsteady aerodynamic effects. In attached flow, these effects include circulatory contributions from the nonuniform shed wake convection velocity, with additional noncirculatory contributions (Leishman, 2006). Experiments by Favier *et al.* (1988) suggested some considerable influence of varying freestream velocity on the dynamic stall process – flow conditions which will be investigated here. Favier *et al.* (1988) also found that the phasing of the velocity with respect to changes in angle of attack affect the formation of stall, however phasing other than that which is representative of helicopter flight conditions – where the angle of attack is a maximum at the minimum airspeed – will not be discussed here. Dynamic stall under variable freestream conditions is not completely understood, though it has been studied experimentally by means of choking upstream flow, fore-and-aft displacement of airfoil within test section, and numerically to a limited extent. This sub-section discusses some of the experiments and numerical modelling.

carried out to determine the effect of a time-varying freestream velocity on dynamic stall. In some cases an airfoil static in pitch was analyzed with a variable freestream, in others the two unsteady effects were combined.

Pierce *et al.* (1978) used a system of vanes downstream from the test section in a low-speed wind tunnel to choke the flow and thus produce a variable freestream magnitude. Pierce *et al.* (1978) obtained static data which was very different from the test case that was being duplicated, which was attributed to Reynolds number differences or surface roughness. It was concluded that the varying freestream had a significant effect on unsteady aerodynamic moment for airfoil pitching oscillations in vicinity of static stall, and that the unsteady freestream has little effect on aerodynamic work done on airfoil by freestream (the aerodynamic damping). Gompertz *et al.* (2012) also used choked exit vanes in a wind tunnel to produce a variable freestream near flight conditions, with  $M = 0.42 \pm 0.5$  and  $Re = 1.7 \times 10^6 - 2.8 \times 10^6$ . However, the reduced frequency was limited to 0.05, which despite being technically in the quasi-steady regime, managed to observe hysteresis of the aerodynamic loads. The experiment was limited to varying the freestream magnitude and angle of attack separately, though the author stated an intention to combine the two motions in the future. Gompertz *et al.* (2012) also made use of a S805 airfoil, results for which are not widely available, possibly because Somers (1997) identified this airfoil as having been designed specifically for horizontal wind turbines, and is therefore less generally applicable than the NACA 0012. A similar variable freestream-only study was conducted by Saxena *et al.* (1978), who found that the static stalling angle was not changed in the presence of a variable freestream. At low oscillation

frequencies, the behaviour was quasi-steady though the LSB was particularly sensitive to variations in the freestream. The magnitude of the unsteady pressure gradient was found to be a function of the reduced frequency and amplitude ratio. Brendel and Mueller (1987) found that laminar separation takes place with transition to turbulence occurring in the separated shear layer. Energetic mixing causes the turbulent free shear layer to reattach as turbulent boundary layer, forming a closed region known as the transitional separation bubble. Ellsworth and Mueller (1991) used a ramp speed deceleration profile and found that the LSB position in the chordwise direction opposite to that which it would respond in the presence of a quasi-steady change in speed. The point of transition was found to be more sensitive to flow acceleration than the separation point. Kerstens and Williams (2012) also used shutters downstream. Gompertz *et al.* (2011) determined the speed of propagation of the wave of speed variation upstream from the shutters. A variation on the more popular use of downstream shutters, Foresman (1974) used shutters upstream of the fan, and explained how the period of oscillation is controlled by the rotational speed of the vanes, and the amplitude of freestream oscillation is controlled by the blade width and resulting choke area.

Other researchers used a translating as well as plunging (Maresca *et al.*, 1981) or pitch-oscillating (Favier *et al.*, 1988 and 1992) airfoil in the test section to achieve the effect of a variable freestream. It was observed that above static stall angle, effects of the unsteady freestream are strong and depend on frequency and amplitude of velocity fluctuations. Although the translating airfoil model is relevant since the airfoil does physically translate due to lead-lag around the azimuth, Gompertz *et al.* (2011)

highlighted that viscous and compressibility effects are not adequately modelled by this method of freestream variability. The range of attainable frequencies using this experimental method is also limited by mechanical complexity. Wong *et al.* (2013) conducted a series of flat-plate cases to compare the two approaches, and showed that an oscillating body in steady freestream produces different effects than a steady body in an oscillating freestream, due to differences in the acceleration and time-history effects of the wake.

Some numerical modelling of dynamic stall with a variable freestream has also been carried out. Gharali and Johnson (2013) used variable boundary conditions to produce the horizontal oscillations of the freestream velocity, and rotational motion of the complete domain to produce the pitch oscillations of the NACA 0012 airfoil. The numerical simulations of Gharali and Johnson (2013) were carried out for conditions of  $\alpha = 10^\circ \pm 15^\circ$ , and three ranges of Mach number: 0.026 – 0.060, 0.017 – 0.069 and 0.009 – 0.078. The numerical results supported the experimental findings above that the time-varying freestream velocity effects are most pronounced when the airflow is separated, and that the increase in lift caused by the dynamic pitching motion is further increased by the influence of the variable freestream when the pitch and speed increase in phase, with the opposite effect when the two are out of phase. Both cases increase the time in which the LEV develops, leading to the conclusion that increased LEV growth time will affect the loads depending on the force history before the stall due to the maximum freestream velocity timing. Shi and Ming (2008 and 2009) conducted experiments on a delta-wing vehicle at  $\alpha = 0^\circ - 30^\circ$  and  $0^\circ - 60^\circ$ , and Mach 0.011 – 0.052 and found that the slowing

freestream speed during pitch-up can delay dynamic stall and increase  $C_{lmax}$ . The accelerating freestream on the downstroke also delays the reattachment, the combined effect being to enlarge the hysteresis loops. Kerho (2007) used a deforming mesh to vary the incidence of a SSC-A09 airfoil which was exposed to sinusoidal velocity oscillations and also an angle of attack schedule representative of a UH-60 aircraft. The effect of the change in angle schedule was to delay in separation of the LEV, increase  $C_{lmax}$ , and increase the loss of lift following lift stall. The effect of variable Mach number was to increase both lift during the upstroke and the  $C_{lmax}$ . The increase in lift is attributed to compressibility effects, though this could be dependent on the choice of steady Mach number that was used for comparison – it was less than the average of the variable component of the velocity. At the maximum angle of attack though, the Mach number was less than the steady Mach value leading to a delay in shock-induced separation and thus higher  $C_{lmax}$ . It was found that the  $C_l$  curve was nonlinear on the upstroke as a result of the continuously changing Mach number. Martinat *et al.* (2009) also used numerical methods, replicating the experimental results of Pascazio (1995) a pitching and horizontally oscillating airfoil was used, and the two oscillations were in phase.

The freestream Mach numbers and angles of attack for which the aforementioned analyses were carried out are summarized in Table 2.2. Note that some of these investigations were at multiple, fixed angles of attack whose scope was limited to the effect of the variable freestream in isolation of a changing angle of attack.

**Table 2.2:** Summary of test conditions for variable freestream investigations.

Reference	Type of Investigation	$M$ Range [-]	AOA Range [°]
Pierce <i>et al.</i> (1978)	Experimental	0.031 – 0.044	6, 10 14 ± 4 18 ± 4
Saxena <i>et al.</i> (1978)	Experimental	0.029 – 0.043	10 – 15
Maresca <i>et al.</i> (1981)	Experimental	0.007 – 0.058	15 ± 10 20 ± 17
Brendel and Mueller (1987)	Experimental	0.013 – 0.015	-5, 0, 7
Favier <i>et al.</i> (1988)	Experimental	0.007 – 0.058	6 ± 6 12 ± 6
Ellsworth and Mueller (1991)	Experimental	$3.9 \times 10^{-5}$ – $4.4 \times 10^{-5}$	7
Favier <i>et al.</i> (1992)	Experimental Numerical	0.007 – 0.072	9 ± 6 12 ± 6 15 ± 6
Shi and Ming (2008)	Experimental	0.017 – 0.052	0 – 30, 0 – 60, 15 – 45, 30 – 60
Shi and Ming (2009)	Experimental	0.012 – 0.040	0 – 60
Gompertz <i>et al.</i> (2012)	Experimental	0.38 – 0.48	8 – 20
Kerstens and Williams (2012)	Experimental	0.008 – 0.032	0 – 20
Kerho (2007)	Numerical	0.34 – 0.76	10 ± 10
Martinat <i>et al.</i> (2009)	Numerical	0.011 – 0.018	12 ± 6
Gharali and Johnson (2013)	Numerical	0.009 – 0.078	10 ± 15

### 2.3.4 Fluidelastic Similitude

The tests conducted by Bousman (1998) on a full-scale helicopter found that the rotor blade underwent three stall cycles under certain conditions at different parts of the rotor azimuth, additional stall cycles which have not been widely studied. The second and third

stall cycles, which take place as shown in Figure 1.8 quadrants 4 and 1 respectively, were believed to be caused by the torsional dynamics of the rotor blade. Therefore, modelling of the structural mass and stiffness of a rotor blade, as well as its deflection and response due to interaction with the flow, is necessary to model all of the effects of dynamic stall.

## **2.4 Numerical Modelling of Dynamic Stall**

Given the inherent challenges of experimental testing of dynamic stall, extensive numerical studies of dynamic stall have been performed, though these are not without their challenges either. Dynamic stall aerodynamic loading predictions are used in comprehensive rotor analysis, and can be generated using a variety of means. Theoretical, semi-empirical and computational fluid dynamics unsteady Reynolds-averaged Navier-Stokes, Large-Eddy Simulation (LES) and Direct Numerical Simulation (DNS) approaches have been used to study the phenomenon.

### **2.4.1 Comprehensive Rotor Analysis**

Comprehensive rotor analysis combines aerodynamic, structural, dynamic and aeroelastic models to calculate performance, loading, vibration and acoustic characteristics of a helicopter in support of the parametric design of helicopters. These analyses require the coupling of many models, and to be of practical use the computational expense must be reasonable. Therefore, instead of much more expensive CFD computations, the aerodynamic models of these analyses make use of lookup tables of 2D airfoil data, corrected for unsteady aerodynamics. Corrections for dynamic stall are

carried out using semi-empirical models, some of which are described below (Bousman, 2000). These comprehensive rotor analyses, examples of which include Comprehensive Analytical Model of Rotorcraft Aerodynamics and Dynamics (CAMRAD) II (Johnson, 1998), SMARTROTOR (Cesnik *et al.*, 2004) and that of Dai *et al.* (2011), have aerodynamic models which use blade element momentum theory (BEMT) to determine the loads of a rotating system of rotor blades. BEMT is a combination of momentum theory and blade element theory. Momentum theory, formalized by Glauert (1935), treats the blade rotor system as a single disk with a pressure difference across it, and is useful as a first approximation for thrust and rotor power. However, it does not consider the local effects on each blade which would be useful for analysis and design of the blades themselves. Blade element theory is useful for blade design. It assumes that a rotor blade can be modelled as a series of 2D airfoil sections, accounting for 3D effects by applying empirical factors, and integrating the loads over the blade span (Leishman, 2006). The combination of these two theories, BEMT improves upon the modelling of inflow by treating dividing the rotor disk into a series of concentric annuli, and applying conservation equations to each annulus.

### **2.4.2 Theoretical and Semi-Empirical Approaches**

The approach to develop the underlying theory of dynamic stall began with Theodorsen (1935), using potential flow theory the Kutta condition. Equations were developed for both lift and pitching moment, each with a circulatory and a non-circulatory group of terms. The non-circulatory terms represent flow acceleration, and the

circulatory terms represent the influence of the shed wake. This theory, however, is applicable only to thin-airfoil small-amplitude oscillations since the viscous effects (flow reversal in boundary layer and formation of the LEV) that define dynamic stall and delay it to higher angles of attack are not considered, as concluded by McCroskey and Philippe (1975) in their study of an approach using thin boundary layer theory.

Ericsson and Reding (1988) developed an analytic method that uses static experimental data to predict the effect of separated flow on incompressible, unsteady conditions. Two flow features were identified as affecting the separation-induced unsteady aerodynamic loading. First, the quasi-steady delay to flow separation caused by the time lag of static loads with respect to the angle of attack and boundary layer improvement effects results in delayed stall and increased lift. The time lag is caused by contributions of circulation, convective viscous flow and the moving separation point. Accelerated flow, which is not applicable to plunging airfoils, and the effect of the change in airfoil pitch and forward-moving separation point (moving wall effects) improve the boundary layer. The second feature that was identified was the transient displacement of the separation point upstream during stall followed by formation and convection of the LEV. The model showed good agreement of aerodynamic damping loads with dynamic stall experiments, despite not predicting flow reversal within the attached boundary layer.

Leishman (2006) has devoted significant effort to the development of indicial methods, based upon the linearization of the flow as a function of the forcing condition using Duhamel's integral. An indicial function models unsteady flow as a series of step-

function disturbances. This method is faced with some limitations, including an inexact application to compressible flow and non-applicability to separated flow. Although recent improvements to the method by Jose *et al.* (2006) have extended its applicability to unsteady compressible flows with combined pitching and freestream speed oscillations, these improvements are still limited to speeds below the critical Mach number and  $k < 0.4$ . Speeds above the critical Mach number present a non-linearity due to the shock waves, and when  $k > 0.4$  the approximations in the non-circulatory terms become more significant, producing phase differences. The equations that model separated flow consist of the linear terms representing the attached flow regions and nonlinear terms model the separated region, therefore indicial methods which use superposition of linear terms are not able to model the post-stall period of dynamic stall, which is highly influenced by separated flow.

Two of the dynamic stall models used by the CAMRAD II aeromechanical analysis include those of Leishman-Beddoes (Leishman and Beddoes, 1989) and Office national d'études et de recherches aérospatiales (ONERA) équations différentielles linéaires (EDLIN) (Petot, 1989). The Leishman-Beddoes model uses unsteady thin airfoil theory to determine the unsteady but linear attached flow loads. To these are added the nonlinear loads determined from modelling of separated flow using Kirchoff-Helmholtz theory, which determines lift as a function of angle of attack and the flow separation point (Leishman, 2006). Finally, the influence of dynamic stall loads caused by the LEV are considered by modelling its formation, as a function of the leading edge pressure and Mach number, and convection over the chord and into the wake.

The ONERA EDLIN model is based on the original ONERA model of Tran and Petot (1981), which used nonlinear differential equations to determine loads in attached (linear) and dynamic stall (nonlinear) regimes, considering time-history effects. The ONERA model represents aerodynamic loads below stall with a first-order equation, and loads beyond stall by a second-order equation, as explained by McAlister *et al.* (1984). This model can be linearized easily, making it useful for comprehensive rotor analysis. Its coefficients are dependent on the freestream velocity, airfoil shape and angles of attack and incidence.

Although there are limitations to the current state of the art in analytical approaches to dynamic stall, such as the inability to consider locally variable freestream airspeed (Pierce *et al.*, 1978) and the current applicability to angles of attack below that of static stall (Saxena *et al.*, 1978), the appeal of the theoretical approach is to develop “predictive rather than post-dictive models” (Chopra, 2010). Whereas a “post-dictive” model must be validated experimentally and is only applicable to similar cases without further validation, predictive models are derived from first principles and applicable to all cases that satisfy the simplifying assumptions used. Theoretical models also assist in understanding the underlying physics of the phenomenon of dynamic stall. The semi-empirical models allow for computationally inexpensive determination of aerodynamic loads which is useful for applications such as fluid-structure interaction modelling when coupled with a BEM model, though these models suffer in accuracy due to the assumption of linear behaviour which is not valid for shockwaves and dynamic stall, and steady freestream speed which is not representative of the helicopter rotor blade

environment.

### **2.4.3 Navier-Stokes Solutions**

Given that the flight conditions of helicopter rotors are difficult to reproduce experimentally in all of their nonlinear complexity, numerical solutions to the full Navier-Stokes equations are the only way to completely model the behaviour (Leishman, 2006). However, the computational expense associated with CFD justifies continued work to find other, less expensive, means of predicting dynamic stall.

#### **2.4.3.1 Specification of the Flow Field**

Solutions of simplified Navier-Stokes equations using assumptions of inviscid (Euler) flow and steady, incompressible and irrotational flow (panel methods to solve potential flow) are invalid for use in investigating dynamic stall in the separated region, which is a highly unsteady phenomenon and is influenced by transition modelling of the boundary layer. Numerical modelling of an airfoil undergoing dynamic stall has been conducted by several researches using a variety of methods to conduct the simulations. Feszty *et al.* (2004) used the discrete vortex method, a particle tracking method, to model the flow since it avoids the necessity of a grid, and specification of a separation point is not required. This technique solves the two-dimensional Navier-Stokes equations in vorticity/stream function form, and uses a Lagrangian scheme to describe the convection of vortices released from the no-slip boundary at the airfoil surface.

#### **2.4.3.2 URANS and Turbulence Models**

Given the importance of turbulence and flow separation to the process of dynamic

stall, several researchers have investigated the selection of turbulence model for use with Unsteady Reynolds-averaged Navier-Stokes (URANS) approaches to CFD predictions of dynamic stall. Ahmadi *et al.* (2009) simulated a NACA 0012 airfoil at Reynolds numbers of  $9 \times 10^5$  to  $2 \times 10^6$  at a wide range of static angles of attack using various turbulence models and found that the shear stress transport (SST) model had the least modelling error with respect to experimental lift and drag, compared to the other models tested: Spalart-Allmaras (S-A), Local Linear Realizable (LLR),  $k-\omega$  and SST  $\gamma-\theta$ . While all models had difficulty with viscous drag and boundary layer modelling, drag was predicted more accurately at high angle of attack though lift prediction was less accurate in that range. It was noted that while most of the models performed well, the  $k-\omega$  model was less accurate at high angles of attack. Ko and McCroskey (1997) tested the Baldwin-Lomax, Spalart-Allmaras and  $k-\varepsilon$  turbulence models, respectively zero-, one- and two-equation models. The test case was relevant to dynamic stall, a NACA 0015 airfoil oscillating in attached flow, light and deep stall at  $M$  of 0.3,  $k = 0.1$  and  $Re$  of  $1.95 \times 10^6$ . It was found that none of the turbulence models performed well during deep stall, especially on the downstroke. In attached flow and light stall, the S-A and  $k-\varepsilon$  models agreed well, though the S-A underpredicted loads on the downstroke. Barla *et al.* (2005) also conducted dynamic stall simulations and found that the S-A model provided the most reliable results, as did the SST model until severe separation took place and the model generated unrealistically high and oscillatory hysteresis effects. Martinat *et al.* (2009) found that S-A overpredicted hysteresis, and it was outperformed by  $k-\varepsilon$  Chien as was URANS/Organized Eddy Simulation (OES). Gharali and Johnson (2013) selected the

SST model, though it is designed for fully turbulent flow but takes into account the transition in flow with a low-Reynolds number correction. Menter *et al.* (2003) makes reference to a low- $Re$  formulation of the SST turbulence model, developed by Esch and Menter (2003), which automatically changes between wall functions and resolution of the boundary layer based on  $y^+$  the dimensionless wall distance as defined in Equation (3.35). Ekaterinaris and Menter (1994) studied the performance of one- and two-equation turbulence models to predict massively separated flow, in which Baldwin-Barth, S-A (one-equation) and SST (two-equation) models performed best. In the light stall simulation, S-A underpredicted and Baldwin-Barth overpredicted flow separation, while the predictions of SST were best. The effect of transition modelling was noted in the formation of the LSB as discussed above.

### 2.4.3.3 Mesh Structure and Pitch Oscillation

The grid around the airfoil is typically designed as a rectangular domain or with a C-grid. The means of rotating the airfoil with respect to the airflow must be taken into account when selecting the mesh as well, and several methods have been employed. Ahmadi *et al.* (2009) and Lakey and Sangolola (2007) used a rectangular outer grid with a circular inner grid that included the airfoil and rotated within the outer grid, both structured. Barla *et al.* (2005), Ko and McCroskey (1997), Gharali and Johnson (2011 and 2013) used C-grid topology with a variety of means to change the pitch, including determination of a new grid for each time step, pitching of the entire grid, and oscillating the freestream boundary condition over a static mesh.

## 2.5 Summary of Literature Review and Motivation for Research

The discussion surrounding the mechanism of formation of dynamic stall identified the expected behaviour of the airfoil and the major vortical structures it generates while undergoing dynamic stall in a steady freestream. The presence and sequence of the moment and lift stalls, the changes in peak loads, the formation, convection and interaction between the LEV and TEV are important descriptors of the flow which will be used to compare the variable and steady freestream results. The quantitative discussion led naturally to stall flutter to introduce the concept of aerodynamic damping which is used to justify the importance of mitigating dynamic stall behaviour and to assist in quantitative comparison of the variable and steady freestream cases. With the description of the problem and recognition of its importance justified, the focus of the literature review shifted to a discussion of the parameters affecting dynamic stall and the extent to which it has an impact and is understood.

Dynamic stall is a complex 3D phenomenon, which involves time-variation of AOA and Mach number at high frequency, and is dependent on a number of parameters. Some of the most common simplifications are 2D flow, reduced Mach and Reynolds numbers, and a steady freestream. While the impact of these assumptions have been widely studied, the impact of a variable freestream has not been studied as thoroughly due to the difficulty of reproducing helicopter flight conditions experimentally. The effect of the variable freestream has the potential to be significant since it causes rapid fluctuations in Reynolds number, Mach number and reduced frequency, the latter two of which influence

dynamic stall significantly on their own. Just as many of the researches cited in this chapter carried out several simulations of various combinations of the other parameters described above, the purpose of this research is to study the impact of the variable freestream to improve the understanding of dynamic stall as researchers converge toward modelling all of the complexities involved with this phenomenon. However, it was important that the model used in such a study be accurate, therefore a review of best practices in modelling the phenomenon was carried out.

The numerical modelling section began with a discussion of the theory of dynamic stall and the limitations of theoretical models, to emphasize the importance of the underlying physics in applying simplifying assumptions to the model. The literature review favoured the use of URANS with the SST turbulence model, and published examples of other researchers using a variable freestream velocity boundary condition as a means of varying the angle of attack were identified.

To date, there have been CFD studies of a variable freestream but most of these considered low Mach and Reynolds numbers. Only one paper was found that considered flight conditions, and the simulation therein only considered the impact of the variable freestream on a non-sinusoidal angle of attack variation and an uncommonly used airfoil. Experimentally, there have not been any published results at helicopter flight conditions with both a variable freestream and angle of attack. The research conducted in this thesis will meet this need, using a widely used airfoil and a sinusoidal angle of attack oscillation which will allow the impact of the variable freestream alone to be assessed. This research will draw conclusions with respect to the applicability of models that do not consider a

variable freestream, and contribute to the body of knowledge related to dynamic stall, its formation and effects.

## **Chapter 3**

# **Numerical Method**

The first section of this chapter describes the test case used for the study documented in this thesis. The second section describes the software used to conduct the simulations. The third section the governing equations selected, including the turbulence model. The method of solving the governing equations is discussed in section four. Section five describes the parameters of the case. Section six outlines the steps taken to confirm solution fidelity. The seventh and final section describes the post-processing methods used.

### **3.1 Test Cases**

Two test cases were studied as part of this research. Case 1 featured a steady freestream with oscillating angle of attack in order to validate the computational model. Case 2, on the other hand featured a variable freestream, modified with parameters that

are more representative of real helicopter rotor blade motion. The parameters for these cases are presented in Table 3.1.

Note that since this thesis deals with 2D flows, the values shown in columns 3 and 4 are taken at 80% of the blade radius, where most of the lift is generated and where the flow is closest to 2D conditions. The symbols in the table below are defined by the equations above, the phase shift between angle of attack and freestream variation  $\varphi$ , and the angle of attack as a function of time which is given by

$$\alpha(t) = \alpha_0 + \alpha_1 \sin(\Omega t + \varphi) \quad (3.1)$$

Although, as it was noted in the literature review, true helicopter blade motion is not sinusoidal, a sinusoidal motion schedule was selected here for consistency since empirical models use sinusoidal motion schedules and not the true helicopter blade motion schedules.

The parameters of Case 2 were selected considering characteristics of the Westland Lynx, holder of the helicopter world speed record set in 1986 at 216.3 kts (Perry, 1987). The advancing tip Mach number was 0.977, the advance ratio was 0.5, the rotor radius was 21 ft, the chord 1.29 ft, and the nominal tip speed was 717.5 ft/s. Although the angle of attack range was not given for the Lynx, it was assumed to be consistent with the model CH-47 rotor of McCroskey and Fisher (1972) and the UH-60 (Kerho, 2007). These parameters were modified slightly for Case 2 to reflect characteristics of a more typical, yet high-speed helicopter flight as follows.

A fast helicopter with advance ratio,  $\mu$ , of 0.5 was selected. Considering a rotor tip

**Table 3.1:** Test case conditions.

Parameter [Units]	Case		
	Case 1: Reference Case (McAlister <i>et al.</i> , 1982, Frame 14210)	Case 2: Variable Freestream Case (Helicopter Representative)	Comparison: Westland Lynx, World Record Holder (Perry, 1987)
	Parameter Value		
$\alpha$ [deg]	15 ± 10	15 ± 10	10 ± 10, 15 ± 15
$U$ [m/s]	100.6	Average: 163.3 Min: 61 Max: 265	Average: 175 Min: 64 Max: 286
$M$ [-]	0.292	Average: 0.48 Min: 0.18 Max: 0.78	Average: 0.51 Min: 0.18 Max: 0.84
$\lambda$ [-]	0	0.625	0.636
$Re$ [-]	$3.76 \times 10^6$	Average: $3.31 \times 10^6$ Min: $1.2 \times 10^6$ Max: $5.4 \times 10^6$	Average: $4.65 \times 10^6$ Min: $1.7 \times 10^6$ Max: $7.6 \times 10^6$
$k$ [-]	0.1014	Average: 0.029 Min: 0.018 Max: 0.078	Average: 0.039 Min: 0.023 Max: 0.105
$f$ [Hz]	5.36	5.08	5.44
$c$ [m]	0.61	0.3	0.393
$\varphi$ [deg]	N/A	180	180

speed of Mach 0.6, this would correspond to a forward flight speed of Mach 0.3. Assuming that dynamic stall occurs between 0.77 and 0.92 $R$  (Leishman, 2006), 0.8 $R$  was selected as the rotor cross-section to be modelled in the 2D simulation. The rotational speed here will be 0.8 x Mach 0.6 = Mach 0.48. A chord length of 0.3 m was selected as being in the middle of the typical range (Leishman, 2006). A blade length of 6.4 m is assumed, that of the Westland Lynx. This yields a reduced frequency of 0.029, which interestingly corresponds to quasi-steady phenomenon, since  $k < 0.05$  (Leishman, 2006).

The NACA 0012 airfoil was selected. Despite modern helicopters using cambered airfoils often with different airfoil sections in various ranges of the blade span, NACA 0012 is still popular as a test case in research literature. This is also the reason why this range of angle of attack motion was selected; to enter the regime of deep stall and be comparable to other work.

The angle of attack and speed are 180 degrees out of phase, consistent with the airfoil response over the azimuth as shown in Figure 3.1. An analogous graph for Case 1 is shown in Figure 3.2.

## 3.2 OpenFOAM

For all simulations conducted in support of this thesis, OpenFOAM (Open Field Operation and Manipulation), an open-source CFD package written in C++, was used. This software employs a finite-volume discretization of the Reynolds-averaged Navier-Stokes equations. It is a three-dimensional, parallel code with built-in structured and unstructured mesh generators. OpenFOAM has been widely used by published peer-reviewed literature, and has advantages over other CFD software packages due to its open-source nature. However, documentation is less thorough than for other CFD software and it can be more difficult to learn and employ.

Some of the recent research that has made use of OpenFOAM for similar applications includes that of Bah *et al.* (2013), who studied dynamic stall of wind turbines using an incompressible solver, C-grid and the  $k-\omega$  SST turbulence model. Watrin *et al.* (2012)

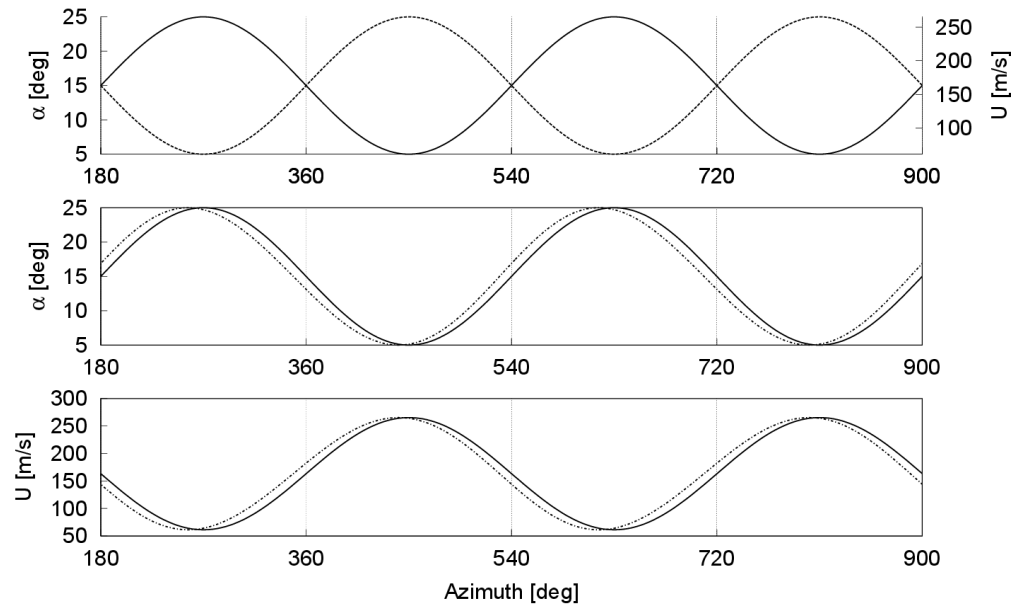


**Figure 3.1:** Variation of freestream magnitude and angle of attack as a function of azimuth for Case 2. Top image: solid lines indicates angle of attack, dashed line indicates freestream speed. Second and third images: solid lines indicate data at the airfoil, dashed lines indicate data at the inlet.

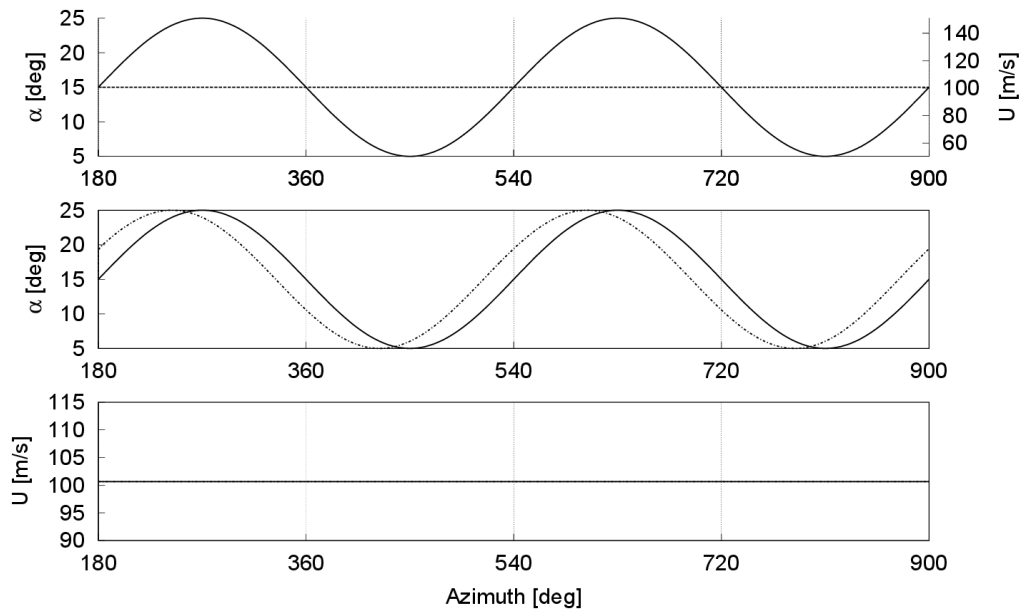


**Figure 3.2:** Variation of freestream magnitude and angle of attack as a function of azimuth for Case 1. Top image: solid lines indicates angle of attack, dashed line indicates freestream speed. Second and third images: solid lines indicate data at the airfoil, dashed lines indicate data at the inlet.

created a new solver and also used the  $k-\omega$  SST model to simulate stall flutter. In both cases, results compared well to experimental data. Nakao *et al.* (2014) conducted steady-state analyses of a 2D airfoil section using the solver “rhoCentralFoam” and found that the data agreed well with experiment at  $Re = 3.8 \times 10^6$  and  $M = 0.277$  and  $0.569$ . Additional external aerodynamics research using OpenFOAM has been published by Amiralaei *et al.* (2009), Gagnon *et al.* (2011), Gao *et al.* (2012), and Sumner and Masson (2012).

### 3.3 Governing Equations

In this section, the governing equations of the flow that will be solved using CFD will be identified. First the conservation equations with their auxiliaries, then the turbulence models and wall functions.

#### 3.3.1 Conservation and Auxiliary Equations

Versteeg and Malalasekera (2007) present the governing equations of the flow of a time-dependent, compressible Newtonian fluid as follows, in the integral conservative form, which is most useful for finite volume discretization:

$$\underbrace{\int_{\Delta t} \frac{\partial}{\partial t} \left( \int_{CV} \rho \phi dV \right) dt}_{I} + \underbrace{\int_{\Delta t} \int_A n \cdot (\rho \phi U) dAdt}_{II} = \underbrace{\int_{\Delta t} \int_A n \cdot (\Gamma \nabla \phi) dAdt}_{III} + \underbrace{\int_{\Delta t} \int_{CV} S_\phi dVdt}_{IV} \quad (3.2)$$

where  $\phi$  is a general variable representing the quantity transported by the equation, i.e.

either the scalar 1 for the continuity equation (conservation of mass); velocity components  $u$ ,  $v$ , or  $w$  for conservation of momentum (Newton's second law); internal energy  $e$ , temperature or enthalpy  $h_0$  for the energy equation (conservation of energy, or the first law of thermodynamics). The expression  $n \cdot x$  indicates the component of a vector,  $x$ , in the direction normal to a surface,  $A$ , in accordance with Gauss' divergence theorem.  $\Gamma$  is the diffusive coefficient, equal to dynamic viscosity for the momentum equations and the conductivity for the energy equation. The terms of the equation represent, in their order of appearance:

- Term I: The rate of increase of  $\rho\phi$  within the control volume;
- Term II: The net rate of decrease of  $\rho\phi$  due to convection across control volume boundaries;
- Term III: The net rate of decrease of  $\phi$  due to diffusion across the control volume boundaries; and
- Term IV: The net rate of production of  $\phi$  inside the control volume.

$S_\phi$  is the source term, given for each equation by:

$$\begin{aligned}
 S_1 &= 0 \\
 S_e &= -P \nabla \cdot U + \Phi + S_E - U \cdot S_M \\
 S_u &= \frac{-\partial P}{\partial x} + S_{Mx}; \quad S_v = \frac{-\partial P}{\partial y} + S_{My}; \quad S_w = \frac{-\partial P}{\partial z} + S_{Mz}
 \end{aligned} \tag{3.3}$$

where  $S_E$  accounts for potential energy effects,  $S_M$  and its components account for body forces such as gravitational forces, pressure and viscous stresses, and  $\Phi$  is the dissipation

function.

In conjunction with the following equations of state, used by assuming thermodynamic equilibrium, the governing equations of the problem are completely defined (Versteeg and Malalasekera, 2007):

$$P = \rho RT \quad (3.4)$$

$$e = C_v T \quad (3.5)$$

where  $C_v$  is the specific heat capacity at constant volume. The assumptions considered by the equations above are summarized as follows:

1. The fluid is in a state of thermodynamic equilibrium, which is valid except for flows with strong shock waves or rarefied flows. This assumption is required to provide sufficient equations to solve for the thermodynamic variables  $\rho$ ,  $P$ ,  $e$ , and  $T$ ;
2. The fluid is Newtonian, meaning the viscous stresses within the fluid are proportional to the rates of deformation, which is valid for air. This assumption is required to solve for the viscous stress components and introduces dynamic viscosity into the system of equations; and
3. The fluid behaves as an ideal gas, which is generally valid except for rarefied atmospheres at very high altitudes that are not considered by this analysis.

There are several further simplifications which are often made to the system of equations for other types of flow problem, but cannot be applied in this thesis since they

are required to properly model the flow conditions:

- Viscous flow. Modelling of the boundary layer and separated flow are fundamental to the study of stall, both static and dynamic.
- Compressible flow. Above Mach 0.3, compressibility effects begin to appear.
- Unsteady flow. Dynamic stall is by nature a transient problem, therefore a time-dependent solution is necessary. Despite the fact that Case 2 is in the quasi-steady regime, vortex shedding at high AOA is an unsteady phenomenon which requires unsteady modelling.

Therefore, a solution of seven equations with seven unknowns is required, and the problem is closed with the definition of initial and boundary conditions.

The URANS equations will be used, since these are effective in modelling external flow and are computationally less expensive than the alternative turbulence models. These alternatives are DNS, where turbulence is resolved at the Kolmogorov scale (Wilcox, 1994) without the use of turbulence models, and LES, where turbulent scales below a threshold set by a low-pass filter are modelled. For the purpose of the investigation at hand, though, URANS is a sufficiently accurate method, as will be shown through verification and validation of the results.

### **3.3.2 Turbulence Modelling**

The use of URANS implies dividing each flow variable of the Navier-Stokes equations into time averaged and fluctuating components, which generates additional

turbulent stress terms known as Reynolds stress terms. These terms require the addition of a turbulence model and its associated equations to define the problem.

The two-equation  $k$ - $\omega$  SST model was selected based on its proven performance for this type of application involving separated flow as discussed in the literature review and by Bardina *et al.* (1997). The Menter and Esch (2001) version of this model is implemented in the CFD solver, OpenFOAM.

The SST model is a two-equation turbulence model, which is a blend of the  $k$ - $\varepsilon$  (turbulent kinetic energy,  $k$ , and turbulent energy dissipation,  $\varepsilon$ ) and  $k$ - $\omega$  ( $k$  and turbulence dissipation rate,  $\omega$ ) models. The SST model makes use of the former model in the far field and the latter model near the wall, benefiting from the outstanding near-wall performance of the  $k$ - $\omega$  model without the potential errors from its freestream sensitivity (Menter *et al.*, 2003). It is an eddy viscosity ( $\mu_t$ )-based model, which assumes a relationship between the viscous and Reynolds stresses of a flow according to the Boussinesq approximation (Versteeg and Malalasekera, 2007). The turbulent kinetic energy equation is given by:

$$\underbrace{\frac{\partial \rho k}{\partial t}}_I + \underbrace{\frac{\partial \rho U_j k}{\partial x_j}}_{II} = \underbrace{\widetilde{P}_k}_{III} - \underbrace{\beta^* \rho \omega k}_{IV} + \underbrace{\frac{\partial}{\partial x_j} \left[ (\mu + \mu_t \sigma_k) \frac{\partial k}{\partial x_j} \right]}_V \quad (3.6)$$

The turbulent dissipation rate transport equation is given by:

$$\begin{aligned}
& \underbrace{\frac{\partial \rho \omega}{\partial t}}_I + \underbrace{\frac{\partial \rho U_j \omega}{\partial x_j}}_{II} = \\
& \underbrace{\frac{\gamma}{V_t} P_k}_{III} - \underbrace{\beta \rho \omega^2}_{IV} + \underbrace{\frac{\partial}{\partial x_j} \left[ (\mu + \mu_t \sigma_\omega) \frac{\partial \omega}{\partial x_j} \right]}_V + \underbrace{(1 - F_1) 2 \rho \sigma_\omega \frac{1}{\omega} \frac{\partial k}{\partial x_j} \frac{\partial \omega}{\partial x_j}}_{VI}
\end{aligned} \tag{3.7}$$

Versteeg and Malalasekera (2007) defined the meaning of the terms as follows for both equations, unless otherwise indicated:

- Term I: the rate of change of  $\rho k$  or  $\rho \omega$ ;
- Term II: transport of  $\rho k$  or  $\rho \omega$  by convection;
- Term III: rate of production of  $k$  or  $\omega$ ;
- Term IV: rate of disipation of  $\rho k$  or  $\rho \omega$ ;
- Term V: transport of  $k$  or  $\omega$  by diffusion; and
- Term VI: present only in the  $\omega$  equation, the cross-diffusion term, which originates from the conversion of the  $\varepsilon$  equation to the  $\omega$  equation.

Note that the effective diffusivity for  $\omega$  is consistent with Menter *et al.* (2003) - which corrected an earlier error in Menter and Esch (2001). Here,  $S$  is the invariant measure of the strain rate, the  $P_k$  terms are production limiters and other parameters are given by:

$$P_k = \tau_{ij} \frac{\partial U_i}{\partial x_j}, \overline{P}_k = \min(P_k; c_1 \beta^* \rho k \omega),$$

$$\mu_t = \rho \frac{a_1 k}{\max(a_1 \omega; S \cdot F_2)}, S = \sqrt{2 S_{ij} S_{ij}}, S_{ij} = \frac{1}{2} \left( \frac{\partial u_i}{\partial x_j} + \frac{\partial u_j}{\partial x_i} \right) \quad (3.8)$$

$$\tau_{ij} = \mu_t \left( \frac{\partial U_i}{\partial x_j} + \frac{\partial U_j}{\partial x_i} - \frac{2}{3} \frac{\partial U_k}{\partial x_k} \right) - \frac{2}{3} \rho k \delta_{ij} \quad (3.9)$$

The constants of Equations (3.6) and (3.7),  $\sigma_k$ ,  $\sigma_w$  and  $\beta$ , are calculated using the analogous constants from the equations for the  $k$ - $\omega$  and  $k$ - $\varepsilon$  models, upon which the SST model is based. The constants of each of these models are denoted by  $\sigma_{kx}$ ,  $\sigma_{wx}$  and  $\beta_x$  in Table 3.2, where  $x = \{1,2\}$  to denote constants of the  $k$ - $\omega$  model and  $k$ - $\varepsilon$  model, respectively. The values of these constants in the SST model are calculated from those of the other models according to the following relationship:

$$\varphi = F_1 \varphi_1 + (1 - F_1) \varphi_2 \quad (3.10)$$

where  $\varphi$  indicates  $\sigma_{kx}$ ,  $\sigma_{wx}$  and  $\beta_x$ .

The OpenFOAM implementation differs slightly from the Menter and Esch (2001) implementation by using the reciprocal values of the  $\sigma$  terms as in Menter *et al.* (2003), and by using 1.0 instead of 0.9 for  $Pr_t$ . The values of  $a_1$  and  $\kappa$  are given in Menter (1994).

where  $F_1$  and  $F_2$  are blending functions given by

**Table 3.2:**  $k$ - $\omega$  SST turbulence model constants.

$x$	$\sigma_{kx}$	$\sigma_{wx}$	$\beta_x$	$c_1$	$\beta^*$	$\kappa$	$\gamma_x$	$Pr_t$	$a_1$
1	0.85034	0.5	0.0750	10	0.09	0.41	0.5532	1.0	0.31
2	1.000	0.85616	0.0828	-			0.4403		-

$$F_1 = \tanh \left\{ \left[ \min \left[ \max \left( \frac{\sqrt{k}}{\beta^* \omega y}, \frac{500 \nu}{y^2 \omega} \right), \frac{4 \rho \sigma_{\omega 2} k}{CD_{k\omega} y^2} \right] \right]^4 \right\}, \quad (3.11)$$

$$CD_{k\omega} = \max \left( 2 \rho \sigma_{\omega 2} \frac{1}{\omega} \frac{\partial k}{\partial x_j} \frac{\partial \omega}{\partial x_j}; 1.0 e^{-10} \right)$$

$$F_2 = \tanh \left\{ \left[ \max \left( 2 \frac{\sqrt{k}}{\beta^* \omega y}, \frac{500 \nu}{y^2 \omega} \right) \right]^2 \right\} \quad (3.12)$$

where  $y$  is the distance from a cell to the nearest wall.

### 3.3.2.1 Wall Functions

Wall functions are used to approximate the boundary layer when the grid resolution is insufficient to fully resolve it, as is common with high-Reynolds number applications. In these simulations, wall functions were used for both  $k$  and  $\omega$ .

The wall function for  $k$  is given in the OpenFOAM source code as a zero gradient. The wall function for  $\omega$  is a blended viscous sublayer model given in Menter and Esch (2001), with the logarithmic term from Wilcox (1994):

$$\omega_1(y) = \sqrt{\left( \frac{6 \nu}{0.075 y^2} \right)^2 + \left( \frac{1}{0.3 \kappa} \frac{\sqrt{k}}{y} \right)^2} \quad (3.13)$$

where the first term is  $\omega$  in the linear (viscous) region, while the second term is  $\omega$  in the log-law region. Thus, the above equation is a blending function of the two, depending on the distance from the wall.

Menter (1994) recommended boundary condition values for  $k$ ,  $\omega$  and  $\mu_t$  as shown in

Table 3.3, where  $\Delta y_1$  is the distance to the first point away from the wall. The equation for  $\omega$  above simulated a smooth wall boundary condition for  $y^+ < 3$ , where  $y^+$  is the dimensionless wall distance.

### 3.4 Solution Method

The first three sub-sections of this section describe discretization schemes, solver algorithms and the solution of discretized equations. In the fourth sub-section, the breakdown of the case for parallel processing is discussed.

#### 3.4.1 Discretization Schemes

The purpose of equation discretization is to solve the governing equations numerically. This means converting the partial differential equations of Section 3.3 into algebraic form that can be represented as the following matrix equation:

$$[A][x]=[b] \quad (3.14)$$

where the OpenFOAM Programmer's Guide (2014) defines  $[A]$  as a square matrix containing the coefficients of the algebraic equations defining the problem,  $[x]$  as the column vector of dependent variables and  $[b]$  as the source vector, where each element of

**Table 3.3:**  $k$ - $\omega$  SST turbulence model boundary condition values.

Wall/Infinity	$\omega$	$k$	$\nu/\mu_t$
Wall	$10 \frac{6\nu}{\beta_1(\Delta y_1)^2}$ at $y=0$	0	Equation 3.8
Freestream	$(1 \rightarrow 10) \frac{U_\infty}{L}$	$\nu_{t_\infty} \omega_\infty$	$10^{-(2 \rightarrow 5)} \nu_\infty$

the  $[x]$  and  $[b]$  vectors represent the values at a discretized mesh node in the domain. This research will use an Eulerian specification of the flow field, modelled with the URANS equations and using a finite-volume discretization to model the relative airflow over the airfoil.

The OpenFOAM Programmer's Guide (2014) defines the finite-volume discretization equations as follows, as each term is first integrated and then linearized. Integration is performed by applying Gauss' theorem to the volume integral as follows:

$$\int_V \nabla \phi dV = \int_S dS \phi = \sum_f S_f \phi_f \quad (3.15)$$

where  $V$  and  $S$  are the volume and surface of integration, respectively, and  $f$  indicates values at a cell face.

This section describes the discretization schemes used for each term. A summary is provided later, in Table 3.4.

### 3.4.1.1 Laplacian term

Integration and linearization of the Laplacian term over the control volume is given by

$$\int_V \nabla \cdot (\Gamma \nabla \phi) dV = \int_S dS \cdot (\Gamma \nabla \phi) = \sum_f \Gamma_f S_f \cdot (\nabla \phi)_f \quad (3.16)$$

where  $\phi$  is the velocity flux ( $\rho U$ ) through a cell boundary and  $\Gamma$  is the diffusive coefficient. When the vector  $d$  between a cell of interest (subscript  $P$ ) and a neighbouring cell (subscript  $N$ ) is orthogonal to the plane that defines the face between them  $S_f$ , the

discretization is implicit as follows:

$$S_f \cdot (\nabla \phi)_f = |S_f| \frac{\phi_N - \phi_P}{|d|} \quad (3.17)$$

Additional terms are required for non-orthogonal meshes, as discussed in further detail by the OpenFOAM Programmer's Guide (2014). The corrected version of the scheme was used in this research, which is second-order accurate, unbounded and conservative.

### 3.4.1.2 Convection Term

The convection term is given by

$$\int_V \nabla \cdot (\rho U \phi) dV = \int_S dS \cdot (\rho U \phi) = \sum_f S_f \cdot (\rho U)_f \phi_f \quad (3.18)$$

where the face field  $\phi_f$  is evaluated using a central differencing scheme that is second-order accurate and unbounded:

$$\phi_f = f_x \phi_P + (1 - f_x) \phi_N \quad (3.19)$$

where  $f_x$  is the ratio of the distances between  $f$  and cell center  $N$  and the distance between the centers of cell  $P$  and  $N$ . Upwind and blended differencing schemes are also available.

### 3.4.1.3 Time Derivative

The discretization selected for the time derivative term is backward differencing, which is second-order accurate, is given by

$$\frac{\partial}{\partial t} \int_V \rho \phi dV = \frac{3(\rho_P \phi_P V)^n - 4(\rho_P \phi_P V)^o + (\rho_P \phi_P V)^{oo}}{2 \Delta t} \quad (3.20)$$

where the superscript  $n$  indicates the time step being solved for, “ $o$ ” refers to the data stored from the previous time step, and “ $oo$ ” to data stored from a time step before the last time step.

#### 3.4.1.4 Divergence

The divergence identified below differs from the convection term, Equation (3.18), in that the velocity does not appear in the term with the dependent variable. It is second-order and unbounded, given by

$$\int_V \nabla \cdot \phi dV = \int_S dS \cdot \phi = \sum_f S_f \cdot \phi_f \quad (3.21)$$

#### 3.4.1.5 Gradient

The gradient term is evaluated explicitly using a second-order, least-squares method. The following tensor is calculated as follows, by summing over the neighbouring points  $N$ .

$$G = \sum_N \frac{d \cdot d}{|d|^2} \quad (3.22)$$

then the gradient is calculated using this tensor as follows

$$(\nabla \phi)_P = \sum_N \frac{G^{-1}}{|d|^2} \cdot d (\phi_N - \phi_P) \quad (3.23)$$

#### 3.4.1.6 Surface Normal Gradient

The surface normal gradient is analogous to the laplacian discretization scheme, and is given by

$$(\nabla \phi)_f = \frac{\phi_N - \phi_P}{|d|} \quad (3.24)$$

The corrected formulation is used here, which explicitly corrects mesh non-orthogonalities, and is second-order, conservative and unbounded.

### 3.4.1.7 Interpolation

This section defines the schemes used for interpolation of some quantities from the cell centers to face centers. A second-order, total variation diminishing (TVD) scheme, is selected within OpenFOAM. TVD schemes are commonly used since they reach a solution without oscillation of the value, and are described further in Versteeg and Malalasekera (2007). The general form for the value at the east or downwind cell face,  $\phi_e$ , is given by

$$\phi_e = \phi_P + 0.5 \psi(r) (\phi_E - \phi_P) \quad (3.25)$$

where the neighbouring cell centers are given by  $E$  for east, and  $P$  for the current cell. Face values are given by  $e$  for east of  $P$ .

Flux limiters, such as van Leer, limit the influence of the convective flux on the discretized value. Flux limiters with constant values of 0 (upwind differencing) and 1 (central differencing) suffer from false diffusion and “wiggles” in grids that are too coarse (Versteeg and Malalasekera 2007). Other flux limiters are functions of  $r$ , the ratio of upwind- to downwind-side gradient, such as the van Leer scheme which is given by

$$\psi(r) = \frac{r + |r|}{1 + r} \quad (3.26)$$

### 3.4.2 Solver Algorithm

The solution algorithm selected is called “rhoCentralFoam”, which is described by the OpenFOAM User Guide (2014) and Greenshields *et al.* (2010) as a density-based solver which is based on the convective-diffusive schemes of Kurganov and Tadmor (2000). The density field is determined from the continuity Equation (3.2), and pressure is derived from density using the equation of state (3.4). This solver, for which more details are provided in the OpenFOAM source code, is transient, compressible, and viscous. The governing equations are solved in a segregated manner, iteratively.

### 3.4.3 Solution of Discretized Equations

After having identified and discretized the governing equations of the problem, a system of linear algebraic equations is produced that must be solved. This section describes the techniques used to solve these equations, a summary of which is presented in Table 3.4. Relaxation factors of 0.25 were applied to the energy equations,  $h$  and  $e$ , to improve stability.

The diagonal solver solves explicit systems of equations; a direct method. The smooth solver uses the Gauss-Seidel point-iterative indirect method. The iteration sequence for this method is given in Versteeg and Malalasekera (2007) by

$$x_i^{(k)} = x_i^{(k-1)} + \alpha \left[ \sum_{j=i}^{i-1} \left( \frac{-a_{ij}}{a_{ii}} \right) x_j^{(k)} + \sum_{j=i}^n \left( \frac{-a_{ij}}{a_{ii}} \right) x_j^{(k-1)} + \frac{b_i}{a_{ii}} \right] \quad (3.27)$$

$(i = 1, 2, \dots, n)$

where  $k$  is the iteration number,  $n$  is the number of equations and unknowns, and  $i$  and  $j$  indicate the equation being solved.  $\alpha$  is the relaxation factor,  $a$ ,  $b$  and  $x$  indicate elements of the matrices from Equation (3.14). The solver converges if the residual falls below the solver tolerance as indicated in Table 3.5.

### 3.5 Computational Setup

This section describes how the test cases identified in Section 3.1 were modeled in the CFD simulations. First, the computational domain was described, followed by the boundary conditions, the initial conditions, the computational mesh, the simulation time-step and duration and finally solution convergence criteria. The simulations were run on two types of machine, first a commercial desktop computer with a Core i7-2600K

**Table 3.4:** Summary of discretization schemes selected within OpenFOAM for the simulations of this thesis.

Term	Selected Scheme
Interpolation schemes (point-to-point interpolation of values)	Central differencing (linear interpolation) for all except reconstruct rho, U and T which used TVD (vanLeer)
Component of gradient normal to a cell surface	Corrected (explicit non-orthogonal correction)
Gradient	Cell limited least squares (second order)
Divergence	Gauss linear (second order, unbounded)
Laplacian	Gauss linear corrected (unbounded, second order, conservative)
Time	Backward (second order, implicit)
Fields which require generation of a flux	Pressure
Flux Scheme	Kurganov

**Table 3.5:** Summary of Solution Methods

<b>Discretized Equation</b>	<b>Linear Solver</b>
$\rho$	Diagonal
$\rho U$	
$\rho E$	
$U$	Smooth solver, smoother: Gauss-Seidel 2 Sweeps Tolerance $1 \times 10^{-9}$
$k$	
$\omega$	
$h$	Smooth solver, smoother: Gauss-Seidel 2 Sweeps Tolerance $1 \times 10^{-10}$

processor, with the mesh decomposed into four domains over four cores. Some of the simulations were then conducted on a Carleton University virtual computing laboratory cloud, with the mesh decomposed into eight domains over eight cores. The contents of the files used to define the case are provided in Appendix A .

### 3.5.1 Computational Domain

The physical problem was modelled with a quasi-two-dimensional mesh consisting of an inlet, which extends over the external boundary of the domain with the exception of the outlet, and the airfoil surface, as shown in Figure 3.3. The domain size was selected as 20 chord lengths (10 chord lengths radius around the airfoil). This size was selected to account for the propagation of information in all directions in subsonic flow, to avoid unphysical effects from the boundary conditions being in too close proximity to the airfoil.

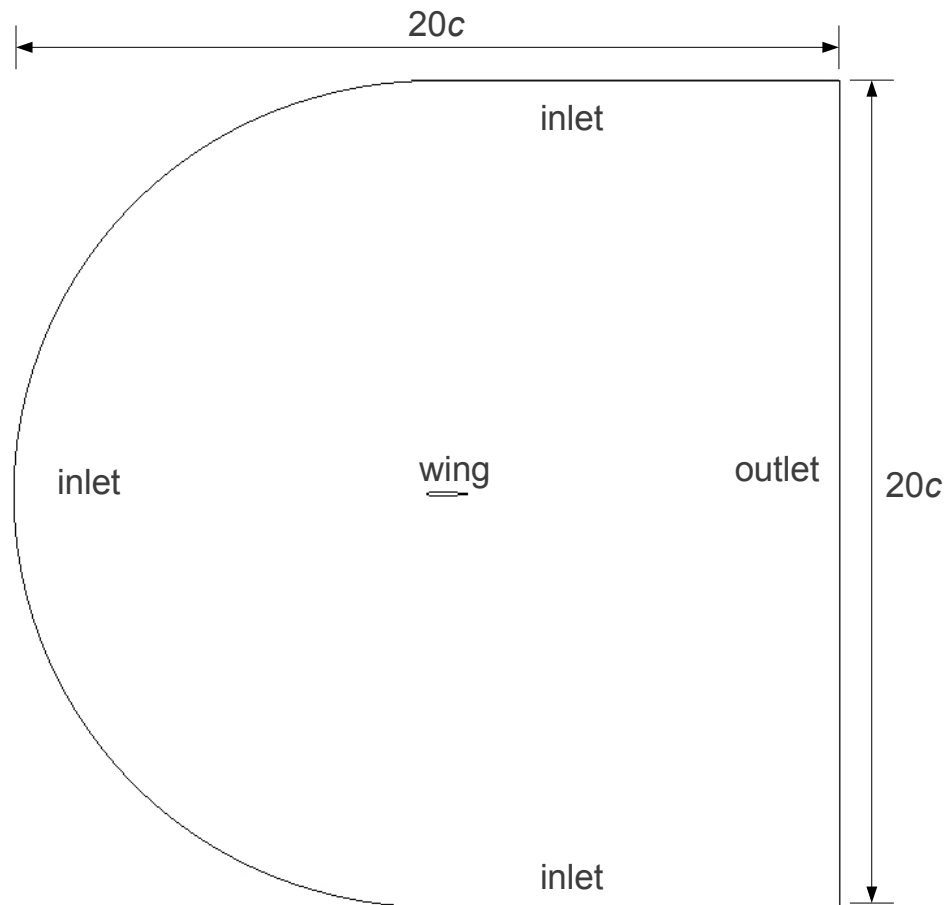


**Figure 3.3:** Computational domain, patches and domain size indicated.

### 3.5.2 Boundary Conditions

This section describes the boundary conditions employed for the spatial boundaries of the computational domain. The boundary conditions selected for the cases are defined in Table 3.6 and Table 3.7, for the boundaries that correspond to those illustrated in Figure 3.3. A description of the meaning and implications of each type of condition is specified below.

Proper specification of the boundary conditions is necessary for a well-posed

**Table 3.6:** Initial and boundary conditions applied. The constants indicated by the symbols in this table are provided for each case in Table 3.7.

Parameter [units]	Initial Conditions			
	Boundary Conditions			Internal Field
	Inlet	Outlet	Airfoil Wall	
$k$ [m <sup>2</sup> /s <sup>2</sup> ]	“FixedValue” uniform $k_\infty$	$\nabla \phi = 0$	“Compressible kqRWallFunction” uniform $k_l$	Same as Inlet
$\mu_t$ [kg/m·s]	“Calculated” uniform $\mu_t$	“Calculated” uniform $\mu_t$	“MulkWallFunction” $C_\mu$ 0.09, $\kappa$ 0.41, $E$ 9.8, value uniform $\mu_t$	Same as Inlet
$\omega$ [s <sup>-1</sup> ]	“FixedValue” uniform $\omega_\infty$	$\nabla \phi = 0$	“Compressible omegaWallFunction” uniform $\omega_l$ $C_\mu$ 0.09, $\kappa$ 0.41, $E$ 9.8, $\beta_l$ 0.075	Same as Inlet
$P$ [Pa]	$\nabla \phi = 0$	“WaveTransmissive” uniform $P$	$\nabla \phi = 0$	“Uniform” $P$
$\rho$ [kg/m <sup>3</sup> ]	“FixedRho” $\rho$	$\nabla \phi = 0$	$\nabla \phi = 0$	Same as Inlet
$T$ [K]	“InletOutlet” uniform $T$	$\nabla \phi = 0$	$\nabla \phi = 0$	Same as Inlet
$U$ [m/s]	“UniformFixedValue” tableFile	$\nabla \phi = 0$	“FixedValue” uniform (0 0 0)	Same as Inlet at $t = 0$ s

**Table 3.7:** Boundary and initial conditions: constants.

Parameter	Case	
	Case 1: Reference Case (McAlister <i>et al.</i> , 1982, Frame 14210)	Case 2: Variable Freestream Case (Helicopter Representative)
$k_l$ [m <sup>2</sup> /s <sup>2</sup> ]	1.5	1.5
$k_\infty$ [m <sup>2</sup> /s <sup>2</sup> ]	1.5	1.5
$\mu_t$ [kg/m·s]	0.14	0.14
$\omega_l$ [s <sup>-1</sup> ]	0.0035	0.0035
$\omega_\infty$ [s <sup>-1</sup> ]	52.074	52.074
$P$ [Pa]	101325	101325
$\rho$ [kg/m <sup>3</sup> ]	1.133	1.225
$T$ [K]	295.6	288.0
$I$ [%]	1.0	0.6

problem. Ill-posed problems may result in difficulty converging. Of the parameters  $P$ ,  $U$  and  $\rho$ , Laney (1998) stated that, for subsonic flow, two must be specified at the inlet and one at the outlet. Therefore,  $U$  and  $\rho$  were specified at the inlet and  $P$  specified at the outlet. The other parameters ( $T$ ,  $k$ , and  $\omega$ ) were all specified at the inlet as well.

Initial and boundary conditions were specified using three primary types of OpenFOAM boundary conditions: “fixedValue”, “inletOutlet”, and “zeroGradient”. The “fixedValue” boundary condition is a Dirichlet condition, where the value is fixed. The “zeroGradient” condition is a special case of the Neumann condition, in which the gradient of the parameter is fixed. With the “zeroGradient” condition, that gradient is fixed at zero. The “inletOutlet” condition is mixed, and alternates based on the direction of the velocity between a “fixedValue” condition when the direction of the flow is into the domain and a “zeroGradient” condition when the flow is directed out of the domain.

### 3.5.2.1 Inlet Boundary

The “inletOutlet” boundary condition was useful for some parameters defined at the inlet boundary, since for non-zero angles of attack the horizontal part of domain at either the top or the bottom would act as an outlet, as shown in Figure 3.3.

The “uniformFixedValue” boundary condition, a special case of the “fixedValue” boundary condition, was used for the  $U$  inlet, since it allowed for control of the inlet freestream speed as a means of modifying the angle of attack for Case 1, and both the angle of attack and freestream velocity magnitude for Case 2, as a function of time. However, neither the “uniformFixedValue” boundary condition, nor any other time-

varying boundary condition in the standard distribution of OpenFOAM, allow the boundary to behave in the manner of the “inletOutlet” boundary. Defining the airspeed when a part of the inlet boundary acted as an inlet may be the cause of unexpected effects at the top of the domain, which will be discussed in the Results chapter. A special case of the “inletOutlet” boundary condition, “timeVaryingUniformInletOutlet”, is available through OpenFOAM-extend, a version of OpenFOAM which includes contributions from the greater user community. This boundary condition functions as an “inletOutlet” condition with the added flexibility of varying the inlet value as a function of time where the flow exited the boundary. The “timeVaryingUniformInletOutlet” boundary condition was not used in this research, since its existence was not known until the cases were complete. An important point to note about the “uniformFixedValue” boundary condition is that it is not non-reflective; OpenFOAM only has two non-reflective boundary conditions, neither of which permits time-varying values. This limitation presented challenges which are discussed below. Changing the velocity boundary condition on a fixed geometry as a means of varying angle of attack has already been performed successfully by Gharali and Johnson (2012); this work extends the variation of velocity to include freestream magnitude. The velocity boundary condition reads the velocity from a lookup file, which was generated using a script according to the Equations (2.7) and (3.1).

### 3.5.2.2 Outlet Boundary

Parameters at the outlet were set using the “zeroGradient” and “waveTransmissive” boundary conditions. “ZeroGradient” was described above. The “waveTransmissive”

boundary condition is a non-reflective, mixed Robin condition, based on the Navier-Stokes Characteristic Boundary Condition (NSCBC) of Poinso and Lele (1992). It reproduces the non-reflective properties without full inter-field coupling, using Locally One-Dimensional Inviscid (LODI) – Euler – equations at the boundary. However, the “waveTransmissive” boundary condition is not perfectly non-reflective, and Pascaglia *et al.* (2013) developed a new condition with improved non-reflective performance, though this new boundary condition is proprietary to the company that funded its development and is not available for general use.

### 3.5.2.3 Airfoil (Wall) Boundary

The airfoil boundary uses a non-slip condition,  $U = (0 \ 0 \ 0)$ , for velocity, wall functions for the turbulence parameters ( $k$ ,  $\omega$ ,  $\mu_t$ ) and a zero gradient condition for all other parameters. The value of  $k$  near the wall is given by OpenFOAM's “kqRWallFunction” wall function, a zero gradient condition. The value of  $\mu_t$  near the wall is given by OpenFOAM's “mutkWallFunction” wall function, based on a rearranged version of the standard log-law of the wall given in Bredberg (2000):

$$\mu_t = \mu \left( \frac{y^+ \kappa}{\log(Ey^+)} - 1 \right) \quad (3.28)$$

where  $E$  is a constant with a value of 9.8. The value of  $\omega$  near the wall is given by OpenFOAM's “compressibleOmegaWallFunction” wall function, based on Menter and Esch (2001) as:

$$\omega_1(y) = \sqrt{\underbrace{\left(\frac{6\nu}{\beta_1 y^2}\right)^2}_{\text{viscous sublayer}} + \underbrace{\left(\frac{u_\tau}{\sqrt{C_\mu} \kappa y}\right)^2}_{\text{logarithmic region}}} \quad (3.29)$$

where the values of the constants are  $\beta_1 = 0.075$ ,  $C_\mu = 0.09$  and von Kármán's constant  $\kappa = 0.41$ , and the velocity profile near the wall is given by Wilcox (1994):

$$u_\tau = \sqrt{k} \sqrt{C_\mu} \quad (3.30)$$

The values of the boundary conditions for the turbulence properties were selected to achieve solution convergence. The values of  $P$ ,  $T$ ,  $\mu$  and  $\rho$  were selected to be similar to low-altitude atmospheric conditions, and adjusted to meet the  $Re$  and  $M$  of the case being modeled. The values are given in Table 3.6 and Table 3.7, along with resulting inflow turbulence intensity as calculated by Pope (2000)

$$I = \frac{u'}{U} = \frac{\sqrt{2k/3}}{U} \quad (3.31)$$

#### 3.5.2.4 Initial Conditions

The initial conditions correspond to the starting values for the simulations for the entire computational domain, including the boundaries as well as the internal field, at  $t = 0$ s. These are indicated in Table 3.6 and Table 3.7.

### 3.5.3 Physical Properties

Physical properties consist of thermophysical, thermodynamic and transport properties, and are identified below for the model used in this thesis.

### 3.5.3.1 Thermophysical Properties

Thermophysical models are related to energy and heat transfer. The thermophysical model used for each type of parameter is presented in Table 3.8. Sutherland's formula (Sutherland, 1893) is a temperature-dependent relationship for dynamic viscosity, given in the OpenFOAM Programmer's Guide (2014) as

$$\mu = \frac{A_s \sqrt{T}}{1 + T_s/T} \quad (3.32)$$

where the Sutherland temperature  $T_s$  and coefficient  $A_s$  are given in Table 3.9 (Fluent 2001) along with the values of the heat capacity at constant volume,  $C_v$ , and specific heat of fusion  $H_f$ .

### 3.5.3.2 Thermodynamic Properties

OpenFOAM requires the specification of  $C_v$  and  $R$ , with the values indicated in Table 3.9.

**Table 3.8:** Thermophysical model.

Parameter	Model Selection
Thermophysical Model	Compressibility-based thermophysical model
Mixture properties	Pure mixture
Transport Properties	Newtonian
Basic thermophysical properties	$C_p$ model which evaluates enthalpy and entropy
Equation of state	Perfect gas state equation
Derived thermophysical properties	Derived from heat capacity at constant pressure, enthalpy and entropy
Energy	Sensible, as opposed to absolute, energy: heat of formation is not considered.

**Table 3.9:** Thermophysical constants.

<b>Constant</b>	<b>Value</b>
Number of moles	1
Mole weight	28.9 g/mol
$C_v$	718 J/(g·K)
$H_f$	50 kJ/kg
$Pr$	0.707
$R$	287 J/(kg·K)
$A_s$	$1.46 \times 10^{-6}$ kg / (m·s·K <sup>1/2</sup> )
$T_s$	110.4 K
$C_p$	1005 J/(g·K)

### 3.5.3.3 Transport Properties

A Newtonian (linear) viscosity model was used, with  $\nu = 1.63 \times 10^{-5}$  m<sup>2</sup>/s (Case 1) and  $1.48 \times 10^{-5}$  m<sup>2</sup>/s (Case 2).

### 3.5.4 Spatial Discretization

The solution domain must be discretized into a mesh of nodes where the governing equations are solved. OpenFOAM's built-in “blockMesh” utility was used to generate a two-dimensional structured mesh. A script was written and executed using Octave to provide a flexible means of generating the input file for “blockMesh”.

The domain was divided into four blocks, as shown in Figure 3.4. Some of the blocks do not appear since they are thin and the domain is shown to scale. Figure 3.5 was included at an unrepresentative scale to illustrate the concept of these blocks. Blocks 1-3 are one cell thick around the airfoil, and were included to provide increased control over

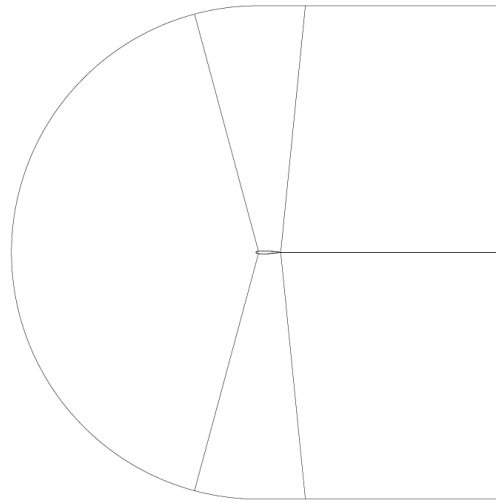


**Figure 3.4:** Layout of blocks that form the mesh.

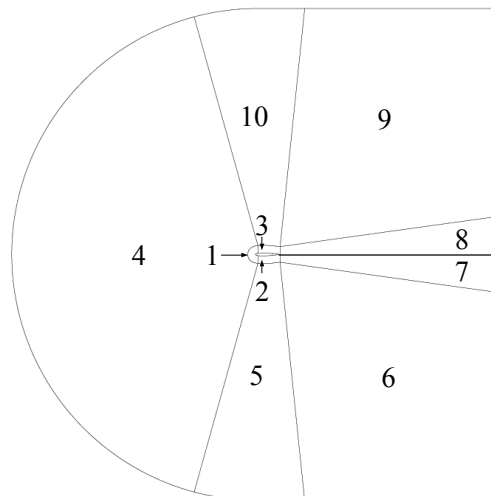


**Figure 3.5:** Layout of blocks that form the mesh. The sizes of blocks 1-3, 7 & 8 are exaggerated to illustrate the layout.

the spacing of the first cell from the boundary. Blocks 7 & 8 are along the centerline of the wake, and are present to control the interface of the downstream edge of Blocks 1-3 with the wake.

Once the blocks are defined, “blockMesh” requires the number of cells,  $n$ , and ratio of the first to last cell size along each edge,  $R$ , to be defined. These were calculated from

an expansion ratio,  $r$ , of 1.1 which was selected to ensure a small cell density gradient and promote stability, and the number of cells was calculated from this number and the desired distance from the wall to the first cell center to obtain the desired  $y^+$ . These calculations were performed using the following equations (OpenFOAM User Guide, 2014)

$$y_1 = l \frac{r-1}{Rr-1} \quad (3.33)$$

where  $l$  is the edge length and

$$r = R^{\frac{1}{n-1}} \quad (3.34)$$

The “yPlusRAS” utility in OpenFOAM calculates  $y^+$  as follows:

$$y^+ = C_\mu^{1/4} y_1 \sqrt{k} \frac{\rho_w}{\mu_w} \quad (3.35)$$

where  $k$  is the turbulent kinetic energy,  $y_1$  is the wall distance and  $C_\mu$  is a constant of value 0.09. This equation is consistent with the Fluent (2001) definition of  $y^*$ . Fluent (2001) goes on to state “in FLUENT, the laws-of-the-wall for mean velocity and temperature are based on the wall unit,  $y^*$ , rather than  $y^+$ . These quantities are approximately equal in equilibrium turbulent boundary layers.” OpenFOAM appears to be consistent with that approach. For reference, the standard definition of  $y^+$  is as follows (Wilcox, 1994):

$$y^+ = \frac{u_\tau y}{\nu} \quad (3.36)$$

and  $u_\tau$  is the friction velocity defined as:

$$u_\tau = \sqrt{\frac{\tau_w}{\rho}} \quad (3.37)$$

Note that the mesh around the airfoil was altered to impose a sharp trailing edge, which required scaling of the NACA equation, given by Leishman (2006)

$$\frac{y_t}{c} = \bar{y}_t = 5 \bar{t} \left( 0.29690 \sqrt{\bar{x}} - 0.12600 \bar{x} - 0.35160 \bar{x}^2 + 0.28430 \bar{x}^3 - 0.10150 \bar{x}^4 \right) \quad (3.38)$$

Where  $t$  is the chord thickness, and the overbar on  $y_t$ ,  $x$  and  $t$  indicates values normalized by chord length. For a NACA 0012 airfoil,  $t/c = 0.12$ . The scaling factor of 1.008930411365 was applied to each term at the power as  $x/c - 1$ .

The final mesh for each case features a  $y^+$ , total number of cells, and number of cells around the airfoil were selected as shown in Table 3.10. The cells in the mesh are shown at various levels of zoom in Figure 3.6, Figure 3.7 and Figure 3.8.

### 3.5.5 Parallel Processing

To accelerate the computations and take advantage of multi-core processing, parallel

**Table 3.10:** Mesh data.

Parameter	Case	
	Case 1: Reference Case (McAlister <i>et al.</i> , 1982, Frame 14210)	Case 2: Variable Freestream Case (Helicopter Representative)
$y^+$	0.1 – 48	0.1 – 60
Number of Cells	42240	38400
Number of Cells Along Airfoil	240	240

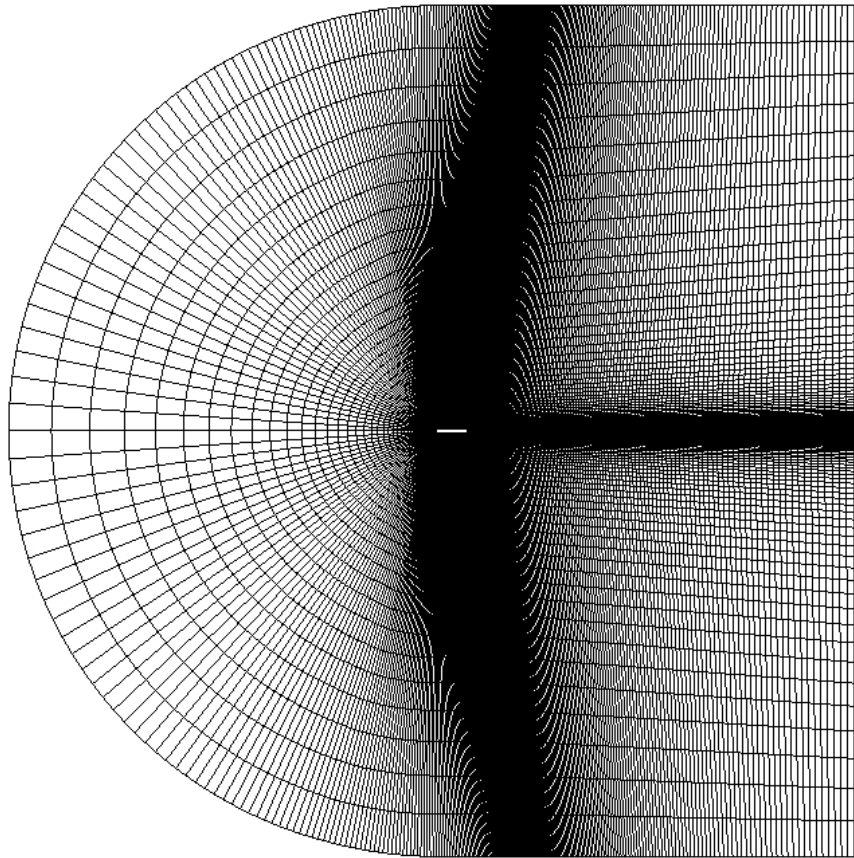


**Figure 3.6:** Computational mesh.

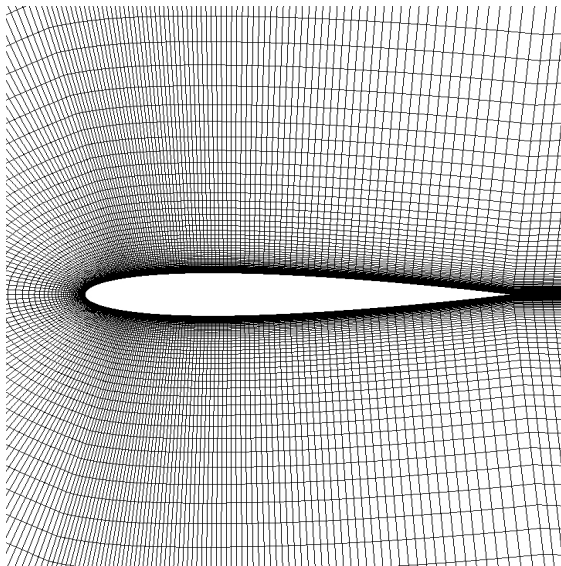


**Figure 3.7:** Computational mesh: zoom on airfoil.

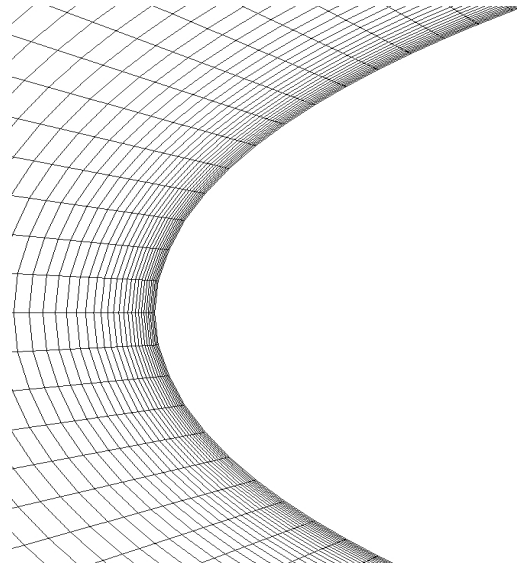


**Figure 3.8:** Computational mesh: zoom on leading edge boundary layer resolution.

processing was used on the computational domain. The domain was distributed into four sub-domains, two along the  $x$ -axis and two along the  $y$ -axis, and decomposed using the methodology of Scotch version 6.0.0 (Pellegrini, 2012). The decomposed mesh is shown in Figure 3.9.

### 3.5.6 Temporal Discretization

The solution is determined at discrete points in space but also, for transient (or

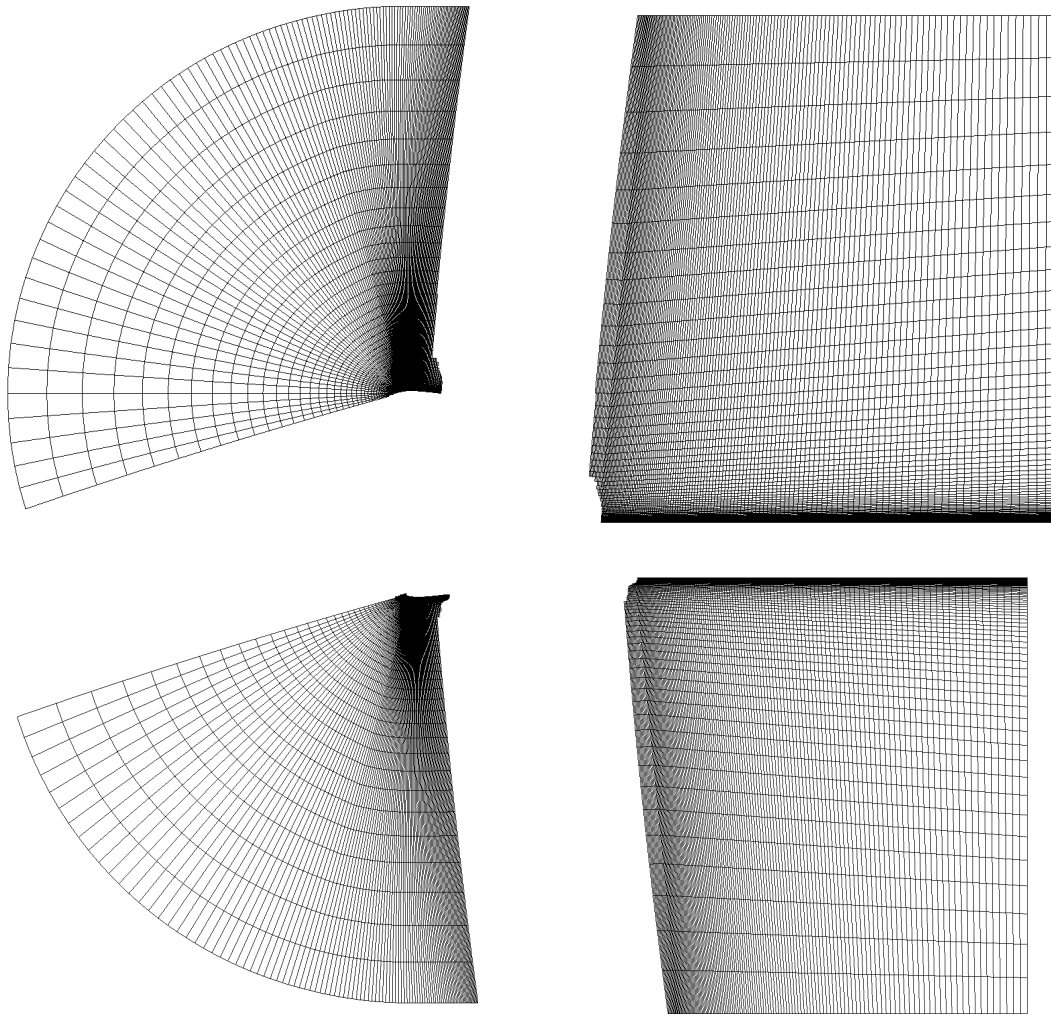


**Figure 3.9:** Decomposition of domain into four sub-domains for parallel processing using Scotch.

unsteady) solutions such as these, at discrete points in time. The method of linearizing and discretizing the temporal terms was described in Section 3.4.1; this section will describe the selection of the timestep size.

The selection of the timestep size is essential for temporal accuracy and numerical stability, and depends somewhat on the spatial discretization. The requirement for timestep size based on spatial discretization is based on the ratio between node spacing  $\delta x$  to timestep  $\delta t$ , given by the OpenFOAM User Guide (2014)

$$Co = \frac{|U| \delta t}{\delta x} \quad (3.39)$$

Although implicit discretization schemes are in theory more stable and can make use of higher Courant numbers ( $Co$ ) than their explicit counterparts, which have a theoretical upper limit of 1, it was found with OpenFOAM that cases would not converge with a  $Co$  much greater than 0.3. The timestep was controlled by using the “adjustableTimeStep” option of the “rhoCentralFoam” solver, which allows the user to specify a maximum  $Co$  and the software will adjust the timestep to match. This option, and the low  $Co$  limit practically required for convergence, required a timestep of  $9 \times 10^{-8}$  s which yielded average and maximum  $Co$  of 0.0055 and 0.5, respectively. For the constant freestream speed case, these were  $5.6 \times 10^{-8}$  s, 0.003 and 0.3. The Courant number maximum ensures that any phenomenon moving across the grid will be measured at neighbouring nodes on successive timesteps, and not skip any neighbouring cells.

It is also essential to ensure that any transient phenomena are adequately resolved

with a sufficient number of timesteps. Leishman (2006) stated that the time step must be selected such that no more than  $2-5^\circ$  of azimuth change takes place between timesteps to accurately represent dynamic stall. In this case, with a rotational frequency of over 1800 degrees/second, there is far less than one degree of azimuth per time step and this criteria is easily met, the Courant number criterion being more severe for this case.

### **3.5.7 Solution Convergence**

Convergence of each timestep is determined when the criteria for residual error for each parameter defined in Table 3.5 are met. Convergence of the case as a whole is determined by obtaining periodicity of the last two cycles of azimuth for the aerodynamic loads.

## **3.6 Solution Fidelity**

This section describes the validation and verification that was done to ensure that the simulation results were credible, and followed the guidelines of AIAA (1998). The purpose of verification is to determine if the implementation of the simulation accurately represents the conceptual model of the problem. Validation is performed to determine if the computational simulation is representative of the actual flow physics of the real-world problem to be solved. The verification and validation presented in this section includes only the scope of trade studies or selection of parameters that were carried out before the results of the cases were obtained. The second part of the verification and validation, which requires the results of the cases, is presented in the next chapter.

### **3.6.1 Verification**

Verification determines if the problem has been solved correctly. Verification addresses the primary sources of error in CFD simulations: mesh and time-step independence, and iterative convergence. Mesh and time-step convergence studies are discussed in this section, while iterative convergence is discussed in the next chapter with the presentation of the results.

#### **3.6.1.1 Mesh Independence**

Mesh independence is shown when there is little change in the results observed by refining the grid or timestep. Second-order accurate discretization schemes are generally accepted as sufficient, and second-order schemes were selected as described above. Figure 3.10 shows the comparison between the coefficient of pressure on the airfoil from CFD and experimental data. It is clear that the CFD results are nearly coincident with each other and match well with experimental data, indicating that the results are not dependent on the mesh.

#### **3.6.1.2 Time-Step Independence**

Time-step independence is shown when there is little change in the results observed by refining the timestep. Second-order accurate discretization schemes are generally accepted as sufficient, and a second-order accurate discretization scheme in time was used as described above. The simulation for Case 1 was run to four cycles at maximum Courant numbers of 0.3 and 0.5 to confirm that the reduction in timestep did not significantly change the results. As shown in Figure 3.11, the lift, pitching moment and

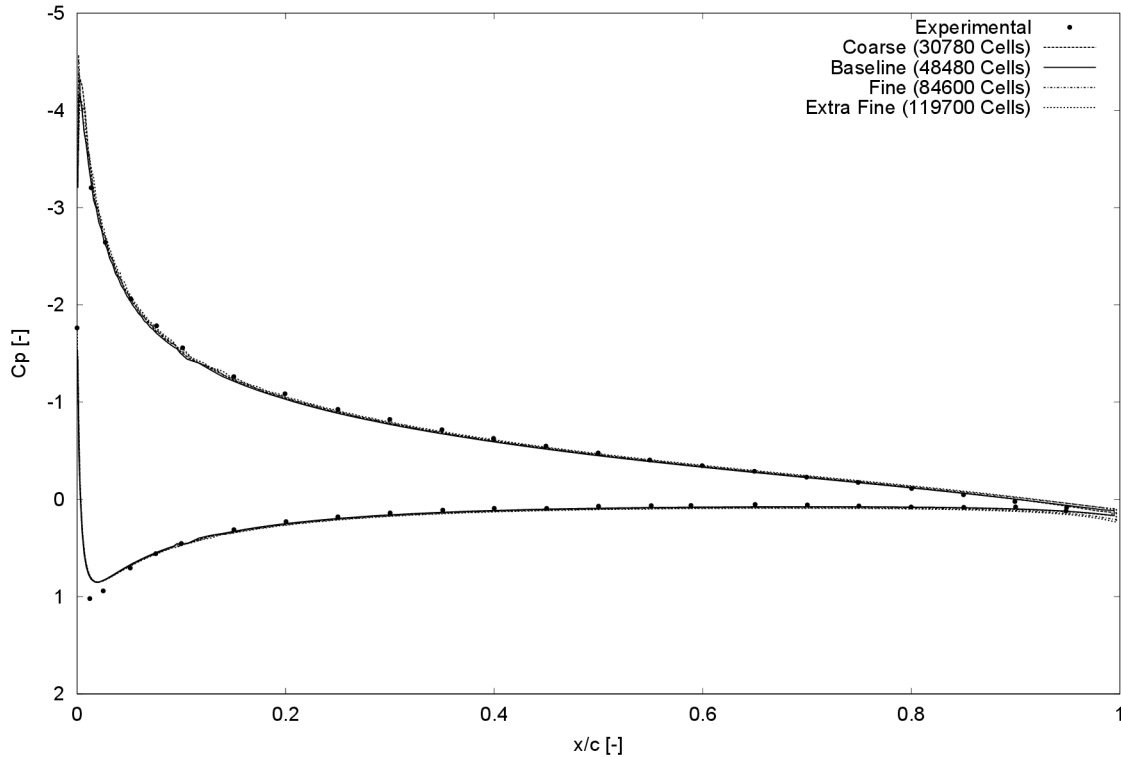


**Figure 3.10:** Mesh independence results, NACA0012 airfoil at Mach 0.30, Reynolds Number  $6.1 \times 10^6$ ,  $k = 0$  and angle of attack  $9.0^\circ$ . Experimental data from Ladson *et al.* (1987).

drag data were consistent at both Courant numbers, indicating the results were not dependent on the selection of the time-step.

### 3.6.2 Validation

Validation seeks to ensure that the correct problem has been solved, and accuracy is measured against experimental results. A building-block approach is recommended, and applied to this case as follows: steady solutions, unsteady pitch solutions, and dynamic stall oscillating pitch solutions. These results were then extended to the variable freestream magnitude case, for which no validation case exists at comparable conditions.

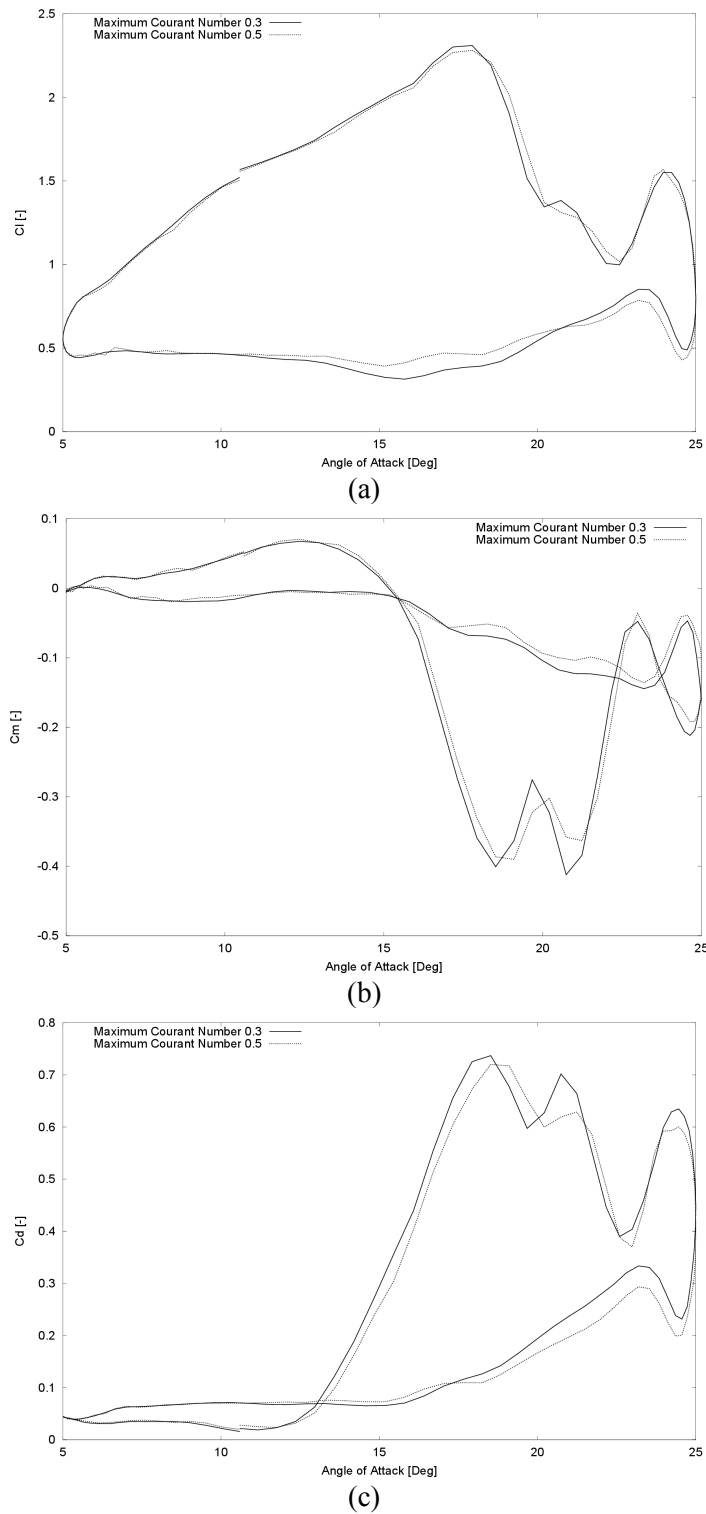


**Figure 3.11:** Timestep independence comparison of (a) lift, (b) pitching moment and (c) drag results, Case 1.

### 3.6.2.1 Steady and Quasi-Steady Solutions

A series of steady freestream static cases was run first to test OpenFOAM with a less demanding case, and good agreement was found with experimental data of Ladson (1988) and Ladson *et al.* (1987) and numerical results for coefficients of pressure, drag, lift, and pitching moment in Figure 3.12 and Figure 3.13. A steady solver was used to generate the  $C_p$  data, and an incompressible transient solver was used to generate the  $C_d$ ,  $C_l$  and  $C_m$  data, as simulations of increasing complexity were completed to gain confidence in OpenFOAM's capabilities.

### 3.6.2.2 Dynamic Stall Oscillating Pitch Solution

The results of Case 1 will be compared to experimental data in the Results chapter below.

## 3.7 Post-Processing and Data Reduction

This section describes the post-processing that was carried out, and the relevant

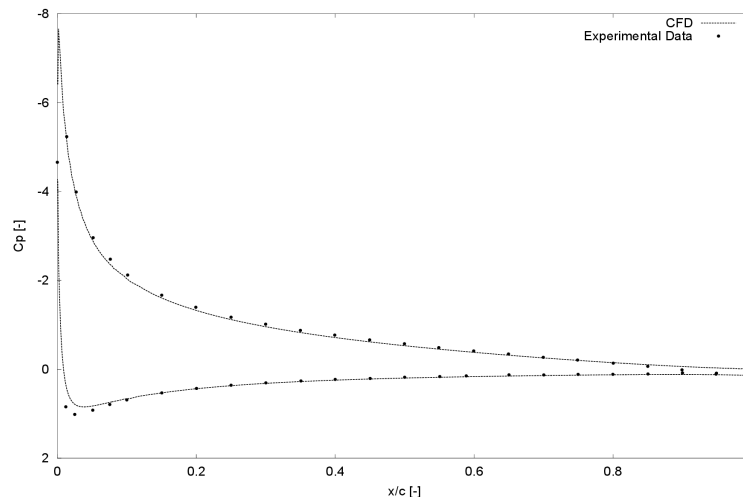


**Figure 3.12:**  $C_p$  vs  $x/c$ , NACA0012 airfoil at Mach 0.30, Reynolds Number  $6.1 \times 10^6$ , and angle of attack  $13.0^\circ$ . Experimental data from Ladson *et al.* (1987).

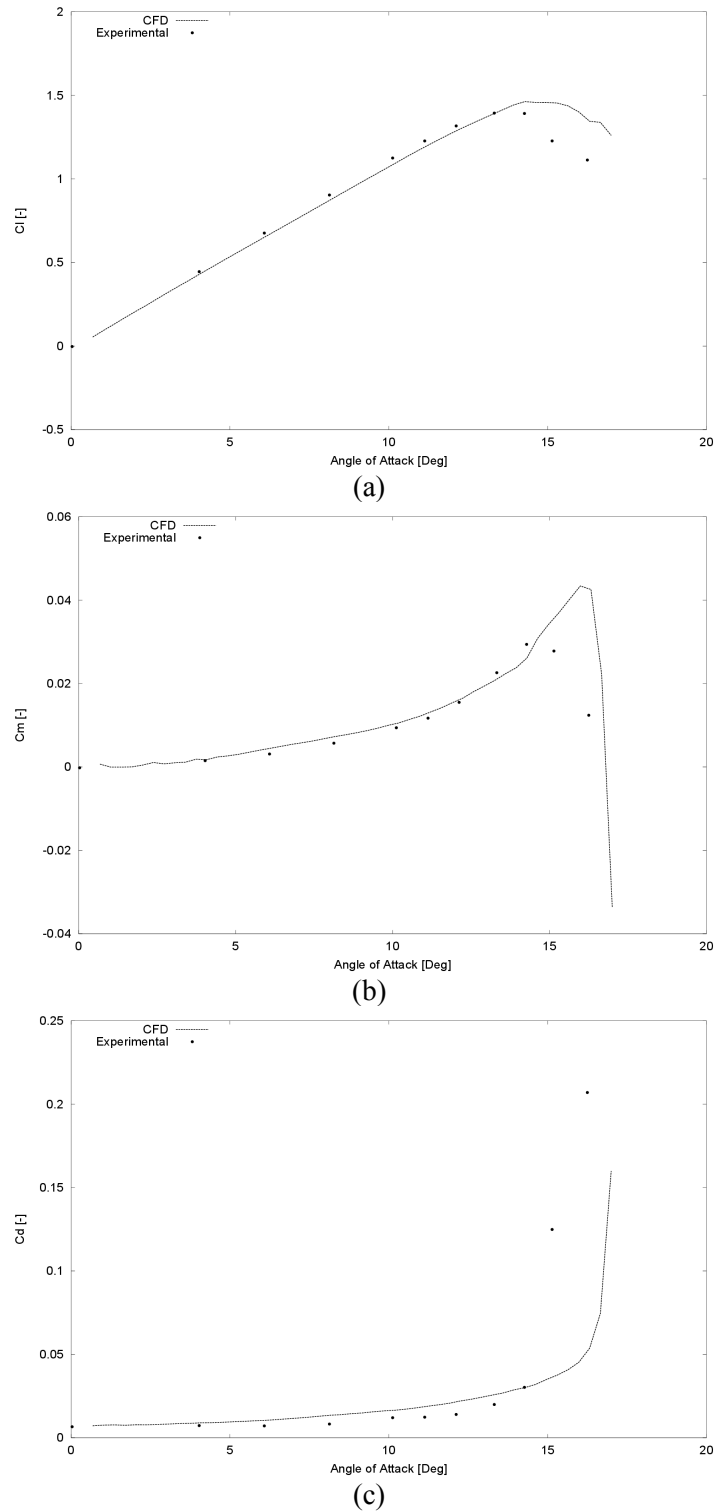


**Figure 3.13:** Coefficient of (a) lift, (b) pitching moment and (c) drag versus angle of attack for static angle of attack, NACA 0012 airfoil, Mach 0.3, Reynolds number  $5.93 \times 10^6$ . Experimental data from Ladson (1988).

equations used to calculate the applicable parameters.

### **3.7.1 Flow Visualization**

ParaView software version 4.1 (Henderson, 2007) was used for post-processing. This open-source software package is compatible with OpenFOAM, and was used to generate images and animations of the results, by plotting streamlines, vectors, contours and surface scalar data. Macros and shell scripts were written to automate the post-processing to the extent possible.

### **3.7.2 Data Reduction**

A combination of OpenFOAM's standard post-processing tools and custom scripts are used to post-process the case data. First, OpenFOAM's native tools were used to calculate wall shear stress,  $y^+$ , Mach number, and vorticity. Second, GNU Octave 3.6.2, a high-level open-source programming language similar to Mathworks MATLAB, was used to process the data from the simulations via shell scripts run from a Linux operating system. The post-processing script read the required data from the case structure. Then, the aerodynamic loads and azimuth position of the airfoil were calculated based on the freestream conditions at the airfoil.

#### **3.7.2.1 Application of Time Lag**

The inlet speed and direction are defined at the inlet boundary, and there is a  $10c$  distance between the airfoil and the inlet, therefore a change in velocity at the inlet will only affect the airflow at the airfoil once it has convected downstream to the airfoil.

Poinsot and Lele (1992) defined the characteristic speed of a wave travelling in the positive direction (in the direction of the airflow) as  $\lambda_5 = U + a$ ; essentially, the linear combination of the speed of the pressure wave (the speed of sound in the medium) and the speed of the medium itself. This lag was applied in post-processing to determine the conditions at the airfoil. The time lag defined above was validated experimentally by Gompertz *et al.* (2011) and Jensen *et al.* (2011), though for wave propagation upstream, who modified a wind tunnel to generate a variable freestream magnitude.

The time lag was calculated differently for the constant freestream and variable freestream magnitude cases. For constant freestream magnitudes, the time lag was calculated using the formula

$$\Delta t_{lag} = \frac{10c}{a + U_{inlet(t)}} \quad (3.40)$$

where  $U_{inlet(t)}$  is the inlet airspeed at time  $t$ .

However, for variable freestream magnitudes, an additional step was required. Given the dependence of the time lag on the inlet speed, the time lag was calculated as above for each time step. The time lag was then added to the timestep for which it was calculated to obtain the “arrival time” of the freestream at the airfoil. A one-dimensional cubic interpolation was then carried out to determine the lag at each timestep on the airfoil considering the “arrival time”.

The azimuth position of the airfoil was then determined from the time lag and the values of these parameters at the inlet as follows:

$$\psi_{airfoil}(t) = \text{mod}(\Omega \cdot \max((t - \Delta t_{lag}(t)), 0), 360^\circ) \quad (3.41)$$

The azimuth position is then substituted into Equations (2.7) and (3.1) to yield lag-adjusted equations for airspeed and angle of attack:

$$\frac{U_{airfoil}(t)}{U_{rot}} = 1 + \lambda \sin \psi_{airfoil} \quad (3.42)$$

$$\alpha_{airfoil}(t) = \alpha_0 + \alpha_1 \sin(\psi_{airfoil} + 180^\circ) \quad (3.43)$$

### 3.7.2.2 Aerodynamic Loads Calculation

Coefficients of pressure and skin friction were obtained from which aerodynamic loads (lift, drag, pitching moment) could be calculated. Pressure forces are converted to  $C_p$  according to the following formula for compressible flow (Leishman, 2006):

$$C_p = \frac{2}{\gamma M_{(t)}^2} \left( \frac{P}{P_\infty} - 1 \right) \quad (3.44)$$

Wall shear stress is read from the OpenFOAM post processing file and converted to coefficient of friction as follows (Schlichting, 1979):

$$\tau_w = 0.5 C_f \rho U_{airfoil}^2 \quad (3.45)$$

where (Schlichting, 1979):

$$\tau_w = \mu_{eff} \left. \frac{\partial U}{\partial y} \right|_{y=0} \quad (3.46)$$

and

$$\mu_{eff} = \mu + \mu_t \quad (3.47)$$

for simulations with turbulence modelling.

The direction of application of the pressure force,  $\hat{P}$ , is taken as the direction perpendicular to the airfoil surface at the node, as determined by the negative inverse of the derivative of the airfoil equation at that point. The direction of application of the shear force is taken as the direction tangent to the airfoil surface, as determined by the derivative of the airfoil equation at that point.

### 3.7.2.3 Lift

The area to which the pressure and shear forces was applied was calculated as the vertical or horizontal distance between the midpoints of a given cell and its neighbouring points, for drag and lift respectively. In this context, vertical and horizontal mean with respect to the airfoil chord; corrections for angle of attack are taken into consideration with the rotation matrix,  $rot$ , since the domain does not move with changes in angle of attack. The lift vector,  $lift$ , is used in matrix multiplication to obtain the component of the aerodynamic force in the direction perpendicular to the relative airflow.

$$rot = \begin{bmatrix} \cos(\alpha) & -\sin(\alpha) \\ \sin(\alpha) & \cos(\alpha) \end{bmatrix} \quad (3.48)$$

$$lift = [0 \quad 1] \quad (3.49)$$

The standard sectional lift equation

$$C_l = \frac{L}{\frac{1}{2} \rho U^2 c} \quad (3.50)$$

where  $L$  is the sectional lift force, with some manipulation can yield

$$C_l = \frac{1}{c} \sum_{n=1}^{\# \text{Nodes on airfoil}} d_{eff(n)} \left( C_{p(n)} \times \hat{P} \times rot \times lift - [C_{fx} \ C_{fy}] \times rot \times lift \right) \quad (3.51)$$

where  $d_{eff}$  is the distance on the airfoil surface upon which the force at a node acts.

### 3.7.2.4 Drag

As for lift, similarly for drag, though the lift vector is replaced by the drag vector defined below, for aerodynamic forces parallel to the relative airflow:

$$drag = [1 \ 0] \quad (3.52)$$

The standard sectional drag equation

$$C_d = \frac{D}{\frac{1}{2} \rho U^2 c} \quad (3.53)$$

where  $D$  is the sectional drag force, can be manipulated to yield

$$C_d = \frac{1}{c} \sum_{n=1}^{\# \text{Nodes on airfoil}} d_{eff(n)} \left( C_{p(n)} \times \hat{P} \times rot \times drag - [C_{fx} \ C_{fy}] \times rot \times drag \right) \quad (3.54)$$

### 3.7.2.5 Pitching Moment

The moment arm for each cell was calculated as the vertical or horizontal projected distance between the node and the quarter-chord point, for drag and lift, respectively.

Then the standard sectional pitching moment equation

$$C_m = \frac{M}{\frac{1}{2} \rho U^2 c^2} \quad (3.55)$$

where  $M$  is the sectional pitching moment, can be manipulated to yield

$$C_m = \frac{1}{c} \sum_{n=1}^{\# \text{Nodes on airfoil}} C_{d(n)} \times d_{drag(n)} + C_{l(n)} \times d_{lift(n)} \quad (3.56)$$

where  $d_{drag}$  and  $d_{lift}$  are the vertical and horizontal projections of  $d_{eff}$  in airfoil coordinates, and represent the distance on the airfoil surface upon which the each force acts at a mesh node.

## **Chapter 4**

### **Results**

This chapter is structured into two sections. First, the steady freestream case will be evaluated to demonstrate that the computation is validated and verified, and thus appropriate for use on the variable freestream case. Second, the variable freestream case will be discussed and the differences between the two cases will be described.

#### **4.1 Steady Freestream Case**

This section addresses the elements of verification and validation of the model that were not described in the previous chapter because they required the results from the simulation; namely, boundary conditions, solution convergence, aerodynamic loads and the mechanism of dynamic stall.

### 4.1.1 Boundary Conditions

The correct implementation of the boundary conditions was confirmed by plotting the velocity vectors over the complete domain as vector plots and comparing to the expectation at the inlet, an example of which is shown in Figure 4.1. This image shows the vectors aligned horizontally left-to-right, as they should when the domain is rotated to the desired angle of attack. Review of vorticity and pressure contours throughout the

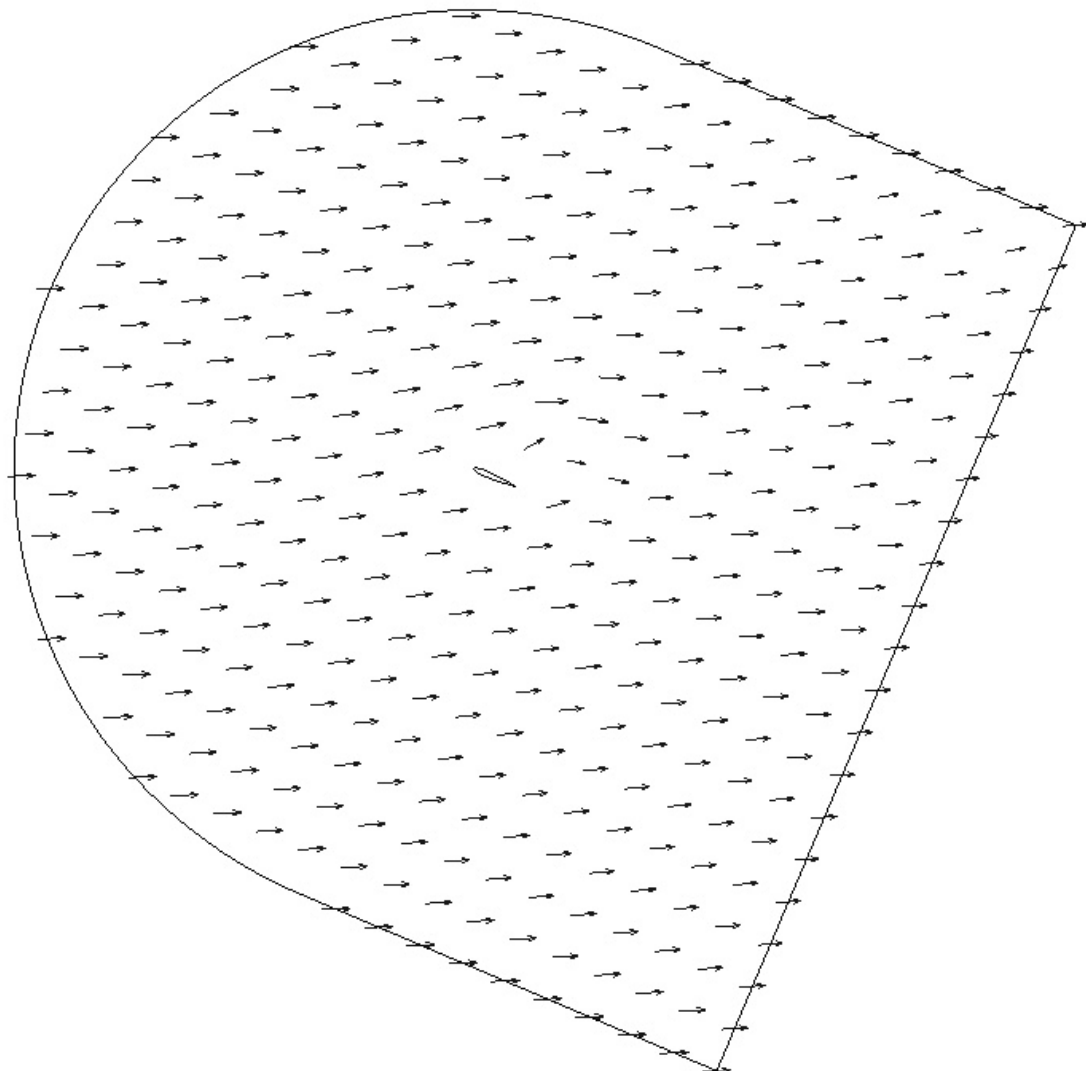


**Figure 4.1:** Vector plot showing boundary conditions at high angle of attack, 233° azimuth.

motion showed no evidence of reflection at the boundaries, consistent with the selection of a non-reflective boundary condition at the outlet.

### 4.1.2 Convergence

Convergence was evaluated in two ways: reduction of the residual between iterations and periodicity of the aerodynamic loads. OpenFOAM interrupts simulations when a maximum number of iterations is reached without the residual descending beyond the target defined by the user, as described in the preceding chapter. The simulation was completed without interruptions, indicating that the residual targets were achieved. Convergence was also evident in comparing the periodicity of the results, as shown in Figure 4.2, where periodicity is obtained after the fifth cycle.

### 4.1.3 Aerodynamic Loads

Plots of coefficients of lift, pitching moment and drag versus angle of attack for the last cycle of rotation are shown in Figure 4.3. The CFD results show acceptable agreement with the experimental data, and the same quantitative characteristics are present in both. The overall shapes of the CFD results are consistent with the experimental data, and the peaks in  $C_m$ ,  $C_d$ , and  $C_l$  match closely. Lift and moment stall angles of occurrence also match well, as shown in Table 4.1. The CFD data for the upstroke matches the experimental results quite well, which was expected due to the turbulence modelling of significant flow separation, as has been discussed in the literature review. For the pitching moment, note that the CFD data show four loops in the

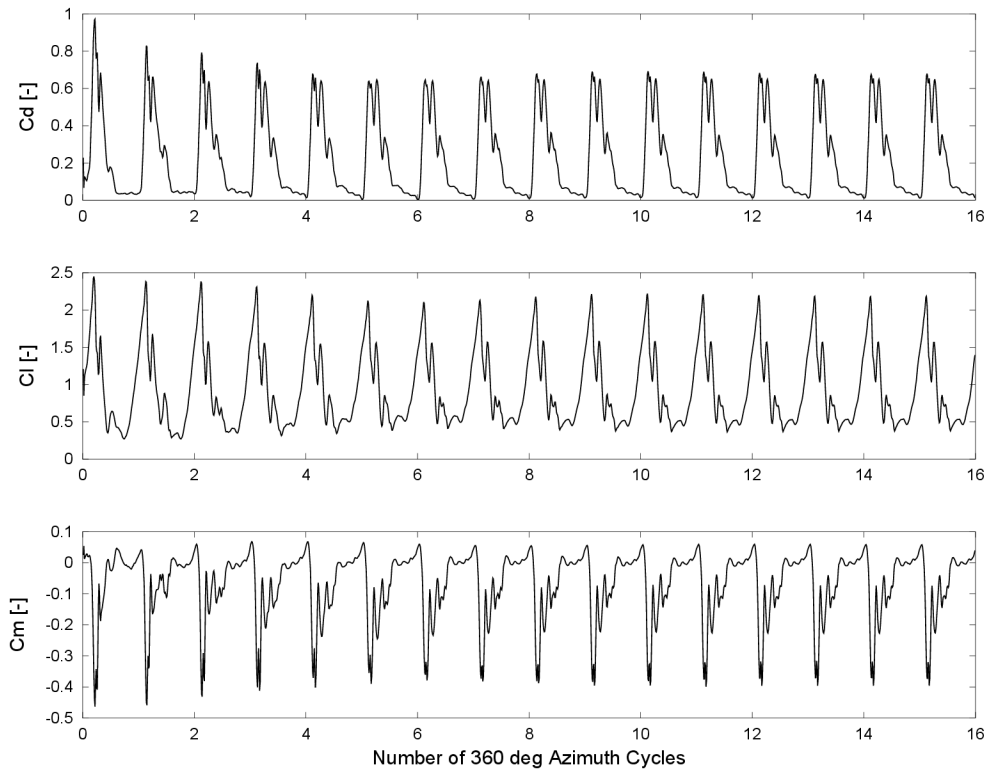


**Figure 4.2:** Time-history of aerodynamic loads, steady freestream case (Case 1). Each cycle begins at  $154^\circ$  azimuth at the airfoil.

$C_m$ - $\alpha$  curve, whereas only three were expected from the literature review, to be consistent with deep stall. The experimental data did not show any loops; although the  $C_m$  data from the up- and down-strokes were very close at  $18^\circ$  and  $24^\circ$  angle of attack, they did not cross each other to form a loop. This difference is acknowledged but will not be discussed further since controlling aerodynamic damping is not the purpose of this thesis.

The results were also consistent with the typical features of a dynamic stall case as suggested by the literature review: there was an increase in lift with respect to the static loading case, the pitching moment stall precedes the lift stall and the lift stall is at a higher angle of attack than the quasi-static airfoil stall angle of attack. No change in lift-

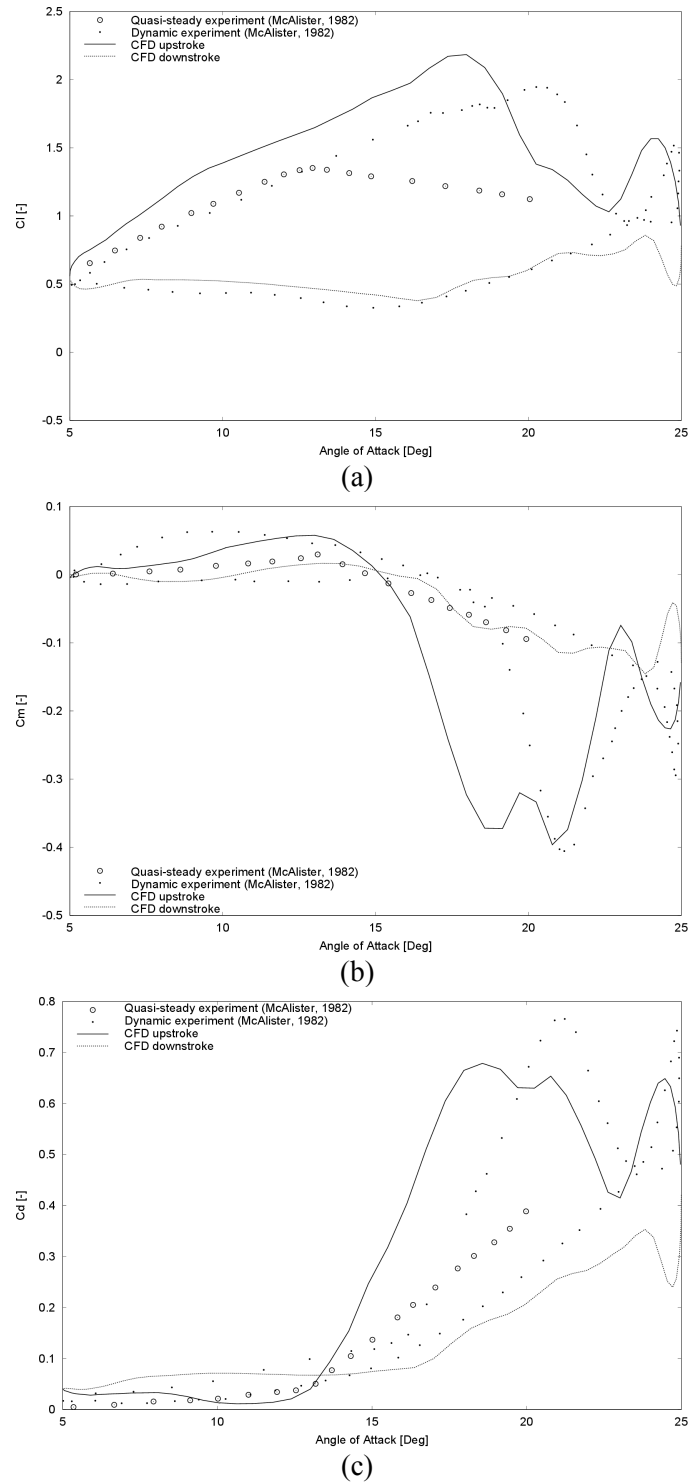


**Figure 4.3:** Comparison of (a) lift, (b) pitching moment and (c) drag coefficients from quasi-steady and dynamic experimental results from McAlister *et al.* (1982) as well as of CFD results of this work. The flow conditions correspond to  $M = 0.301$ ,  $Re = 3.91 \times 10^6$  and  $\alpha = 15^\circ \pm 10^\circ$ . Quasi-static results are shown for a slow ramp-up in angle of attack between 5 and 20 degrees.

**Table 4.1:** Comparison of CFD results to experimental data, both for the steady freestream case. Arrows next to the angles of attack indicate upstroke or downstroke.

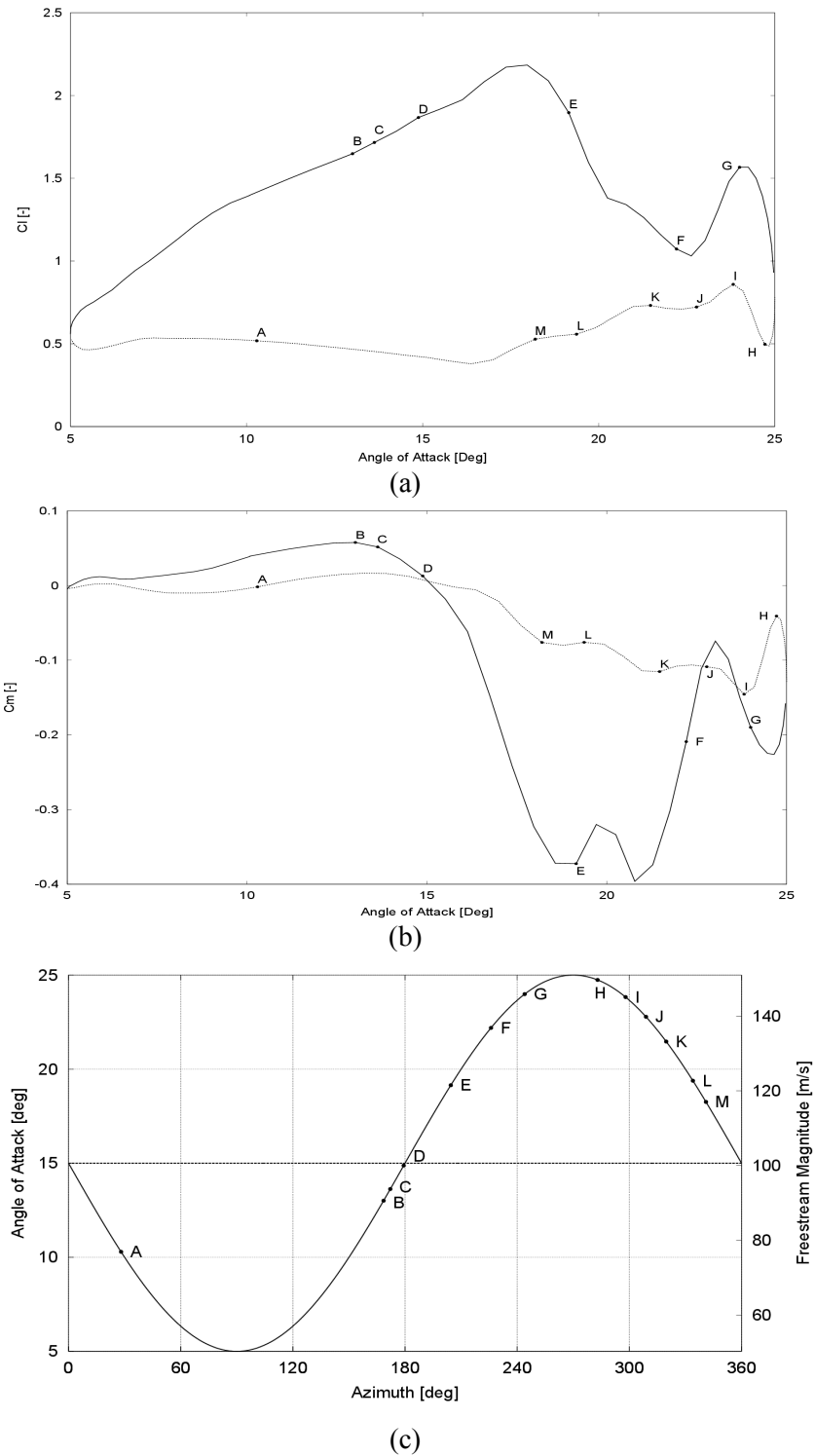
Parameter [units]	CFD	Experimental	Difference
Negative Peak $C_m$ [-]	-0.396	-0.405	-2.3%
Peak $C_d$ [-]	0.679	0.766	-11.4%
Peak $C_l$ [-]	2.184	1.946	+12.2%
Moment stall $\alpha$ [°]	14.9 ↑	16.5 ↑	CFD Earlier
Lift stall $\alpha$ [°]	18.0 ↑	20.3 ↑	CFD Earlier

curve slope was observed with respect to the quasi-static airfoil data.

#### 4.1.4 Mechanism of Dynamic Stall at Steady Freestream

This section of the thesis discusses the mechanism of dynamic stall by analyzing a sequence of two sets of images selected at points on the azimuth corresponding to lift and pitching moment data as shown in Figure 4.4. Images showing pressure contours and velocity vectors in the first column and Mach number contours and streamlines in the second column together form Figure 4.5, and each set of images correspond to a point in the azimuth of rotation indicated by a letter, as shown in Figure 4.4. The discussion that follows makes reference to sub-images of Figure 4.5 by indicating the sub-image reference letter in parentheses.

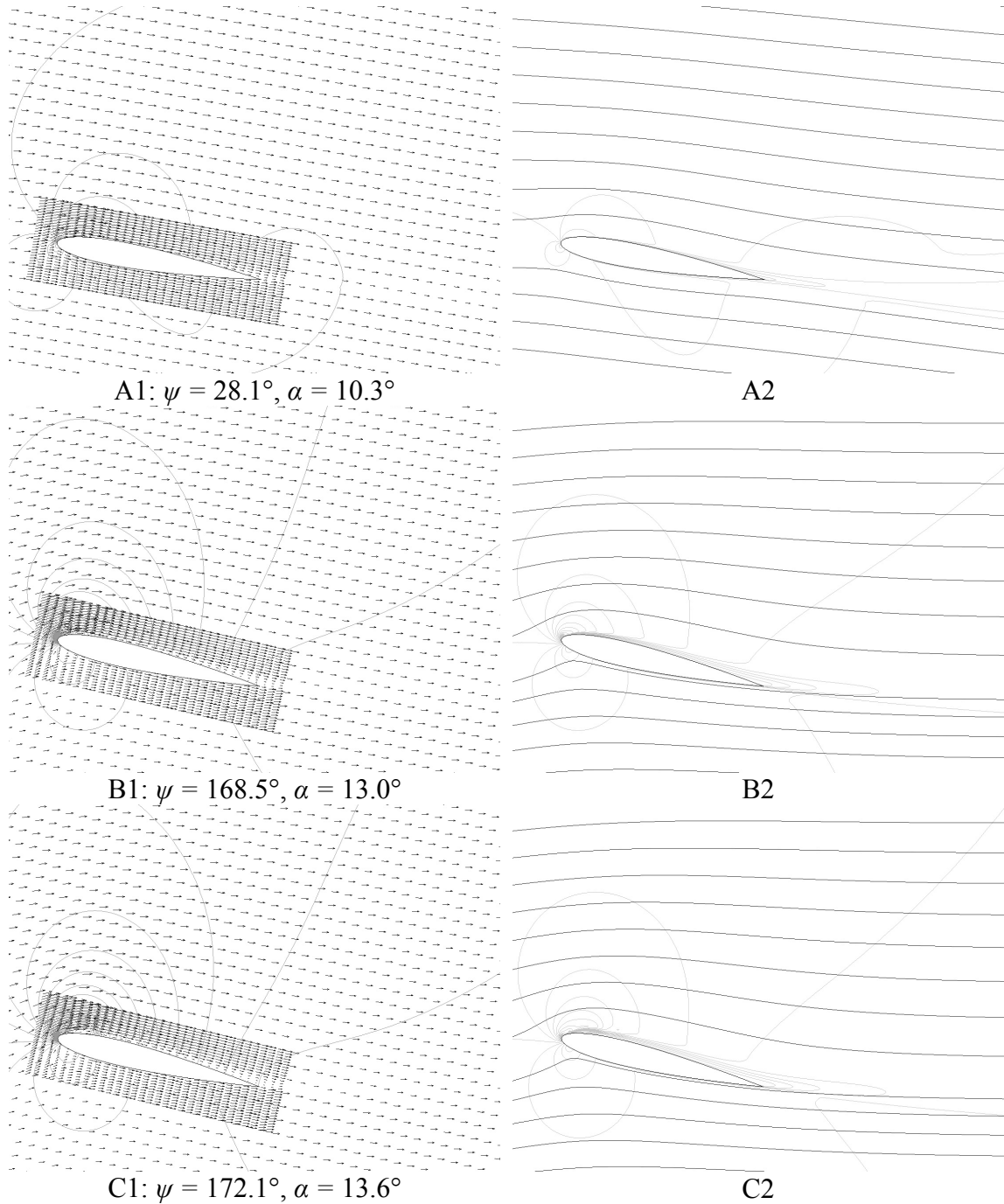
Flow separation begins at the trailing edge (frame B), and later at the leading edge (frame C) with attached flow in between. A laminar separation bubble (LSB) forms briefly at  $\alpha = 13^\circ$ , and then grows into a leading-edge vortex (LEV) (frame D) and is convected aft over the airfoil at about a quarter of the freestream speed (frame E), which

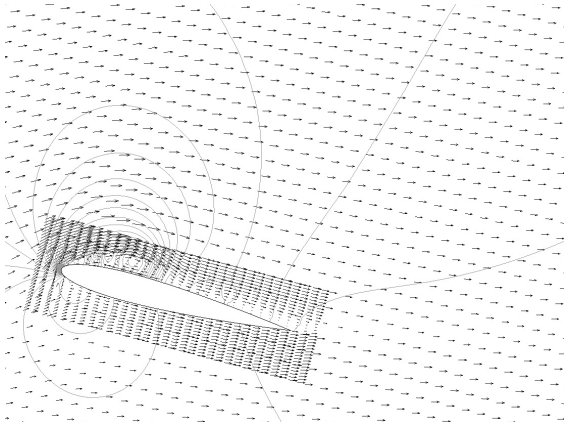
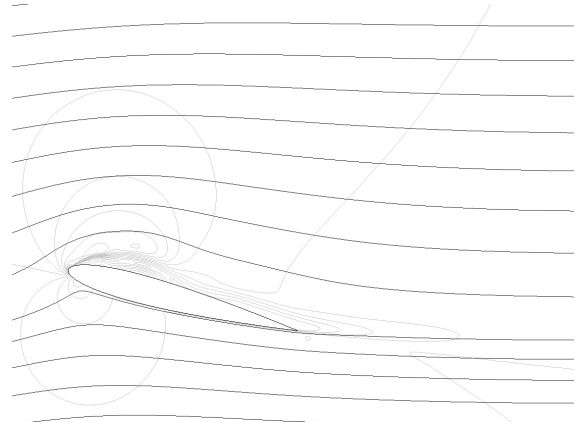


**Figure 4.4:** Positions of images in Figure 4.5 indicated on coefficient of (a) lift and (b) pitching moment coefficient CFD results for Case 1. Solid line indicates upstroke, dashed line indicates downstroke. (c) Azimuthal positions of images in Figure 4.5. Dashed line is speed, solid line is angle of attack.

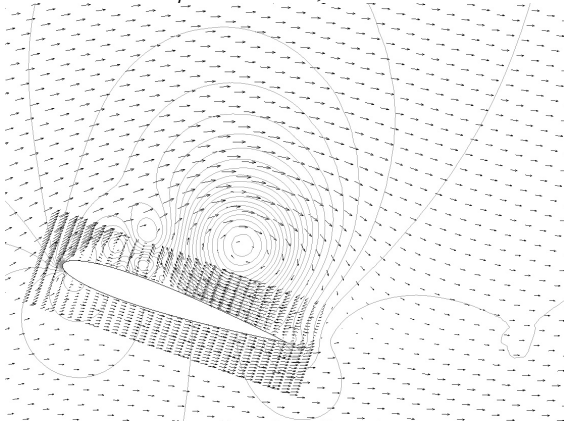
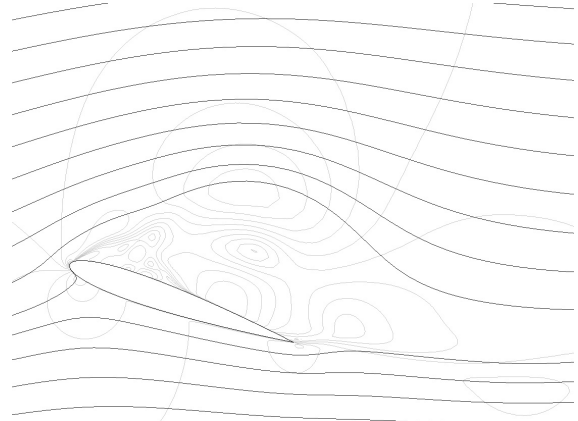
is consistent with previous literature (Gerontakos, 2008). As it reaches  $\alpha = 19^\circ$ , the trailing edge vortex (TEV) begins to form (frame E). The presence of three loops in the  $C_m$ - $\alpha$  data and the shedding of the LEV and lift stall prior to the maximum angle of attack suggest the airfoil is in the deep dynamic stall regime. The downstream motion of the LEV is suspended from  $\alpha = 20^\circ - 21^\circ$ , where it instead remains stationary relative to the chord and moves upward (frame F), where it then continues downstream over the TEV away from the airfoil as the TEV grows. A second large LEV is shed at that instant, which grows and convects aft as a second TEV develops (frame F). The shedding and convection of the second LEV appears to be responsible for the second increase in lift at high angle of attack. The second LEV pauses its downstream motion near  $0.8c$  much like the first LEV (frames G, H), though instead of moving over the TEV as the first LEV did, the second LEV appears to push the second TEV off the trailing edge of the airfoil as the airfoil reaches its maximum angle of attack (frame I). No thin layer of flow reversal in the boundary layer was observed at any point during the cycle. Stall appears to be caused by rapid turbulent boundary layer separation which is consistent with the theory. No shear layer vortex was observed, consistent with the theory (Visbal, 1989) which states that it is not present at flight Reynolds number. Additional, less powerful vortices form during separated flow: first a TEV (frame J), then another LEV (frame K) followed by a final TEV (frame L). Reattachment begins at  $\alpha = 18^\circ$  (frame M), greater than the static stall angle, and is completed by  $\alpha = 11^\circ$  (frame A), and moves downstream at a rate of  $2.5x$  the freestream speed. Although the reattachment is indicated in the qualitative data, the lift graph would show coincident data on the up- and down-strokes during attached flow,

therefore it was unexpected that according to the lift data reattachment did not occur until the angle of attack reached a minimum.

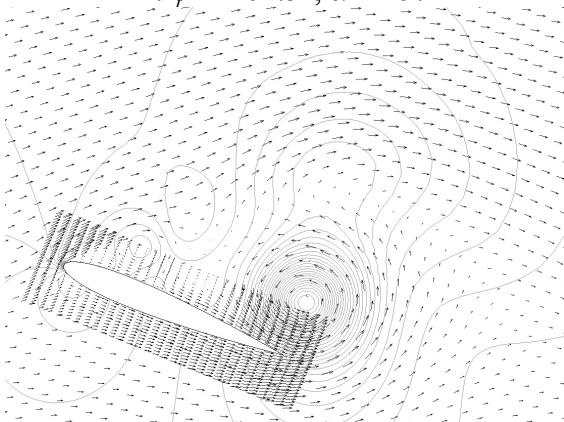
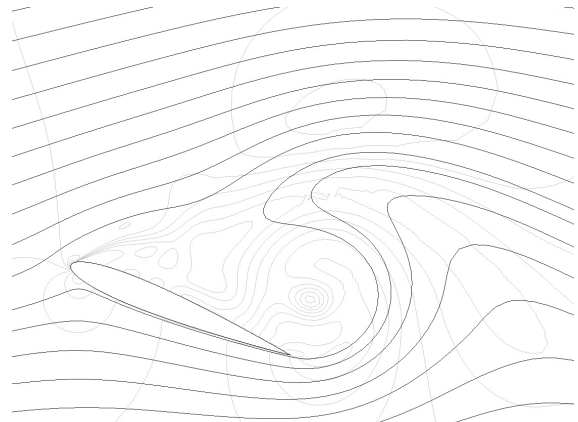


D1:  $\psi = 179.3^\circ$ ,  $\alpha = 14.9^\circ$ 

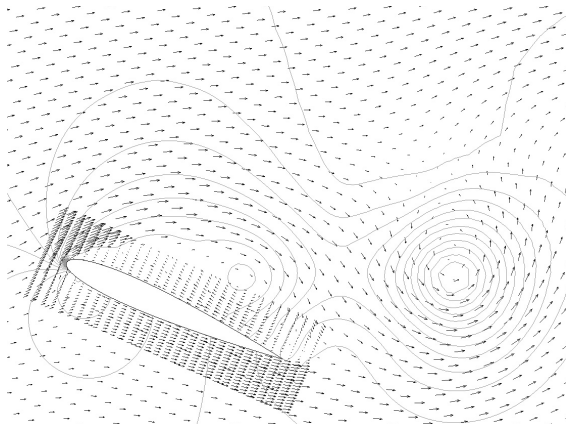
D2

E1:  $\psi = 204.5^\circ$ ,  $\alpha = 19.1^\circ$ 

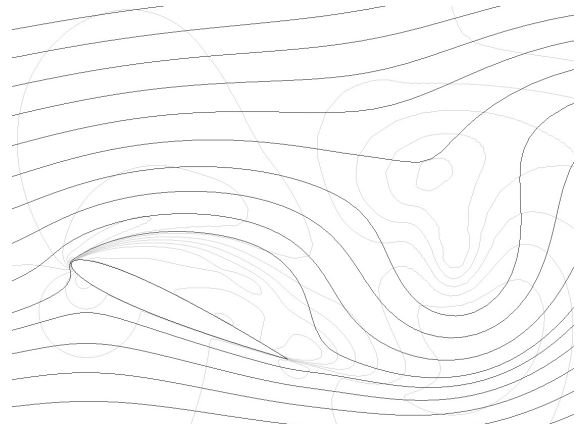
E2

F1:  $\psi = 226.0^\circ$ ,  $\alpha = 22.2^\circ$ 

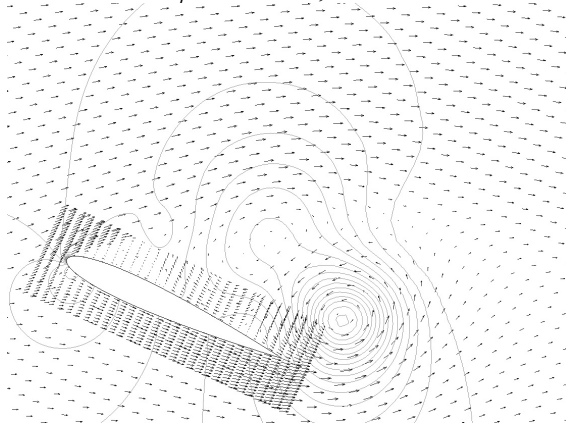
F2



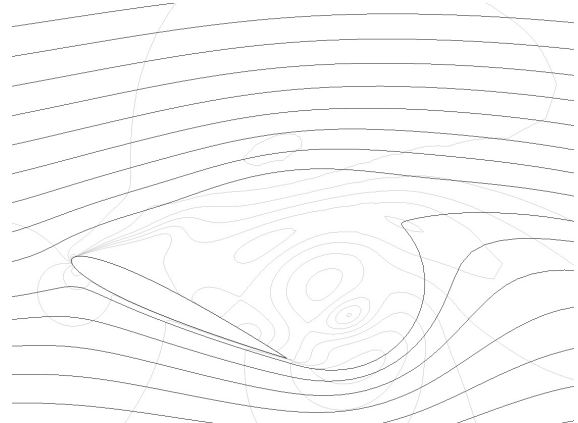
G1:  $\psi = 244.0^\circ$ ,  $\alpha = 24.0^\circ$



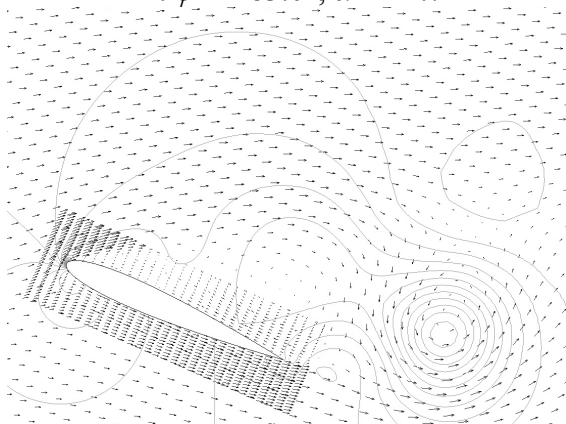
G2



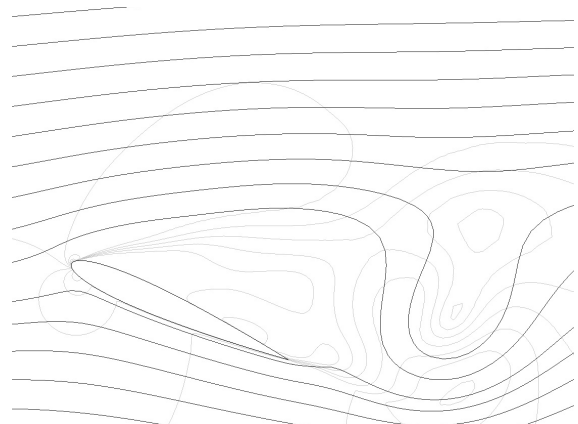
H1:  $\psi = 283.0^\circ$ ,  $\alpha = 24.7^\circ$



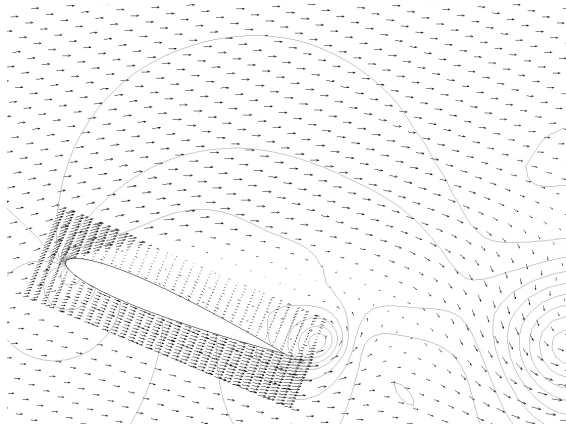
H2



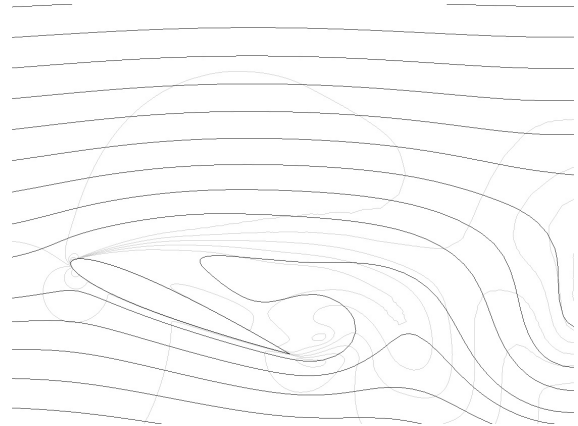
I1:  $\psi = 298.0^\circ$ ,  $\alpha = 23.8^\circ$



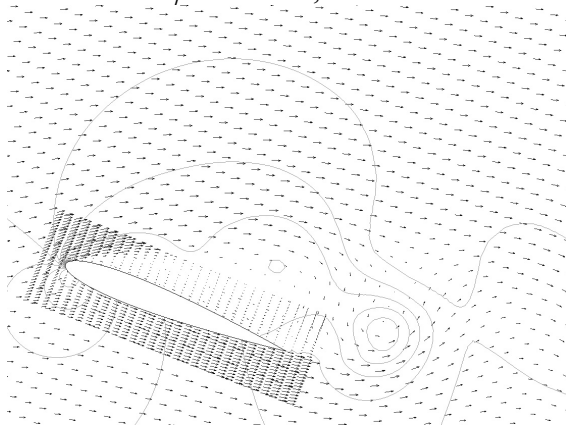
I2



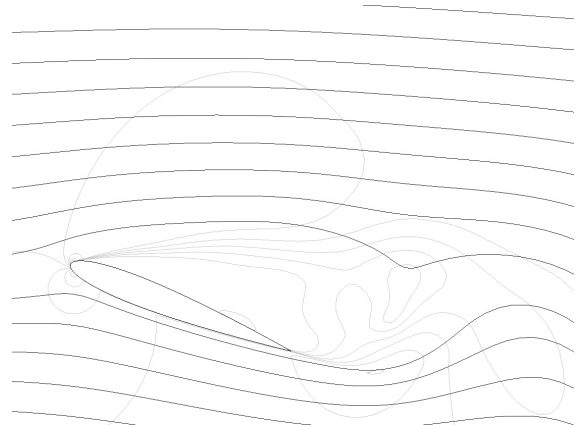
J1:  $\psi = 308.9^\circ, \alpha = 22.8^\circ$



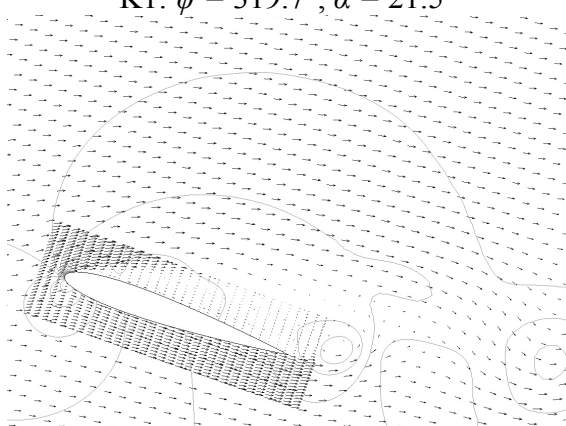
J2



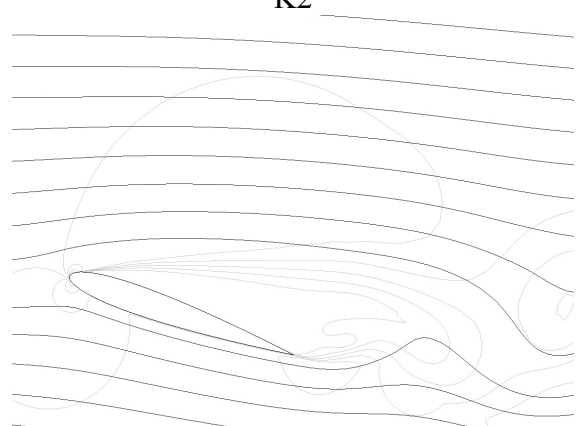
K1:  $\psi = 319.7^\circ, \alpha = 21.5^\circ$



K2



L1:  $\psi = 334.0^\circ, \alpha = 19.4^\circ$



L2

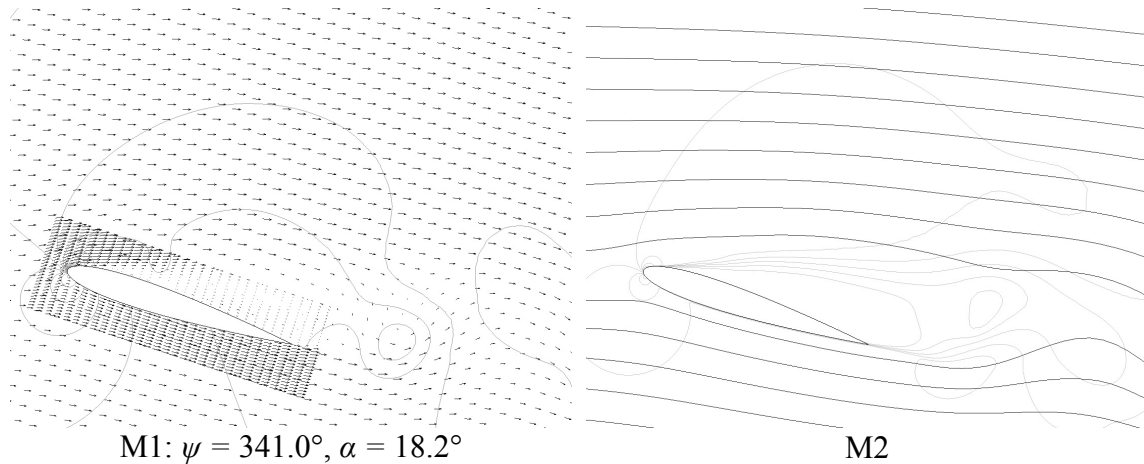


**Figure 4.5:** Velocity vector plots and pressure contours (left column) and Mach contours and streamline plots (right column), rows corresponding to points indicated in Figure 4.4 respectively.

Pressure contours show a minimum of 25 kPa, a maximum of 120 kPa, with 76 contours at intervals of 1.25 kPa. Mach contours show a minimum of M 0, a maximum of M 1.5, with 25 contours at intervals of  $M = 0.06$ . The data is taken from Case 1:  $\alpha = 15^\circ \pm 10^\circ \sin(\Omega t + \pi)$ ,  $k = 0.101$ ,  $M = 0.292$ ,  $Re = 3.76 \times 10^6$ .

## 4.2 Time-Varying Freestream Velocity Case

The model, verified and validated for the steady freestream case, was then considered accurate for extension to an unsteady freestream. This section will provide verification of the boundary conditions and convergence followed by a comparison of the unsteady and steady freestream data in aerodynamic loads and mechanism of stall to study the impact of the variable freestream.

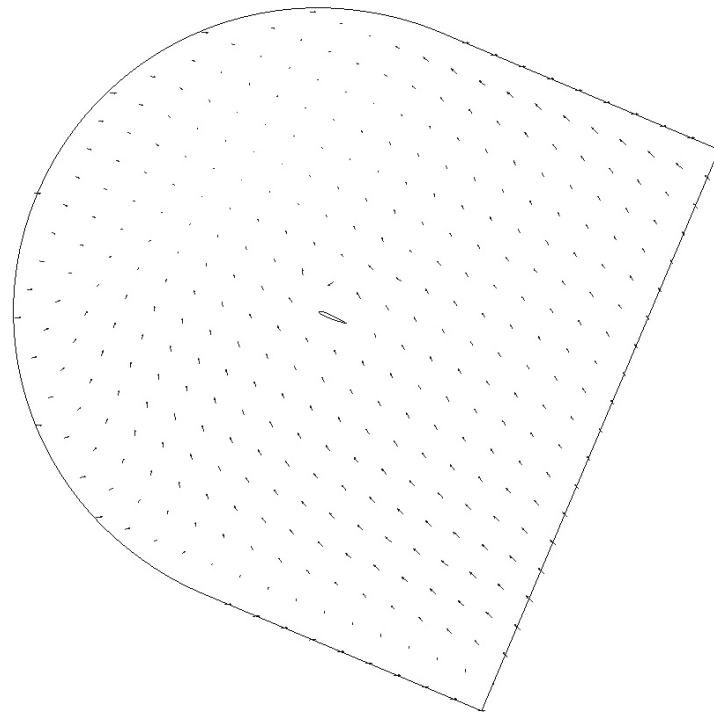
### 4.2.1 Boundary Conditions

The implementation of the variable freestream speed at the inlet was confirmed by examining the velocity vectors on the outer boundaries over one cycle, similarly to that shown in Figure 4.1. Although the velocity vectors at the boundary behaved as expected – the AOA and inlet velocity varying simultaneously – there was a short period during the

cycle (between azimuth angles  $219^\circ$  and  $295^\circ$ ) where two peculiar behaviours of the flow were observed. These behaviours are illustrated in Figure 4.6 where an unexpected presence of reverse flow throughout the domain was observed, as well as a region of vorticity at the section of the inlet boundary at the top of the domain.

The reverse flow region was not present in the steady freestream results, and so the boundary conditions were carefully reviewed to ensure that they were modelled correctly. It was suspected that this peculiar behaviour was possibly the result of an error in setting up the boundary conditions (for example, by incorrectly setting up the variable freestream definition, or by reflecting some of the information back into the domain). However, the velocity vector movies (see Appendix B) and Figure 4.6 prove that the boundaries are set up correctly, while vorticity and pressure contour movies (see Appendix B) confirmed that the boundaries were truly non-reflective. Therefore, it is believed that the temporary flow reversal is indeed physically possible and possibly caused by the rapid change in flow speed. Additional analysis to support this hypothesis is discussed later in the section describing the mechanism of dynamic stall in the variable freestream case.

The region of vorticity at the top of the domain (inlet boundary) appears to be non-physical, and occurs at the same time as the large recirculation zone. The vorticity appears to be caused by the interaction between the boundary velocity in the downstream direction, and the reverse flow in the opposite direction just inside the boundary. The effect of the velocity vectors in opposite directions is to create a “curl” effect. It is possible that this issue could be resolved by increasing the distance between the airfoil and the boundary from the current 10-chord radius, such that the reverse flow region is



(a)



(b)

**Figure 4.6:** Vector plot showing (a) velocity boundary conditions and (b) vorticity contours during reverse flow,  $232^\circ$  azimuth.

some distance away from the boundary. The top of the domain could also be changed from an inlet to an outlet, or the “timeVaryingInletOutlet” boundary, if it functions as it is intended, in theory would resolve the issue by acting as a “zeroGradient” condition when the airflow is directed out of the domain.

### 4.2.2 Convergence

The CFD solver converged to the specified residuals described above. Convergence was also evident in comparing the periodicity of the results, as shown in Figure 4.7. Although the results were not identically periodic even after 25 cycles, the differences between the cycles were minor enough that the results were considered to be converged. This was somewhat surprising as Gharali and Johnson (2013) and Kerho (2007) observed periodicity after one and 2.5 cycles, respectively.

### 4.2.3 Aerodynamic Loads

Plots of coefficients of lift, pitching moment and drag versus angle of attack for the last cycle of rotation are shown in Figure 4.8. The CFD results show significant differences with respect to the steady freestream case data.

The drag for the variable freestream case was higher than the experimental data from  $\alpha = 0^\circ - 17^\circ$  in both directions. Beyond  $17^\circ$ , the upstroke drag was generally less for the variable freestream case, and the downstroke drag was generally greater than the steady freestream case. The only exception is the increase in drag at  $23^\circ$  for both cases: the increase in drag for the variable freestream case is exaggerated compared to the steady

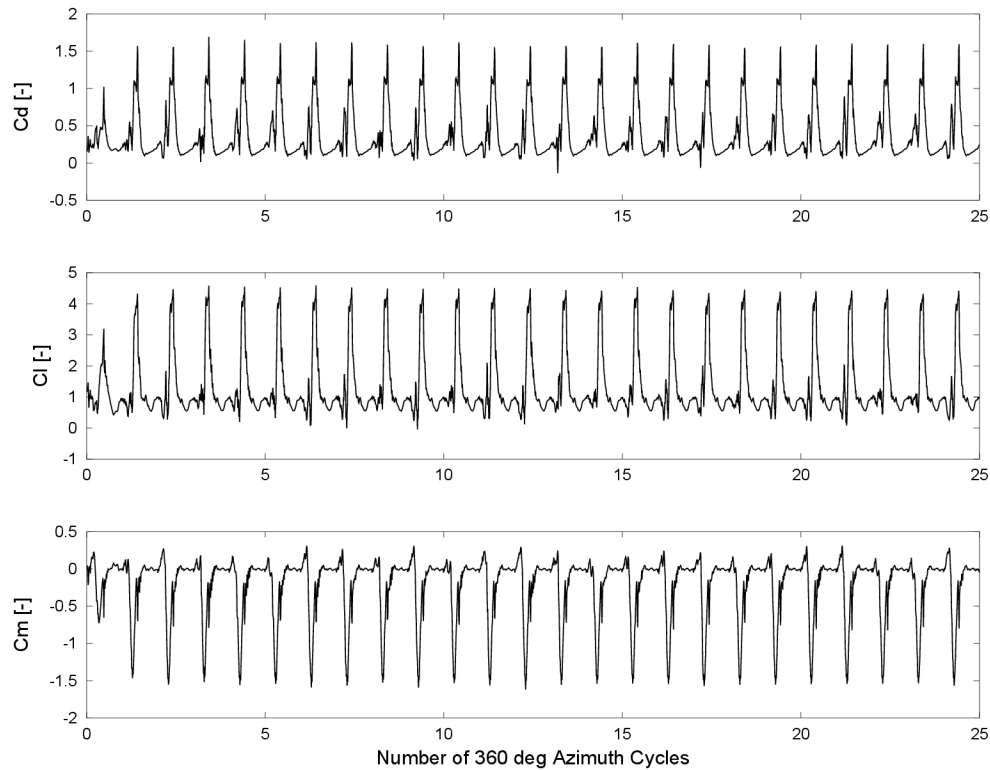


**Figure 4.7:** Time-history of aerodynamic loads, Case 2 variable freestream. Each cycle begins at  $169^\circ$  azimuth measured at the airfoil.

freestream case, to the point that the drag increases beyond the steady freestream results. Note, however, that this coincides with the occurrence of reversed flow in the domain.

It was also observed that, contrary to the steady freestream data, the variable freestream case produced higher drag on the upstroke between  $\alpha = 0^\circ - 14^\circ$ , and higher drag on the downstroke between  $14^\circ - 25^\circ$ . This difference in the behaviour can be attributed to shock-induced boundary layer separation, which would quite logically increase drag below  $\alpha = 18^\circ$ . In addition, reverse flow on the upstroke and LEV and TEV shedding on the downstroke also contribute to the change in drag at angles of attack

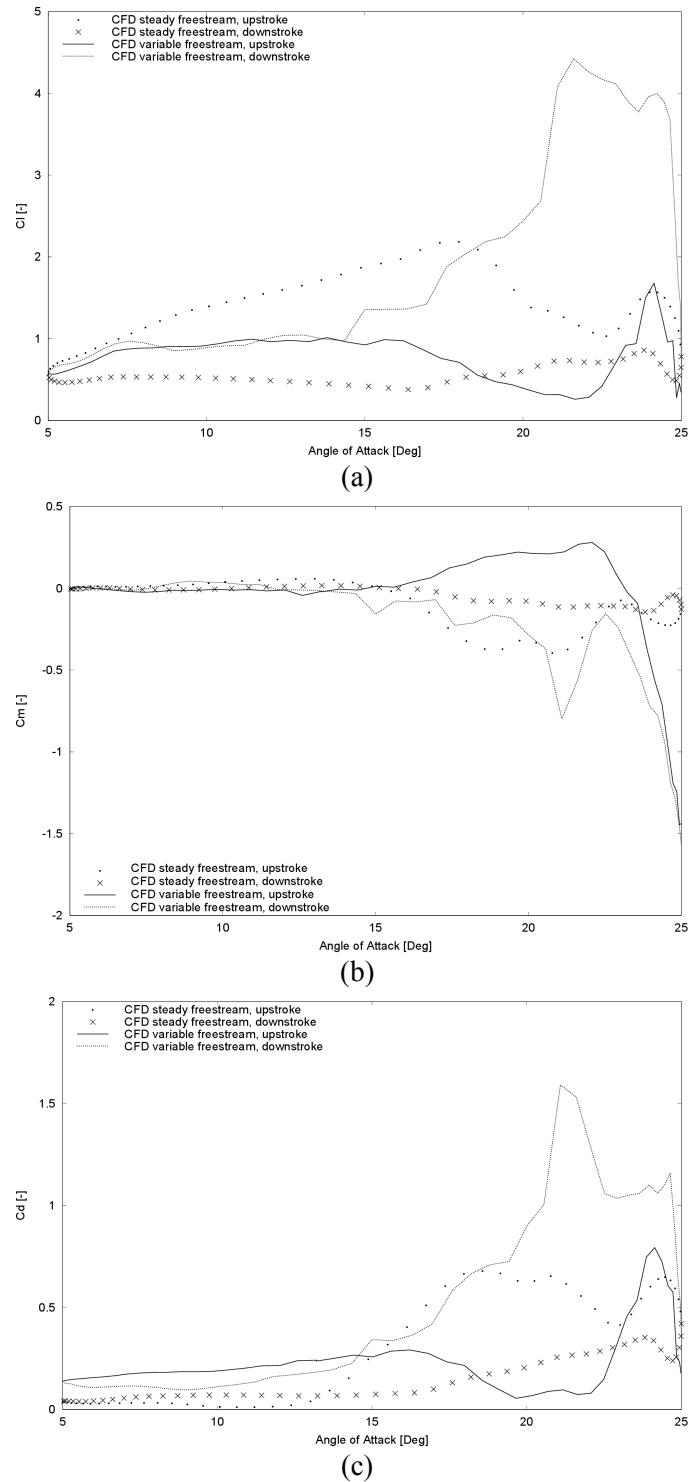


**Figure 4.8:** Comparison of (a) lift, (b) pitching moment and (c) drag coefficients from Cases 1 and 2 of this work. The flow conditions correspond to  $M = 0.292$ ,  $Re = 3.76 \times 10^6$ ,  $\alpha = 15 \pm 10$  degrees and  $k = 0.1$  for Case 1 (steady freestream);  $M = 0.48 \pm 0.3$ ,  $Re = 3.3 \times 10^6 \pm 2.1 \times 10^6$ ,  $\alpha = 15 \pm 10$  degrees and  $k = 0.018 - 0.078$  for Case 2 (variable freestream).

above  $18^\circ$ . The peak drag was greater and occurred later in the azimuth, as shown in Table 4.2.

The lift data for the variable freestream also deviated significantly from the steady freestream data. The steady freestream lift data generally follows the quasi-static airfoil lift-curve slope until the point of stall. The variable freestream data - on the other hand - deviates from the lift-curve slope near  $\alpha = 7.5^\circ$  when the shockwave on the suction surface has retreated to  $0.3c$ , and then remains roughly constant until  $16^\circ$  where the shockwave disappears at the leading edge. Then, lift begins to decrease steadily until  $\alpha = 22^\circ$ , when the freestream begins the transition from reverse flow back to regular flow. At that point, the lift reaches its local maximum at  $\alpha = 24^\circ$  due to the presence of an unusually strong TEV before dropping to a minimum at  $25^\circ$  as the LEV is convected beyond the trailing edge of the airfoil. At the beginning of the downstroke, the lift increases rapidly to a maximum and lift stall at  $\alpha = 22^\circ$ , just before flow separation begins. Then, lift decreases rapidly until  $\alpha = 20^\circ$ , at which point the rate of decrease in lift is reduced as the area of the wake region is reduced by the decreasing angle of attack. At  $\alpha = 14^\circ$ , the lift-curves on the upstroke and downstroke overlap, which would

**Table 4.2:** Comparison of variable freestream CFD results to steady freestream experimental data. Arrows next to angle of attack figures indicate upstroke or downstroke.

Parameter [units]	CFD	Experimental	Difference
Negative Peak $C_m$ [-]	-1.57	-0.405	+286.1%
Peak $C_d$ [-]	1.59	0.766	+108.8%
Peak $C_l$ [-]	4.42	1.946	+127.2%
Moment stall $\alpha$ [ $^\circ$ ]	22.5 $\uparrow$	16.5 $\uparrow$	Delayed
Lift stall $\alpha$ [ $^\circ$ ]	21.6 $\downarrow$	20.3 $\uparrow$	Delayed

normally coincide with the corresponding quasi-static airfoil data and indicate flow reattachment in a dynamic stall case. However, in the variable freestream case the lift at this point is less than that of the quasi-static airfoil, and the similarity in data between up- and down-stroke is attributed to the presence of a shockwave at  $0.05c$  which separates the flow downstream in both motions. The lift data matches the steady freestream results below  $7.5^\circ$ , though this does not indicate reattachment since the presence of shock-induced flow separation in this region prevents flow reattachment over the complete airfoil chord. This is in contrast to the steady case where the flow appeared qualitatively to reattach at  $\alpha = 11^\circ$ , but quantitatively the lift data on the up- and down-strokes only converged at the end of the downstroke. The peak lift was greater and occurred later in the azimuth, as shown in Table 4.2. Especially notable was that peak lift was delayed to the downstroke, where the literature review suggested that even in deep stall conditions the lift stall occurs at the maximum angle of attack.

The pitching moment graph showed a peak positive pitching moment (moment stall) greater in magnitude and much later in the upstroke than in the steady freestream case,  $\alpha = 22^\circ$  versus  $\alpha = 13^\circ$ , respectively. Despite being delayed much later in the upstroke, the pitching moment stall took place before the lift stall, typical of dynamic stall behaviour. The pitching moment reached a minimum at the maximum angle of attack as the TEV convected into the wake. Effectively, one large loop existed providing significant negative aerodynamic damping. The number of loops and amount of negative damping is unusual for deep dynamic stall, but as with the steady freestream results, this observation is noted here but will not be discussed further since aerodynamic damping is

not the focus of this thesis. The peak pitching moment was greater in magnitude and occurred later in the azimuth, as shown in Table 4.2.

Numerical simulations of dynamic stall typically match experimental data to a lesser extent on the downstroke where airflow is not attached. In the variable freestream case, significant portions of the upstroke and downstroke experienced separated flow, therefore it is possible that the discrepancy with respect to experimental data, should such an experiment be carried out in the future, would be greater than for steady freestream simulations on the upstroke as well. It was observed in the literature review that changes in the parameters affecting dynamic stall have a quantitative and not qualitative effect on the mechanism of dynamic stall. The results discussed above clearly agree that a significant quantitative impact was present; it will be shown in the next section that the presence of the variable freestream caused significant qualitative changes as well. Contrary to the results of Gharali and Johnson (2013), the variable freestream 180° out of phase with the velocity did not decrease the loads; rather in this case they were significantly increased. This difference may be attributed to the different conditions at which this research and the Gharali and Johnson (2013) case were carried out.

#### **4.2.4 Mechanism of Dynamic Stall at Variable Freestream**

This section of the thesis discusses the mechanism of dynamic stall in the presence of a variable freestream by analyzing a sequence of two sets of images, corresponding to points in the azimuth with lift and pitching moment data shown in Figure 4.9. These points refer to images of pressure contours and velocity vectors in the first column and Mach

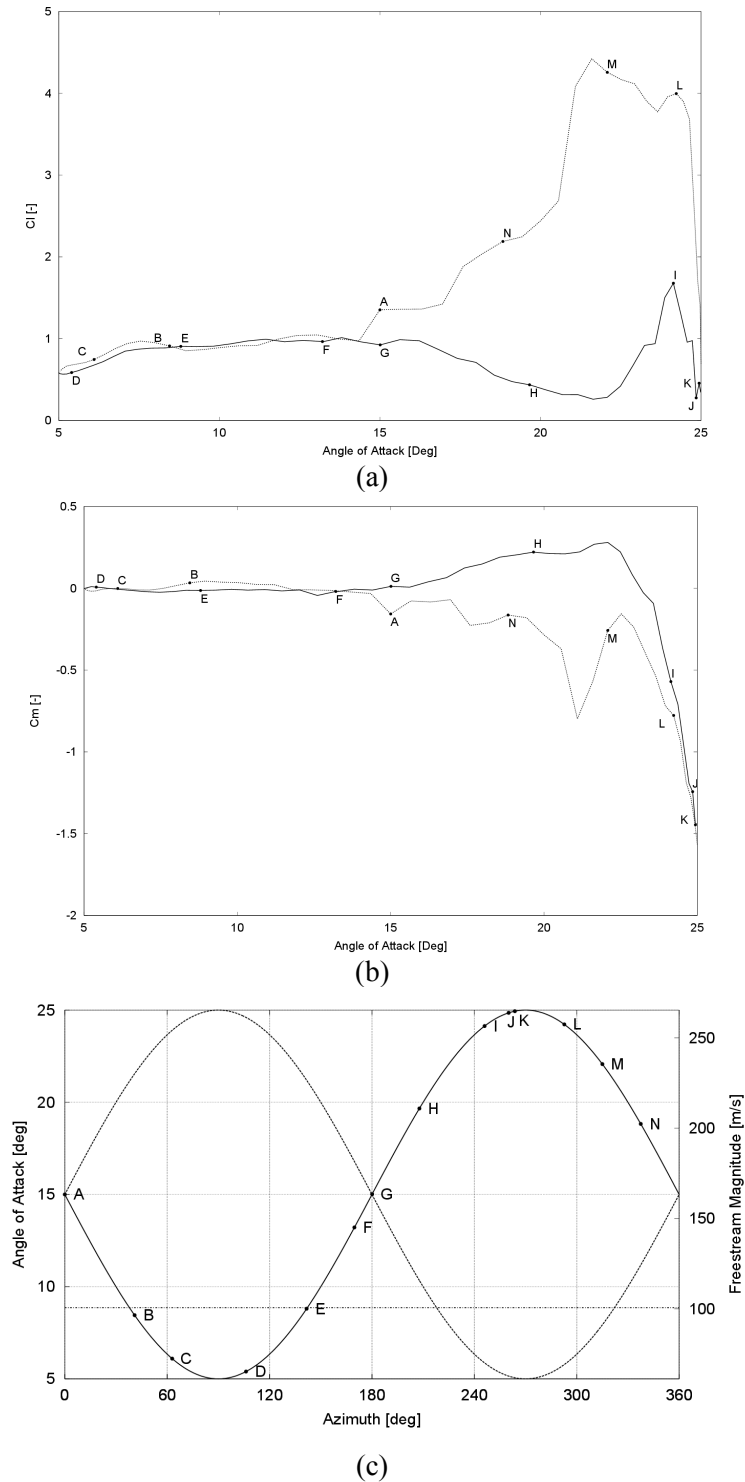


**Figure 4.9:** Positions of images in Figure 4.10 indicated on coefficient of (a) lift and (b) pitching moment CFD results for Case 2. The solid line indicates the upstroke and the dashed line indicates the downstroke. (c) Azimuthal positions of images of Figure 4.10. dashed line is speed, solid line is the angle of attack.

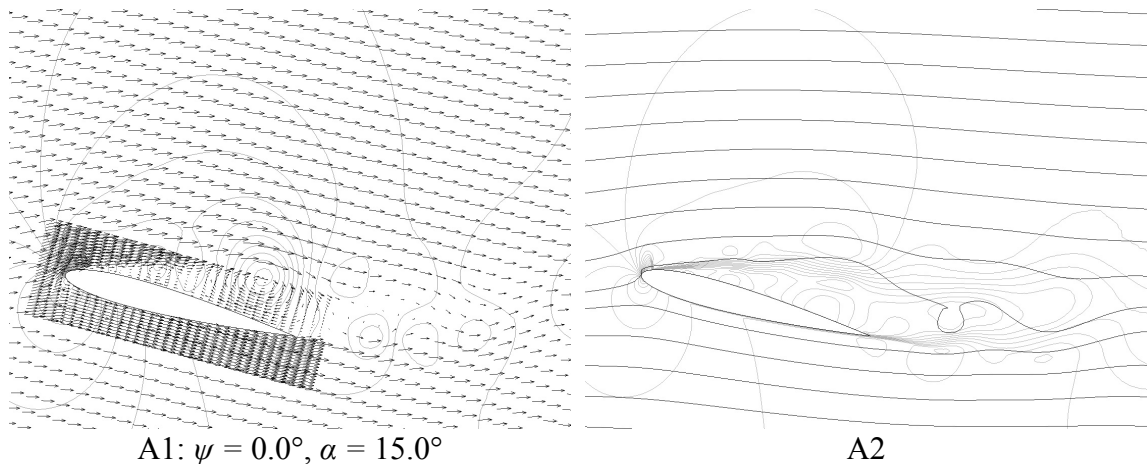
number contours and streamlines in the second column, together forming Figure 4.10. The discussion that follows makes reference to sub-images of Figure 4.10 by indicating the sub-image reference letter in parentheses.

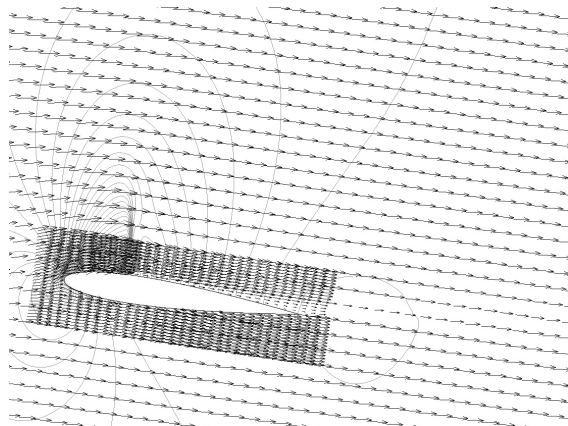
The decrease in angle of attack on the downstroke is accompanied by an increase in Mach number, and the formation of a shock wave at the leading edge of the airfoil (frame A). The increasing Mach number and decreasing angle of attack as the downstroke continues to cause the shock wave to move aft over the airfoil and increase in strength (frames B, C) to a maximum at the bottom of the downstroke (frame D). The pitch-up motion results in the shock wave decreasing in strength and moving forward (frame E). Throughout the azimuth where the shock wave was present, the boundary layer was attached upstream of the shock and separated downstream of the shock. Effectively, the shock wave prevented complete boundary layer reattachment from taking place.

As the shock wave moved toward the leading edge and dissipated, it caused complete separation of the boundary layer, shed several vortices on the upstroke (frame F) and formed a small TEV and small LEV (frame G). As the angle of attack increases further, a strong TEV is formed (frame H) which appears to contribute to the generation of a LEV which is formed near the mid-chord. The relatively fast-moving freestream above the relatively slow-moving wake tends to create a clockwise vortex. The formation of the counter-clockwise TEV increases the magnitude of the upstream flow in the wake of the airfoil, which adds vorticity to the LEV. As the angle of attack increases beyond  $\alpha = 20.7^\circ$ , the LEV and TEV continue to grow in size and intensity, and begin to move both upstream and up, away from the airfoil. The TEV moves as far upstream as the mid-chord

(frame I).

A significant region of reverse flow dominates the region surrounding the airfoil until the TEV is convected into the wake as the downstroke begins (frames J, K). The reverse flow may be caused by the increased strength of the LEV and TEV under variable freestream flow. The flow around the airfoil is also undergoing a very rapid change from compressible to incompressible flow during the upstroke. Given that information propagates in all directions at subsonic speeds, and the LEV convects at a fraction of the speed of the freestream, it is possible that the reverse flow could be a result of the combination of the low freestream speed and an extremely strong vortex – created at much faster freestream conditions – with the entrainment caused by the vortex overcoming the local freestream. Despite the high angle of attack, the boundary layer reattaches briefly (frames K, L) once the TEV has moved well downstroke of the airfoil, until shock-induced flow separation begins on the downstroke (frame M) and shedding of vortices begins (frame N).

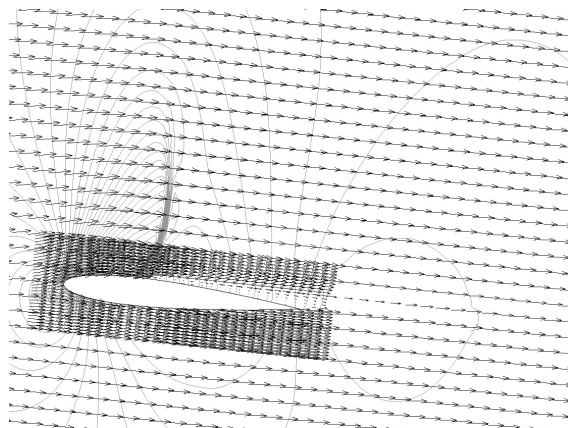




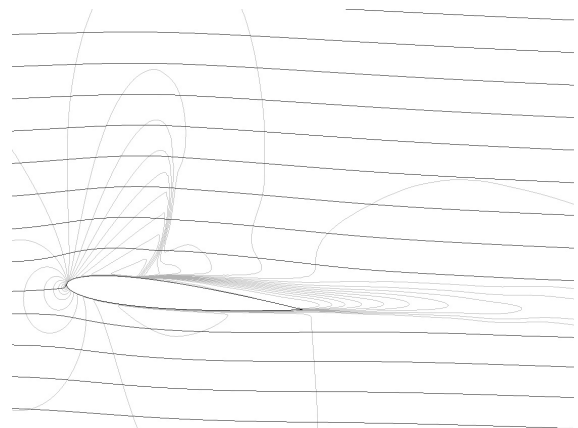
B1:  $\psi = 40.9^\circ, \alpha = 8.5^\circ$



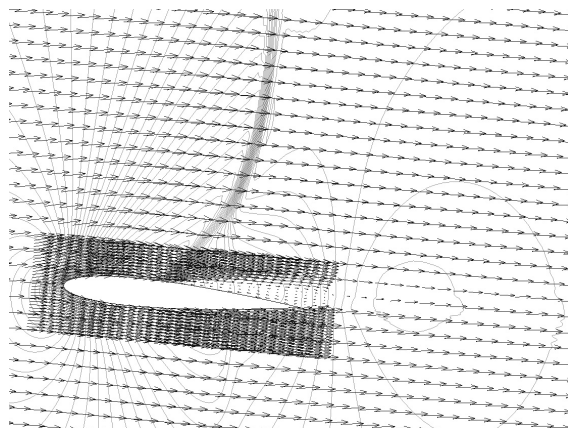
B2



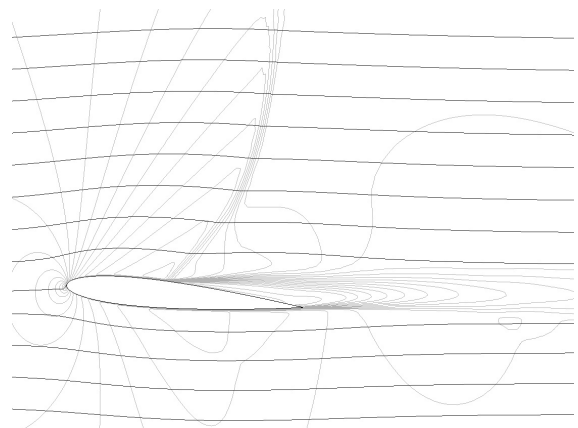
C1:  $\psi = 62.9^\circ, \alpha = 6.1^\circ$



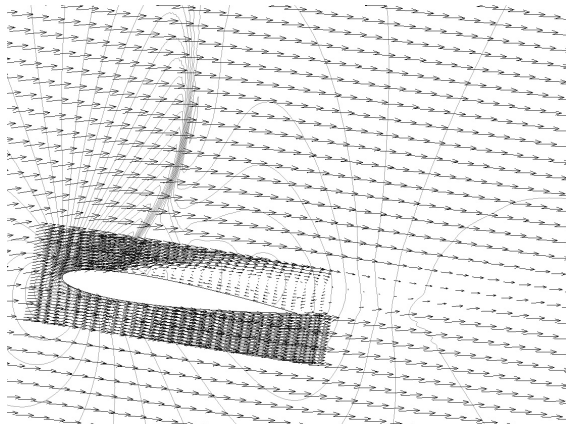
C2



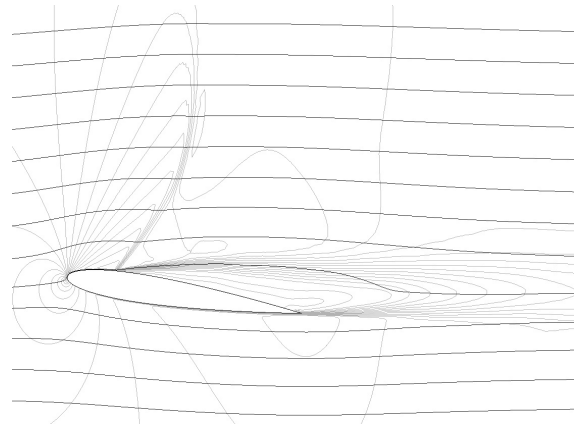
D1:  $\psi = 106.2^\circ, \alpha = 5.4^\circ$



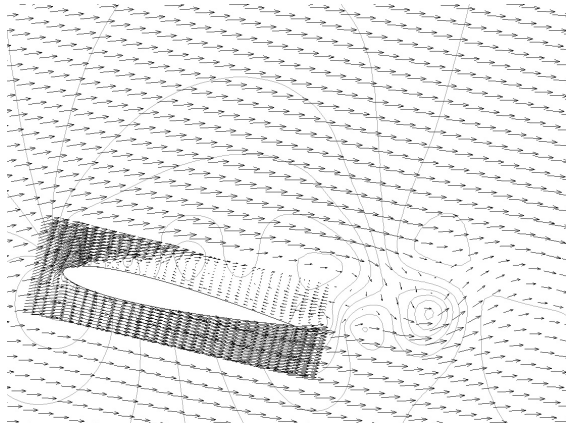
D2



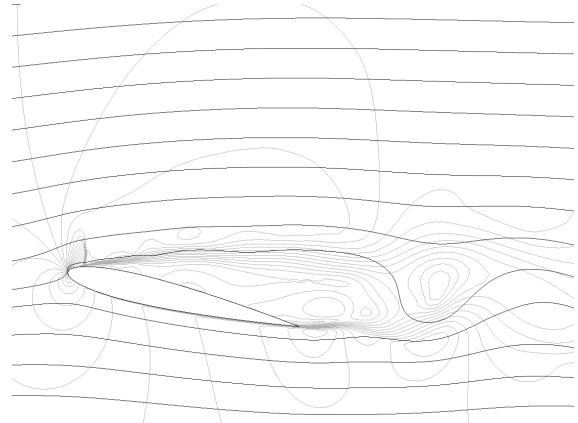
E1:  $\psi = 141.7^\circ, \alpha = 8.8^\circ$



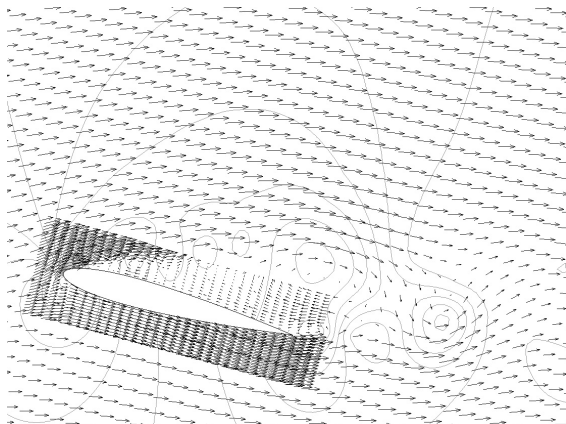
E2



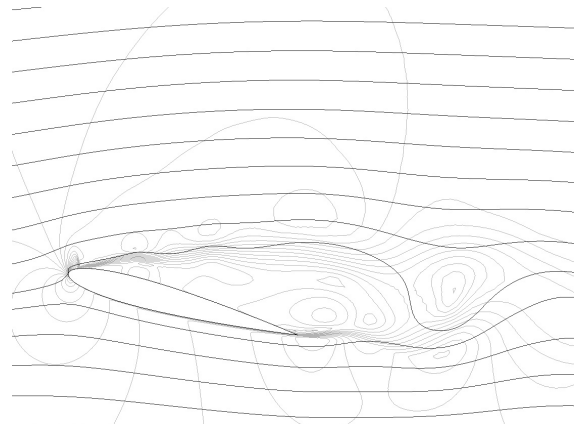
F1:  $\psi = 169.7^\circ, \alpha = 13.2^\circ$



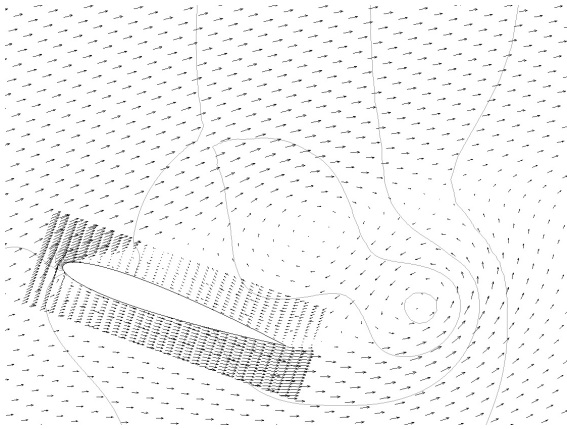
F2



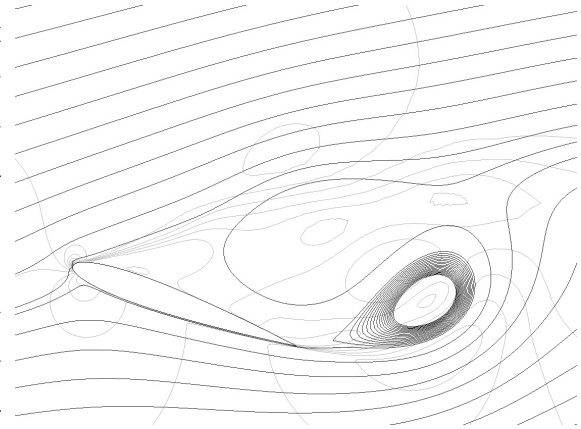
G1:  $\psi = 180.1^\circ, \alpha = 15.0^\circ$



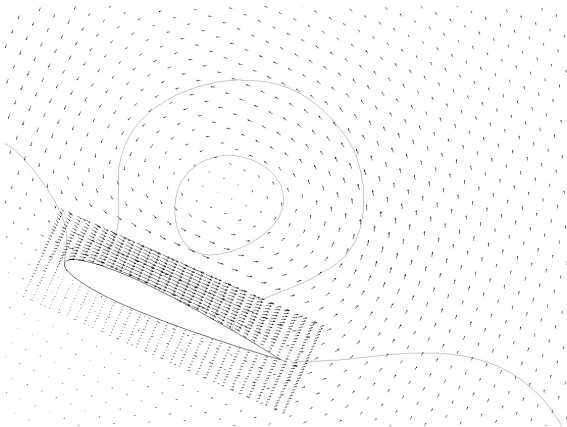
G2



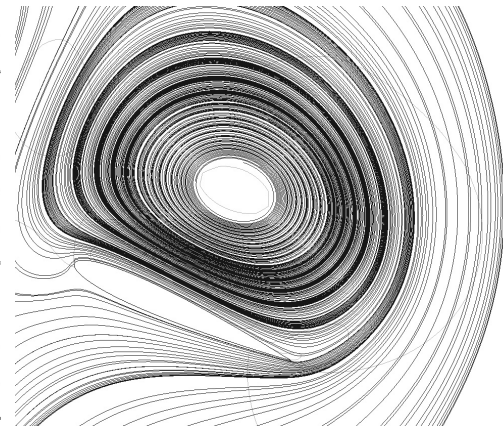
H1:  $\psi = 207.8^\circ, \alpha = 19.7^\circ$



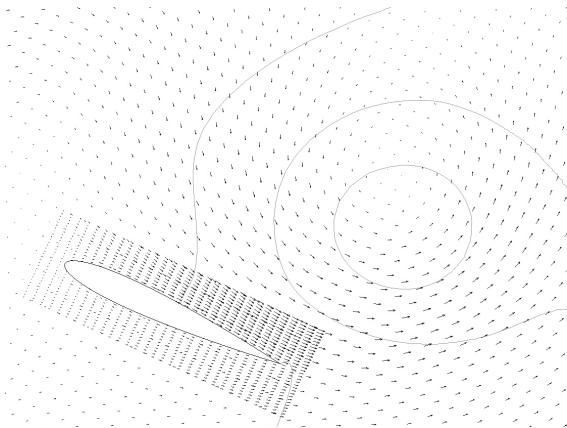
H2



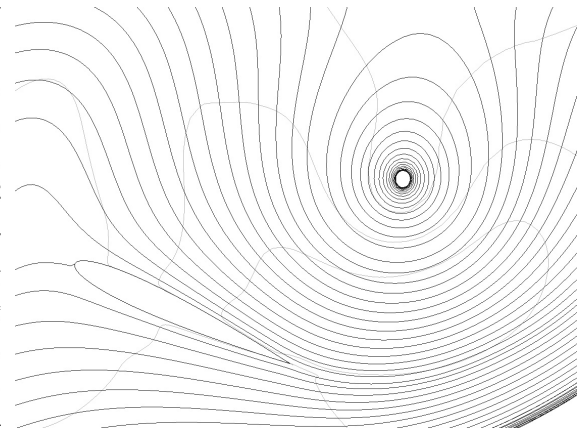
I1:  $\psi = 246.0^\circ, \alpha = 24.1^\circ$



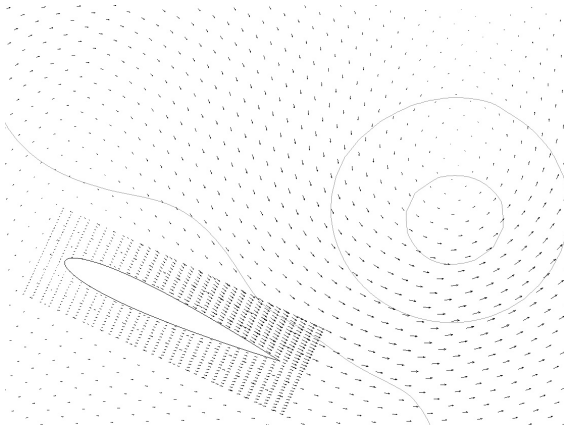
I2



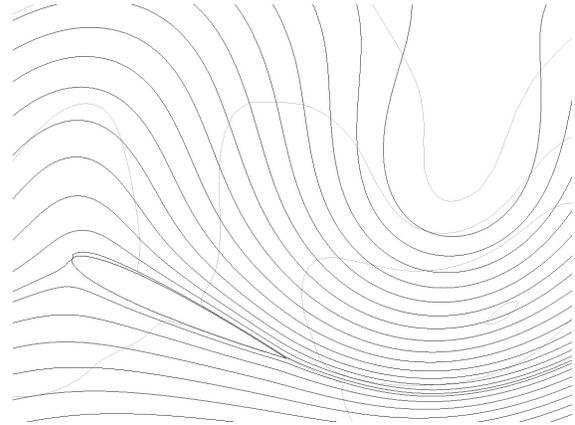
J1:  $\psi = 260.1^\circ, \alpha = 24.9^\circ$



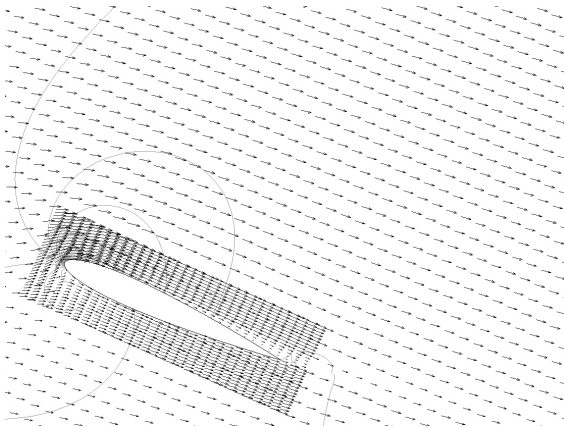
J2



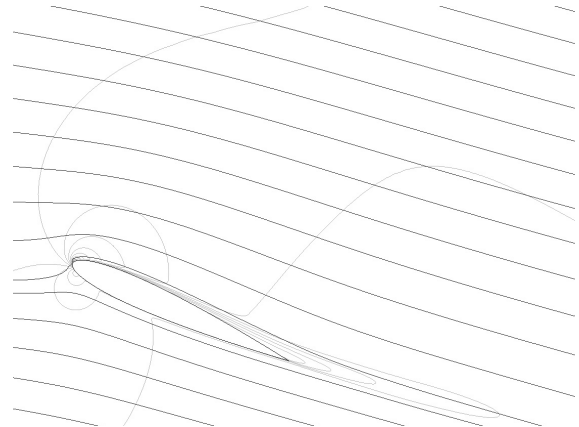
K1:  $\psi = 263.7^\circ, \alpha = 24.9^\circ$



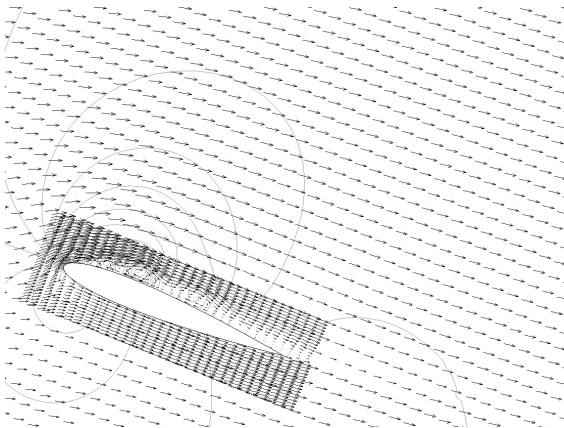
K2



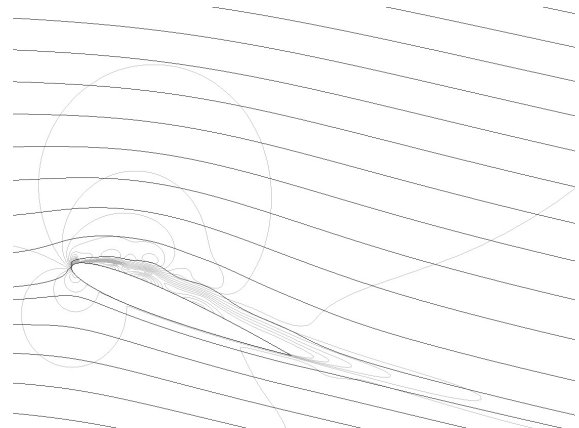
L1:  $\psi = 292.7^\circ, \alpha = 24.2^\circ$



L2



M1:  $\psi = 315.0^\circ, \alpha = 22.1^\circ$



M2

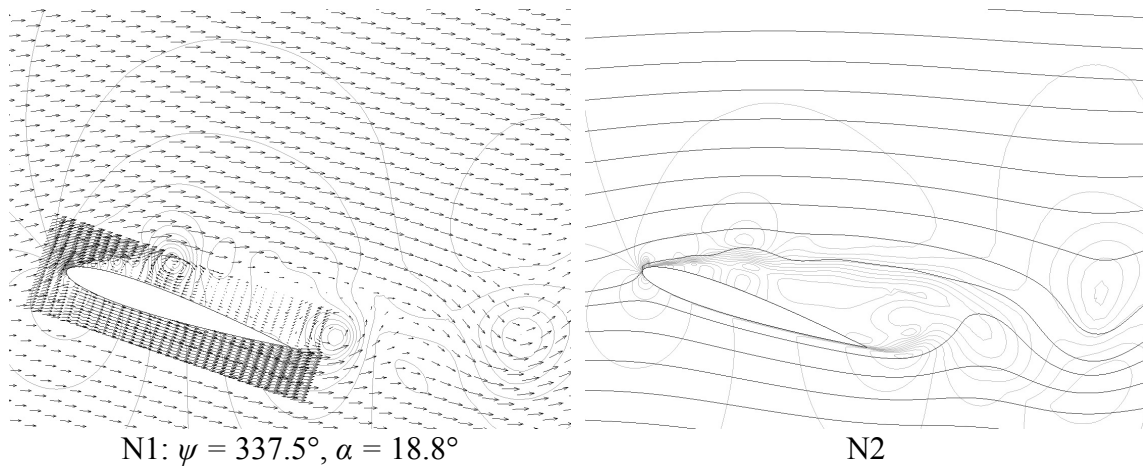


**Figure 4.10:** Velocity vector plots and pressure contours (left column) and Mach contours and streamline plots (right column), corresponding to the positions of the points indicated in Figure 4.9, respectively. Pressure contours show a minimum of 12.5 kPa, a maximum of 250 kPa, with 76 contours at intervals of 3.125 kPa. Mach contours show a minimum of  $M = 0$ , a maximum of  $M = 1.75$ , with 25 contours at intervals of  $M = 0.07$ . The data is taken from Case 2:  $\alpha = 15^\circ \pm 10^\circ \sin(\Omega t + \pi)$ ,  $k_{avg} = 0.0293$ ,  $M = 0.48 \pm 0.3 \sin \Omega t$ ,  $Re_{avg} = 3.31 \times 10^6$ .

#### 4.2.5 Comparison of Steady and Variable Freestream Mechanisms

The qualitative features of both steady and variable freestream cases vary significantly, as shown by a comparison of flowfiled data. Note that the frames for both steady and variable freestream are taken at the same azimuths and therefore angles of attack, to enable a direct comparison. The points corresponding to the lift and pitching moment data are shown in Figure 4.11. These images are shown in Figure 4.12. Below the angle of static stall, the boundary layer is mostly attached in the steady freestream case, whereas in the variable freestream case shock-induced boundary layer separation prevents reattachment in this region of the azimuth (frames A-E). Above the static stall angle, on the upstroke the shock-induced separation causes the formation of many vortices behind the variable freestream airfoil, while the steady freestream airfoil begins to generate a LEV (frame F). The disorganized flow continues under variable freestream

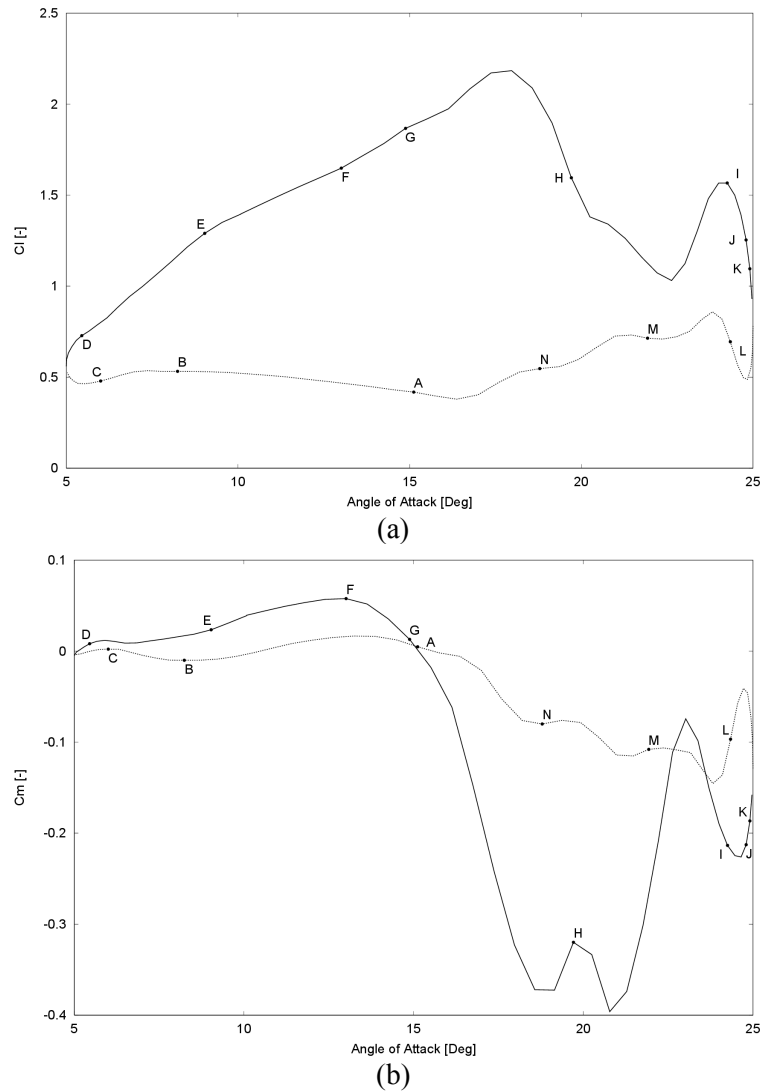


**Figure 4.11:** Positions of images in Figure 4.12 indicated on (a) coefficient of lift and (b) pitching moment CFD results for Case 1. The solid line indicates the upstroke and the dashed line indicates the downstroke.

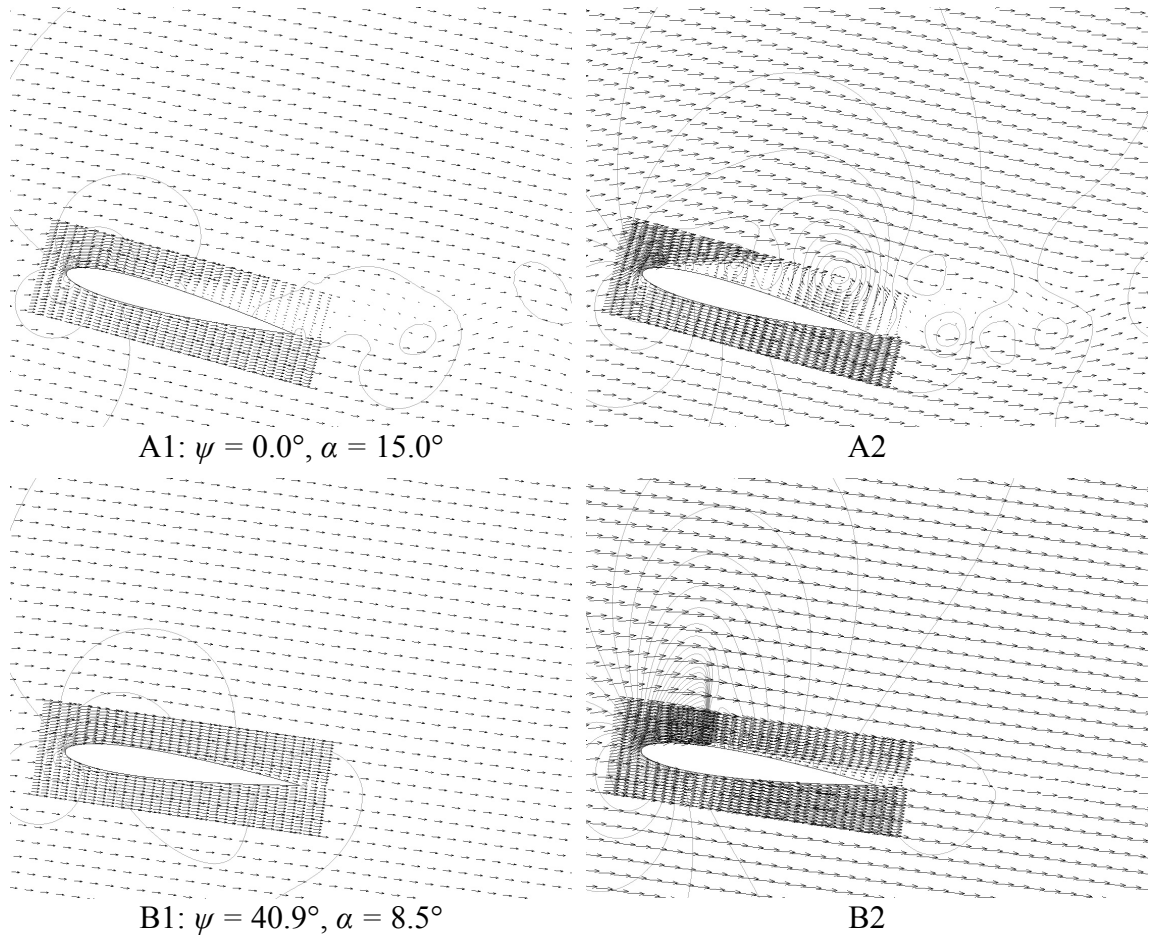
conditions as the LEV grows and convects aft under steady freestream conditions (frame G). TEV formation begins on the steady freestream airfoil as the LEV is convected to the trailing edge of the airfoil, whereas the variable freestream airfoil has generated a much stronger and larger TEV by that point, which has already convected into the wake (frame H). As the angle of attack continues to increase, the reverse flow region grows over the

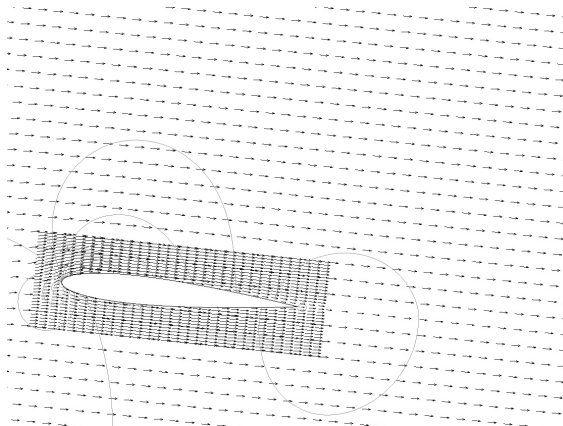
variable freestream airfoil and the TEV grows in size and convects upstream over the mid-chord, while the first LEV has convected over the TEV and a second LEV forms and pushes the TEV off the trailing edge of the steady freestream airfoil (frame I). Nearing the peak angle of attack, the LEV and TEV begin to move downstream of the airfoil in the variable freestream and the second LEV pauses over the steady freestream airfoil as the second TEV grows (frames J, K). The convection of the strong LEV and TEV into the wake in the variable freestream is followed by a brief period of flow attachment (frame L) before shock-induced separation returns (frames M, N), whereas the LEV and TEV are not shed into the wake until much later (frame M) in the steady freestream case and the flow reattachment begins similarly later in the cycle (frame N).

The primary differences between the two types of freestream flow are the presence of the shockwave at low angle of attack, the shock-induced separation of the boundary layer rather than breakdown of the turbulent boundary layer, less organized flow versus a series of clearly defined LEVs and TEVs, and the faster formation, growth, and dissipation as well as greater intensity of the LEV and TEV for the variable freestream case. The TEV plays a more dominant role in the variable freestream case, and the intense region of reverse flow is unique to that case as well. The rapidity of formation, growth and convection of the LEV and TEV are especially notable given that the reduced frequency and freestream magnitude are lower in the variable freestream case at the azimuth where these occur (frames I – M).

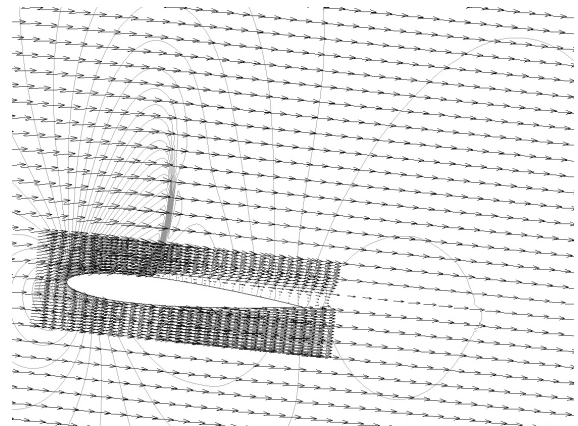
Some of the differences between the results of the steady and variable freestream cases may be caused by the standard parameters which affect dynamic stall, varying

significantly as a function of azimuth. Reynolds number, Mach number and reduced frequency were all affected as a result of the variable freestream, the effects of which will be examined in greater detail in the following sections.

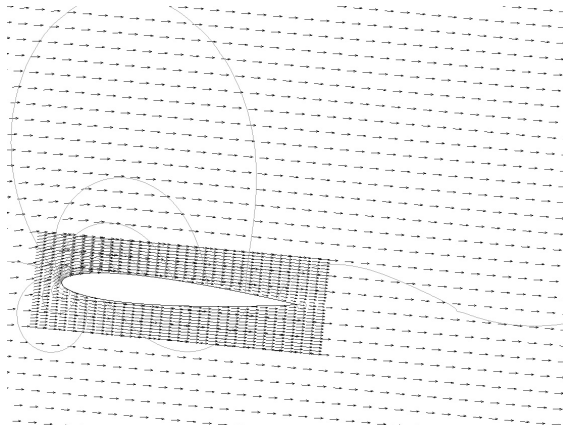




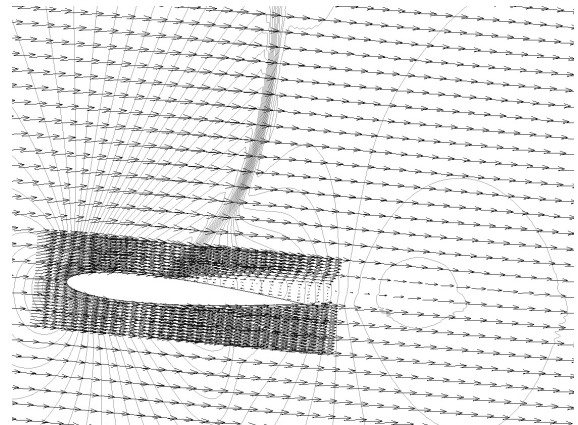
C1:  $\psi = 62.9^\circ, \alpha = 6.1^\circ$



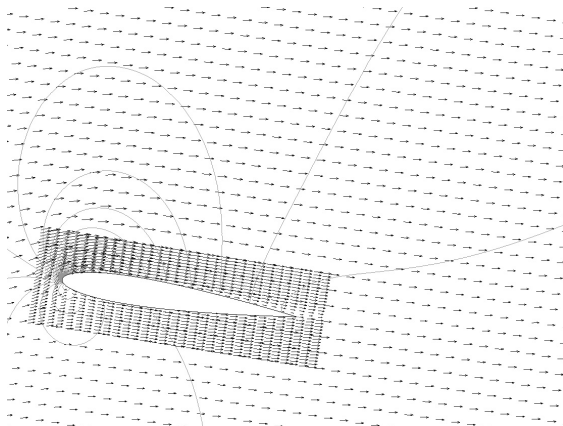
C2



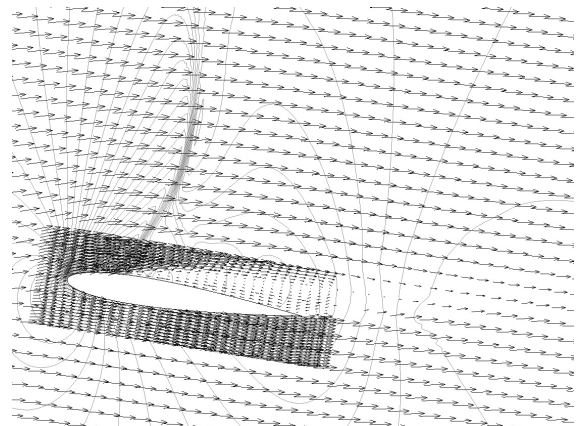
D1:  $\psi = 106.2^\circ, \alpha = 5.4^\circ$



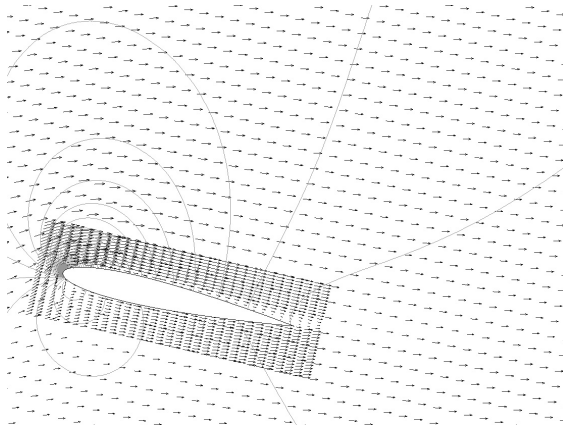
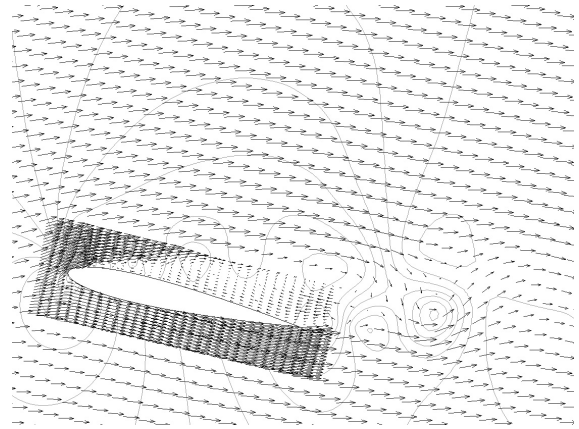
D2



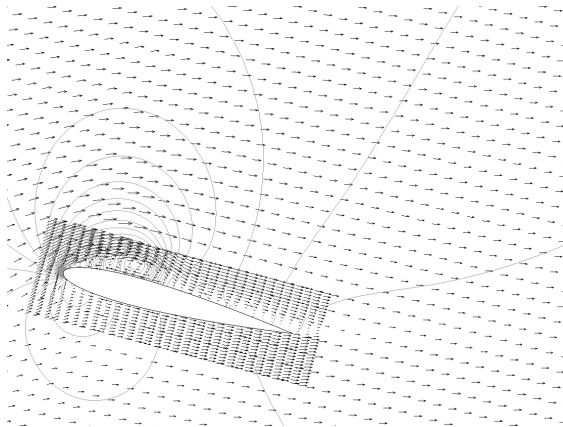
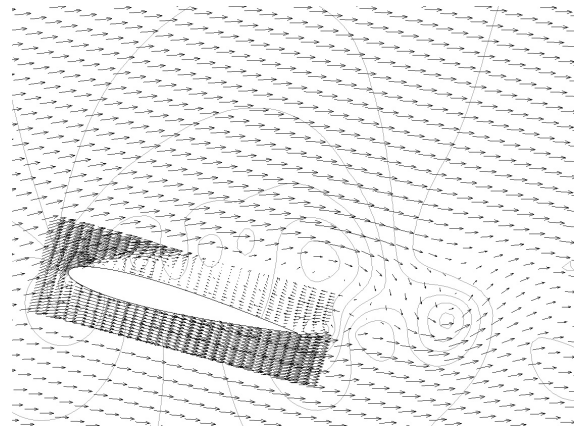
E1:  $\psi = 141.7^\circ, \alpha = 8.8^\circ$



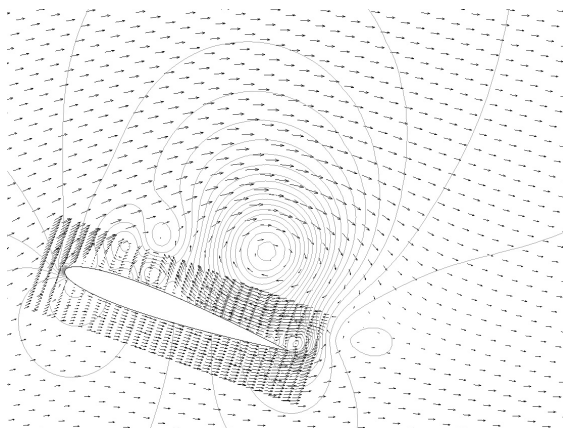
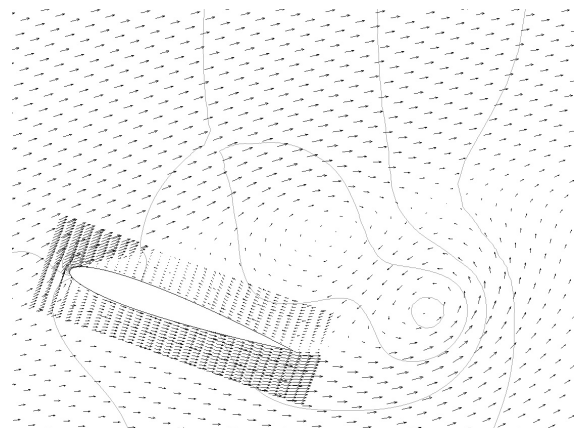
E2

F1:  $\psi = 169.7^\circ, \alpha = 13.2^\circ$ 

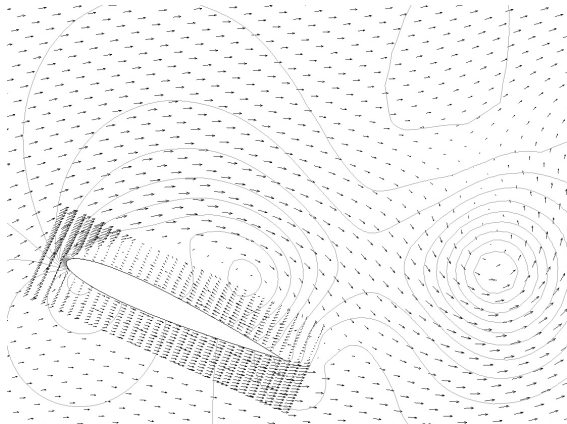
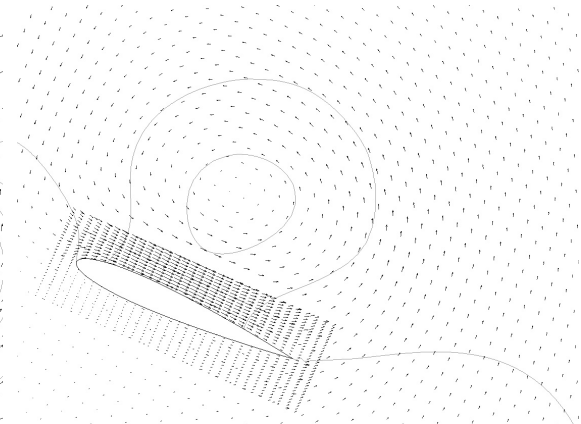
F2

G1:  $\psi = 180.1^\circ, \alpha = 15.0^\circ$ 

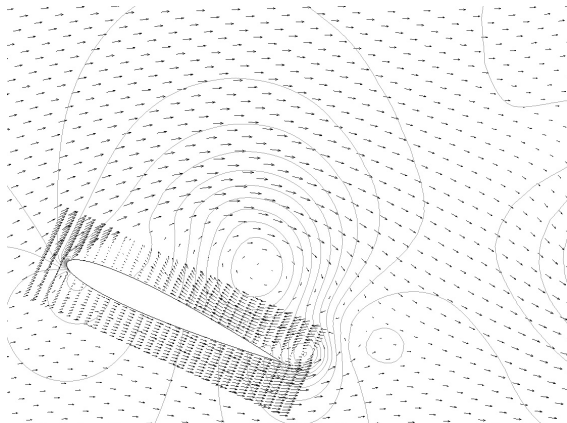
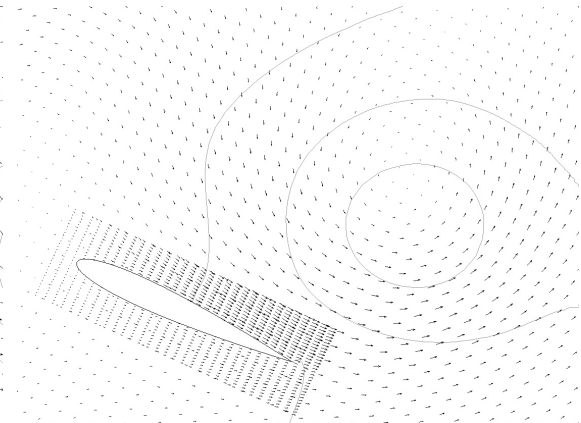
G2

H1:  $\psi = 207.8^\circ, \alpha = 19.7^\circ$ 

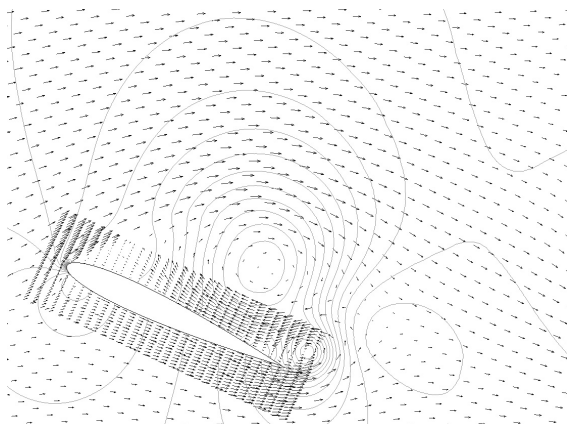
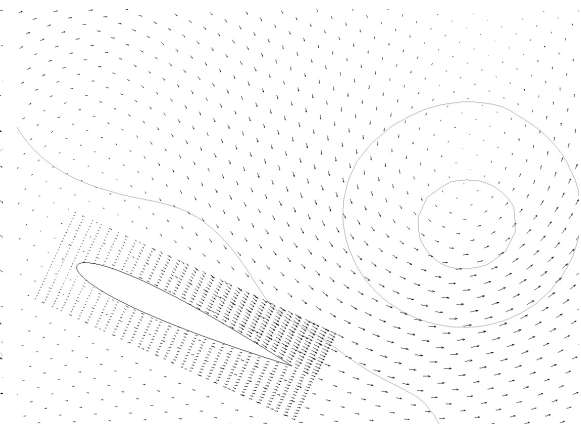
H2

I1:  $\psi = 246.0^\circ$ ,  $\alpha = 24.1^\circ$ 

I2

J1:  $\psi = 260.1^\circ$ ,  $\alpha = 24.9^\circ$ 

J2

K1:  $\psi = 263.7^\circ$ ,  $\alpha = 24.9^\circ$ 

K2

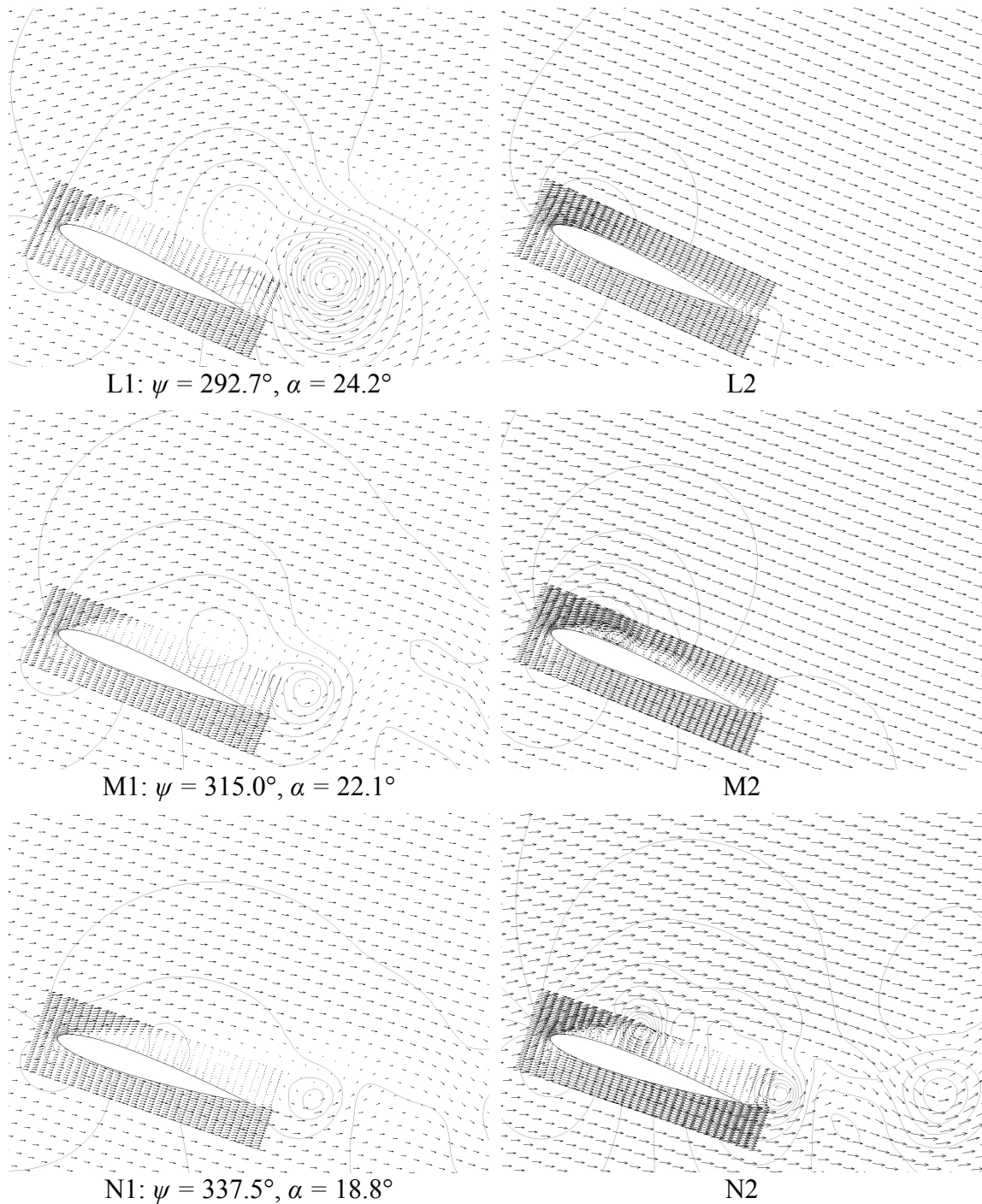


**Figure 4.12:** Comparison of steady freestream (left column) and variable freestream (right column) pressure contours and velocity vector data, corresponding to the positions of the points indicated in Figure 4.11, respectively. The scales and units of the images in this figure are consistent with those presented in Figure 4.5 and Figure 4.10.

#### **4.2.5.1 Reynolds Number Effect**

An increase in Reynolds number is associated with an increase in peak lift and pitching moment, both of which were observed in the dynamic freestream case and the Reynolds number, although on average lower than the steady freestream case, did exceed that of the steady freestream case during the low angle of attack region of the azimuth.

#### **4.2.5.2 Mach Number Effect**

An increase in Mach number promotes flow separation, which is consistent with the observations when comparing the two cases. The literature review indicated that shock waves present at the leading edge may cause dynamic stall to take place and increase the complexity of the center of pressure behaviour during boundary layer separation and reattachment. This expectations was consistent with the results of the variable freestream case, though the lower peak lift and weaker LEV that typically accompany high Mach numbers were not observed, probably due to the Mach number being lower than the reference steady case during the high angle of attack region of the azimuth of rotation. The literature review suggested that a lambda shock wave translating across the chord would be responsible for negative damping, however while the lambda shock wave was present, it caused separated flow equally on the upstroke and downstroke making the damping neutral in the relevant region. It is possible that the lambda shock wave's effects on damping were neutralized by its disappearance as the angle of attack increased and the Mach number decreased due to the variable freestream.

### 4.2.5.3 Reduced Frequency Effect

The reduced frequency is an inverse function of the freestream speed, and therefore it increases as the angle of attack increases and the velocity decreases. Increasing  $k$  delays the formation and shedding of the LEV, which was observed in the results to be consistent with the theory. Aerodynamic damping also increases with an increase in  $k$ , which could explain how the pitching moment hysteresis loop is much larger than the steady case at high angles of attack, but is almost not present at low angles of attack. McAlister *et al.* (1978) suggested that LEV strength could be related to airfoil circulation at the instant of formation, and a stronger LEV was observed in the variable freestream case at higher  $k$ . Although the variable freestream  $k$  increased at higher angles of attack, it did not exceed that of the steady freestream case at any point which suggests that the change in reduced frequency alone cannot be responsible for the change in behaviour.

### 4.2.5.4 Variable Freestream Effect: Comparison to Literature

Pierce *et al.* (1978) reported that a variable freestream had little effect on aerodynamic damping but a large effect on the moment near stall; these results show significant effects on both damping and moment near stall. Gharali and Johnson (2013) reported that lift is decreased when the increase in freestream and angle of attack are out of phase, which is contrary to the results obtained in this research. Shi and Ming (2008 and 2009) stated that a slowing freestream during pitch-up can delay dynamic stall, which is supported by these results, though reattachment was not delayed compared to the reference case as suggested by the same research. This paper also showed that a slowing freestream during pitch-up increases  $C_{lmax}$ . Kerho (1997) observed a small increase in lift

---

stall angle and peak lift as a result of the variable Mach number, though the effects were noted for the CAMRAD II angle of attack motion profile and not the sinusoidal profile used here.

Therefore, the observations of these simulations suggest a fundamental difference in the qualitative and quantitative mechanism of dynamic stall due to a variable freestream at representative helicopter flight conditions. This observation is important since it suggests the only evidence to date of the mechanism of dynamic stall being fundamentally altered by a parameter; all others simply affect the timing of the events but not the sequence. The change in sequence in this case refers to the formation of the TEV and the predominant role played by that structure as opposed to the LEV.

## **Chapter 5**

# **Conclusions and Recommendations**

### **5.1 Conclusions**

In the course of this research, two-dimensional dynamic stall of a helicopter rotor blade section with a variable freestream was studied to determine the impact of a variable freestream on the mechanism of dynamic stall, and as a result assess the validity of dynamic stall models that do not consider a variable freestream. This study represents, to the best of the author's knowledge, the first application of representative helicopter flight conditions to a variable magnitude freestream speed dynamic stall simulation. Since it is believed to have not been accomplished by experiment either, the results of this thesis are novel and represent a valuable contribution to the growing body of work studying dynamic stall.

An unsteady Reynolds-averaged Navier-Stokes computational fluid dynamics code,

OpenFOAM, was used to model the problem using a structured C-grid. The changes in angle of attack and freestream as a function of time were applied by changing the inlet velocity boundary condition magnitude and direction. The time lag was applied to account for the propagation of the change in inlet boundary condition to the airfoil.

By comparison with experimental results for a steady freestream case, significant differences were found between the quantitative data and qualitative behaviour of the steady and variable freestream cases. Quantitatively, significant increases in peak lift, drag and pitching moment were observed, as were changes in aerodynamic damping. The aerodynamic loads were significantly different at angles of attack both above and below the static stall angle. Below the static stall angle, drag was greater, lift was reduced on the upstroke and increased on the downstroke, and pitching moment was similar. Above the static stall angle, drag and lift were generally reduced on the upstroke, but significantly higher on the downstroke – higher even than the drag and lift on the upstroke, which is the reverse of the relationship for the steady freestream drag and lift. Peak lift and drag were increased by 127% and 108%, respectively, and were delayed to later in the azimuth compared to the steady freestream data. Especially notable was that peak lift was delayed to the downstroke, where the literature review suggested that even in deep stall conditions the lift stall occurs at the maximum angle of attack. The data for pitching moment diverged from the steady freestream results, with significantly higher pitching moment on the upstroke, even reversing in sign from the steady freestream data, and significantly lower pitching moment on the downstroke, less than the upstroke data which is different that the relationship between up- and down-stroke pitching moment

steady freestream data. The peak negative pitching moment decreased by 286% compared to the steady freestream case and occurred at the maximum angle of attack, later in the azimuth than the steady freestream case.

Qualitatively, while some features of dynamic stall remained unchanged, many changes in the dynamic stall mechanism were observed throughout the pitch cycle. Fundamentally, the moment stall still preceded the lift stall, there were significant overshoots in aerodynamic loads over static airfoil data and dynamic stall was defined by the presence of large vortical structures. The notable differences due to the application of the variable freestream were observed throughout the pitch cycle. Below the static stall angle, the presence of a shock wave and resultant shock-induced separation prevented boundary layer reattachment from taking place. Above the static stall angle of attack, the trailing edge vortex rather than the leading edge vortex was the dominant feature and generated a large region of reverse flow around the airfoil. The LEV and TEV both formed later and dissipated earlier in the variable freestream case, and they were both stronger than their steady freestream counterparts as well. It is clear that the variable freestream not only brings about behaviour that is consistent with high and low Mach and Reynolds numbers and reduced frequency at the extremes of the pitch range, but that new changes to the overall mechanism are also introduced.

Therefore, the significant differences between steady and variable freestream modelling suggest that the time-varying nature of the freestream velocity is an important factor to model correctly in any dynamic stall experiment or simulation. These differences also suggest that variable freestream effects are indeed important, and

therefore there is a need for new empirical models which take into account variable freestream effects.

## 5.2 Recommendations for Future Work

The conclusions of this research suggest additional investigation that could be carried out to develop the body of knowledge of dynamic stall further. These involve higher-fidelity validation and an extension to flow control.

The validation carried out on the steady freestream reference case suggest that the results are accurate when extended by the addition of a variable freestream. However, it is generally preferred to validate numerical results directly against experimental data. Therefore, experimental modelling of the test case executed in this research could be carried out to validate the conclusions further. However it is acknowledged, as supported by the statement from Leishman in the introduction, that experimental modelling of this type of case has yet to be carried out due to the practical difficulties of these conditions.

Numerically, the research conducted above did not consider boundary layer transition modelling due to the limitations of the software used, the addition of which would increase solution fidelity. A far greater region of separated flow was observed, especially on the upstroke, which was not suspected to have been caused by the inlet boundary condition at the top of the domain, though this could be verified by changing the boundary condition. Given the difficulty of turbulence modelling in URANS simulations to accurately model separated flow, LES or DNS simulations could be carried out to

confirm the results obtained through this research. The complexity of the model could be increased to more closely resemble a complete helicopter by conducting a three-dimensional simulation to consider the influence of the three-dimensional effects discussed in the literature review. An aeroelastic model which considers the motion due to the structural response of the rotor blade to aerodynamic loads would also assist improving the modelling of reality. Modelling the complete set of rotors or the helicopter as a whole would also improve accuracy by considering time-history effects from one blade to another and the influence of the helicopter wake and blade-vortex interaction. It was also discussed above that the sinusoidal motion pattern applied to the angle of attack is a commonly used simplification of true rotor blade motion, and the solution could resemble reality more closely if the true motion schedule were to be applied. Further analysis of the impact of the variable freestream on aerodynamic damping could also be carried out.

A significant portion of dynamic stall research is dedicated to controlling its effects to maximize the favourable additional lift while minimizing the pitching moment peak that is damaging to the helicopter structure. The author is not aware of any research at this time which has combined motion control techniques with the application of variable magnitude freestream speed conditions. Such a combination to simulations of various flow control devices would evaluate their effectiveness in conditions more closely resembling the actual flight regime in which dynamic stall effects are most pronounced, and improve the design and testing of these concepts as they approach the maturity for flight testing.

## References

- Ahmadi, S. A., Sharif, S. and Jamshidi, R. (2009), “A Numerical Investigation on the Dynamic Stall of a Wind Turbine Section Using Different Turbulence Models,” *World Academy of Science, Engineering and Technology*, **34**, pp. 290-296.
- AIAA, (1998), *Guide for the Verification and Validation of Computational Fluid Dynamics Simulations*, AIAA G-077-1998, United States of America.
- Amiralaei, M. R., Alighanbari, H. and Hashemi, S. M. (2010), “An investigation into the effects of unsteady parameters on the aerodynamics of a low Reynolds number pitching airfoil,” *Journal of Fluids and Structures*, **26**, pp. 979-993.
- Bah, E. A. A., Sankar, L. N. and Jagoda, J. (2013), “Investigations on the Use of Multi-Element Airfoils for Improving Vertical Axis Wind Turbine Performance,” 51<sup>st</sup> AIAA Aerospace Sciences Meeting, AIAA 2013-1109, Grapevine, Texas.

- Bardina, J. E., Huang, P. G. and Coakley, T. J. (1997), "Turbulence Modeling Validation, Testing, and Development," NASA Technical Memorandum 110446.
- Barla, C., Geissler, W., Berton, E., Raffel, M. and Favier, D. (2005) "Dynamic Stall Investigations on NACA0012 and OA209 Airfoils," 31st European Rotorcraft Forum, Florence.
- Bousman, W. G. (1998), "A Qualitative Examination of Dynamic Stall from Flight Test Data," *Journal of the American Helicopter Society*, **43**(4), pp. 279-295.
- Bousman, W. G. (2000), "Airfoil Dynamic Stall and Rotorcraft Maneuverability," NASA TM 2000-209601.
- Bowles, P. O., Coleman, D. G., Corke, T. C., Thomas, H. O., and Wasikowskim, M. (2012), "Compressibility Effects on Aerodynamic Damping During Dynamic Stall Effects," *American Helicopter Society 68<sup>th</sup> Annual Forum*, Fort Worth, Texas, pp. 246-264.
- Bredberg, J. (2000), "On the Wall Boundary Condition for Turbulence Models," Internal Report 00/4, Department of Thermo and Fluid Dynamics, Chalmers University of Technology, Göteborg, Sweden.

- Brendel, M. and Mueller, T. J. (1987), "Features of Transitional Separation Bubbles in an Oscillating Freestream", Forum on Unsteady Flow Separation, Presented at 1987 ASME Applied Mechanics, Bioengineering and Fluids Engineering Conference, FED **52**, pp. 191-197.
- Carr, L. W., McAlister, K. W., McCroskey, W. J. (1977), "Analysis of the Development of Dynamic Stall Based on Oscillating Airfoil Experiments," NASA TN D-8382.
- Carr, L. W., Chandrasekhara, M. S. (1996), "Compressibility Effects on Dynamic Stall", Progress in Aerospace Sciences, **32**(6), pp. 523-573.
- Carta, F. O. (1967), "An Analysis of the Stall Flutter Instability of Helicopter Rotor Blades," American Helicopter Society 23<sup>rd</sup> Annual National Forum, Washington, D.C., pp. 1-18.
- Carta, F. O. (1971), "Effect of Unsteady Pressure Gradient Reduction on Dynamic Stall Delay," Journal of Aircraft, **8**(10), pp. 839-841.
- Carta, F. O. (1979), "A Comparison of the Pitching and Plunging Response of an Oscillating Airfoil," NASA Contractor Report 3172.
- Cesnik, C. E. S., Opoku, D. G., Nitzsche, F., Cheng, T. (2004), "Active twist rotor blade modelling using particle-wake aerodynamics and geometrically exact beam structural dynamics," Journal of Fluids and Structures, 19, pp.651-668.

- Chandrasekhara, M. S. and Carr, L. W. (1990), "Flow Visualization Studies of the Mach Number Effects on Dynamic Stall of an Oscillating Airfoil", *Journal of Aircraft*, **27**(6), pp. 516-522.
- Chandrasekhara, M. S. and Carr, L. W. (1995), "Compressibility Effects on Dynamic Stall of Oscillating Airfoils", *AGARD CP-552 Aerodynamics and Aeroacoustics of Rotorcraft*, pp. 3-1 – 3-15.
- Chopra, I. (2010), "Novel Design of a Medium-Sized Helicopter," Presentation at Carleton University.
- Dai, J. C., Hu, Y. P., Liu, D. S, Long, X. (2011), "Aerodynamic loads calculation and analysis for large scale wind turbine based on combining BEM modified theory with dynamic stall model," *Renewable Energy*, 36, pp. 1095-1104.
- Davis, L. G. (2006), "Trailing Edge Flap Control of Dynamic Stall on Helicopter Rotor Blades," Master of Applied Science Thesis, Carleton University, Ottawa, Canada.
- Ekaterinaris, J., Menter, F. (1994), "Computation of Oscillating Aifoil Flows with One- and Two-Equation Turbulence models," *AIAA Journal*, **32**(12), pp. 2359-2365.
- El Akoury, R., Braza, M., Hoarau, Y., Vos, J., Harran, G., Sevrain, A. (2009), "Unsteady Flow Around a NACA0021 Airfoil Beyond Stall at 60° Angle of Attack," *IUTAM Symposium on Unsteady Separated Flows and Their Control*, IUTAM Bookseries 14.

- Ellsworth, R. H., Mueller, T. J. (1991), "Airfoil boundary layer measurements at low Re in an accelerating flow from a nonzero velocity", *Experiments in Fluids*, **11**, pp. 368-374.
- Ericsson, L. E., Reding, J. P. (1972), "Dynamic Stall of Helicopter Blades," *Journal of the American Helicopter Society*, **17**(1), pp. 11-19.
- Ericsson, L. E., Reding, J. P. (1988), "Fluid Mechanics of Dynamic Stall Part 1. Unsteady Flow Concepts," *Journal of Fluids and Structures*, **2**, pp. 1-33.
- Esch, T., Menter, F. R. (2003), "Heat Transfer Predictions Based on Two-Equation Turbulence Models with Advanced Wall Treatment," *Turbulence*, in *Proc. Heat and Mass Transfer 4*, Eds. Hanjalic, Nagano, Tummers, Antalya, pp. 633-640.
- FAA (2008), "Aviation Maintenance Technician Handbook," FAA-H-8083-30, U. S. Department of Transportation, Federal Aviation Administration, Airmen Testing Standards Branch, Oklahoma City, OK.
- Favier, D., Agnes, A., Barbi, C., Maresca, C. (1988), "Combined Translation/Pitch Motion: A New Airfoil Dynamic Stall Simulation," *Journal of Aircraft*, **25**(9), pp. 805-814.
- Favier, D., Belleudy, J., Maresca, C. (1992), "Influence of Coupling Incidence and Velocity Variations on the Airfoil Dynamic Stall," *AHS 48th Annual Forum*, Washington DC, pp. 1385-1407.

- Feszty, D., Gillies, E., Vezza, M. (2004), "Alleviation of Airfoil Dynamic Stall Moments via Trailing-Edge-Flap Flow Control," *AIAA Journal*, **42**(1), pp. 17-25
- Fluent Inc. (2001), *Fluent 6.0 User's Guide*, Fluent Inc., New Hampshire.
- Foresman, J. L. (1974), "Turbulent Boundary Layer Separation Characteristics with Blowing in an Oscillating Flow", Master thesis, Naval Postgraduate School.
- Francis, M. S. and Keesee, J. E. (1985), "Airfoil Dynamic Stall Performance with Large-Amplitude Motions," *AIAA Journal*, **23**(11), pp. 1653-1659.
- Gagnon, L., Richard, M. J. and Lévesque, B. (2011), "Simulation of a Rotating Device that Reduces the Aerodynamic Drag of an Automobile," *Transactions of the Canadian Society for Mechanical Engineering*, **35**(2), pp. 229-249.
- Galbraith, R. A. McD., Niven, A. J., and Seto, L. Y. (1986), "On the Duration of Low Speed Dynamic Stall," 15<sup>th</sup> Congress of the International Council of the Aeronautical Sciences, pp. 522-531.
- Gao, L., Xu, J. and Gao, G. (2012), "Numerical Simulation of Turbulent Flow past Airfoils on OpenFOAM," *Procedia Engineering*, **31**, pp. 756-761.
- Gardner, A. D. (2012), "Influence of rotation on dynamic stall," 68th American Helicopter Society International Annual Forum 2012: Fort Worth, Texas, USA, pp. 464-474.

- Geissler, W., Dietz, G., Mai, H. (2005), "Dynamic Stall on a Supercritical Airfoil," *Aerospace Science and Technology*, 9, pp. 390-399.
- Gerontakos, P. (2008), "Unsteady Airfoil Flow Control via a Dynamically Deflected Trailing-Edge Flap, Ph.D. Dissertation," Department of Mechanical Engineering, McGill University, Montreal, Canada.
- Gharali, K., Johnson, D. A. (2012), "Numerical modeling of an S809 airfoil under dynamic stall, erosion and high reduced frequencies", *Applied Energy*, **93**, pp. 45-52.
- Gharali, K. and Johnson, D. A. (2013), "Dynamic stall simulation of a pitching airfoil under unsteady freestream velocity", *Journal of Fluids and Structures*, **42**, pp. 228-244.
- Glauert, H. (1935), "Airplane Propellers," in Division L of *Aerodynamic Theory*, edited by Durand, W. F., Springer Verlag, Berlin, Germany.
- Gompertz, K., Jensen, C., Kumar, P., Peng, D., Gregory, J. W., Bons, J. P. (2011), "Modification of Transonic Blowdown Wind Tunnel to Produce Oscillating Freestream Mach Number," *AIAA Journal*, **49**(11), pp. 2555-2563.

- Gompertz, K., Jensen, C. D., Gregory, J. W., Bons, J. P., “Compressible dynamic stall mechanisms due to airfoil pitching and freestream mach oscillations,” 68th American Helicopter Society International Annual Forum 2012: Fort Worth, Texas, USA, pp. 266-284.
- Green, R. B., Galbraith, R. A. McD. (1995), “Dynamic Recovery to Fully Attached Aerofoil Flow from Deep Stall”, AIAA Journal, **33**(8), pp. 1433-1440.
- Greenshields, C. J., Weller, H. G., Gasparini, L., Reese, J. M. (2010), “Implementation of semi-discrete, non-staggered central schemes in a colocated, polyhedral, finite volume framework, for high-speed viscous flows,” International Journal for Numerical Methods in Fluids, 63, pp. 1-21.
- Henderson, A. (2007), “ParaView Guide, A Parallel Visualization Application,” Kitware Inc.
- Isaacs, N. C. G. And Harrison, R. J. (1989), “Identification of Retreating Blade Stall Mechanisms using Flight Test Pressure Measurements,” 45<sup>th</sup> Annual National Forum of the American Helicopter Society, pp. 265-279.
- Jensen, C. D., Gompertz, K. A., Peng, D., Juliano, T. J., Kumar, P., Gregory, J. W., Bons, J. P. (2011), “Unsteady Compressible Flow on a NACA 0021 Airfoil,” AIAA 2011-670, 49th AIAA Aerospace Sciences Meeting including the New Horizons Forum and Aerospace Exposition.

- Johnson, W. (1998), "Rotorcraft Aerodynamics Models for a Comprehensive Analysis," American Helicopter Society 54<sup>th</sup> Annual Forum, Washington, DC, May 20-22.
- Jose, A. I., Leishman, J. G., Baeder, J. D. (2006), "Unsteady Aerodynamic Modeling with Time-Varying Free-Stream Mach Numbers," *Journal of the American Helicopter Society* **51**(4), pp. 299-318.
- Jumper, E. J., Schreck, S. J., Dimmick, R. L. (1987), "Lift-Curve Characteristics for an Airfoil Pitching at Constant Rate," *Journal of Aircraft*, **24**(10), pp. 680-687.
- Jumper, E. J., Dimmick, R. L., and Allaire, A. J. S. (1989), "The Effect of Pitch Location on Dynamic Stall," *Journal of Fluids Engineering*, **111**, pp. 256-262.
- Kerho, M. (2007), "Adaptive Airfoil Dynamic Stall Control," *Journal of Aircraft*, **44**(4), pp. 1350-1360.
- Kerstens, W., Williams, D. R. (2012), "Energy exchange measurements with a longitudinally oscillating flow and a vertically oscillating wing," AIAA 2012-1082, 50th AIAA Aerospace Sciences Meeting including the New Horizons Forum and Aerospace Exposition, Nashville, Tennessee.
- Ko, S., McCroskey, W. J. (1997), "Computations of Unsteady Separating Flows over an Oscillating Airfoil," *AIAA Journal*, **35**(7), pp. 1235-1238.

- Kurganov, A. and Tadmor, E. (2000), "New High-Resolution Central Schemes for Nonlinear Conservation Laws and Convection-Diffusion Equations," *Journal of Computational Physics*, **160**, pp.241-282.
- Ladson, C. L., Hill, A. S., Johnson W. G. Jr., (1987), "Pressure Distributions from High Reynolds Number Transonic Tests of an NACA 0012 Airfoil in the Langley 0.3-Meter Transonic Cryogenic Tunnel," NACA TM 100526.
- Ladson, C. L. (1988), "Effects of Independent Variation of Mach and Reynolds Numbers on the Low-Speed Aerodynamic Characteristics of the NACA 0012 Airfoil Section," NASA TM 4074.
- Lakey, S. P., Sangolola, B. A. (2007), "Aerodynamic Analysis of Oscillating Aerofoils, including Dynamic Stall, using Commercial CFD Software," 7<sup>th</sup> AIAA Aviation Technology, Integration and Operations Conference, Belfast, Northern Ireland.
- Laney, C. B. (1998), *Computational Gasdynamics*, Cambridge University Press, New York.
- Lee, T., Gerontakos, P. (2004), "Investigation of flow over an oscillating airfoil," *Journal of Fluid Mechanics*, **512**, pp 313-341.
- Leishman, J. G., Beddoes, T. S. (1989), "A semi-empirical model for dynamic stall," *Journal of the American Helicopter Society*, **34**(3), pp. 3-17.

- Leishman, J. G. (2006), *Principles of Helicopter Aerodynamics*, 2<sup>nd</sup> Edition, Cambridge University Press, New York.
- Lorber, P. F., Carta, F. O. (1987), "Airfoil Dynamic Stall at Constant Pitch Rate and High Reynolds Number", AIAA 19<sup>th</sup> Fluid Dynamics, Plasma Dynamics and Lasers Conference, AIAA-87-1329, Honolulu, Hawaii.
- Maresca, C. A., Favier, D. J., Rebont, J. M. (1981), "Unsteady Aerodynamics of An Aerofoil At High Angle Of Incidence Performing Various Linear Oscillations In A Uniform Stream," *Journal of the American Helicopter Society*, **26**(2), pp. 40-45.
- Martin, J. M., Empey, R. W., McCroskey, W. J., and Caradonna, F. X. (1974), "An Experimental Analysis of Dynamic Stall on an Oscillating Airfoil," *Journal of the American Helicopter Society*, **19**(1), pp. 26-32.
- Martinat, G., Braza, M., Harran, G., Sevrain, A., Tzabiras, G., Hoarau, Y., Favier, D. (2009), "Dynamic Stall of a Pitching and Horizontally Oscillating Airfoil," *IUTAM Symposium on Unsteady Separated Flows and their Control*, IUTAM Bookseries 14, pp. 395-403.
- McAlister, K. W., Carr, L. W., and McCroskey, L. W. (1978), "Dynamic Stall Experiments on the NACA 0012 Airfoil," *NASA Technical Paper 1100*.

- McAlister, K. W., Pucci, S. L., McCroskey, W. J., Carr, L. W. (1982), "An Experimental Study of Dynamic Stall on Advanced Airfoil Sections Volume 2. Pressure and Force Data," NASA Technical Memorandum 84245.
- McAlister, K. W., Lambert, O., Petot, D. (1984), "Application of the ONERA Model of Dynamic Stall," NASA TP 2399.
- McCroskey, W. J. and Fisher, R. K. Jr. (1972), "Detailed Aerodynamic Measurements on a Model Rotor in the Blade Stall Regime," *Journal of the American Helicopter Society*, **17**(1), pp. 20-30.
- McCroskey, W. J. (1973), "Inviscid Flowfield of an Unsteady Airfoil," *AIAA Journal*, **11**(8), pp. 1130-1137.
- McCroskey, W. J., Philippe, J. J. (1975), "Unsteady Viscous Flow on Oscillating Airfoils," *AIAA Journal*, **13**, pp. 71-79.
- McCroskey, W.J., Carr, L.W., McAlister, K.W. (1976), "Dynamic Stall Experiments on Oscillating Airfoils," *AIAA Journal*, **14**(1), pp. 57-83.
- McCroskey, W. J. (1982), "Unsteady Airfoils," *Ann. Rev. Fluid Mech.*, **14**, pp. 285-311.
- McCroskey, W. J., Pucci, S. L. (1982), "Viscous-Inviscid Interaction on Oscillating Airfoils in Subsonic Flow", *AIAA Journal*, **20**(2), pp. 167-174.
- McCullough, G. B., Gault, D. E. (1951), "Examples of Three Representative Types of Airfoil-Section Stall at Low Speed", NACA TN 2502.

- McHugh, F. J. (1978), "What Are The Lift and Propulsive Force Limits At High Speed For The Conventional Rotor?" 34<sup>th</sup> Annual Forum of the American Helicopter Society, pp. 1-12.
- Menter, F. (1994), "Two-equation eddy-viscosity turbulence models for engineering applications," *AIAA Journal*, **32**(8), pp. 1598-1605.
- Menter, F. and Esch, T. (2001), "Elements of Industrial Heat Transfer Predictions," 16<sup>th</sup> Brazilian Congress of Mechanical Engineering (COBEM), Uberlandia, Brazil, pp. 117-127.
- Menter, F., Carregal Ferreira, J., Esch, T., and Konno, B. (2003), "The SST Turbulence Model with Improved Wall Treatment for Heat Transfer Predictions in Gas Turbines," Proceedings of the International Gas Turbine Congress 2003, Tokyo, IGTC2003-TS-059.
- Mulleners, K. and Raffel, M. (2012), "The onset of dynamic stall revisited", *Exp Fluids*, **52**, pp. 779-793.
- Nakao, S., Kashitani, M., Miyaguna, T. and Yamaguchi, Y. (2014), "A Study on High Subsonic Airfoil Flows in Relatively High Reynolds Number by Using OpenFOAM," *Journal of Thermal Science*, **23**(2), pp. 133-137.
- OpenFOAM: The Open Source CFD Toolbox Programmer's Guide Version 2.3.0 (2014), OpenFOAM Foundation.

- OpenFOAM: The Open Source CFD Toolbox User Guide Version 2.3.0 (2014), OpenFOAM Foundation.
- Panda, J. and Zaman, K. B. M. Q. (1994), "Experimental investigation of the flow field of an oscillating airfoil and estimation of lift from wake surveys", *J. Fluid Mech.*, **265**, pp. 65-96.
- Pascaglia, F., Montorfano, A. and Onorati, A. (2013), "Development of a non-reflecting boundary condition for multidimensional nonlinear duct acoustic computation," *Journal of Sound and Vibration*, **332**, pp. 922-935.
- Pascazio, M. (1995), "Contribution expérimentale et numérique à l'étude de la couche limite se développant sur un profil d'aile en oscillation : phénomènes de transition et de décollement en écoulement instationnaire", PhD Thesis, Université de la méditerranée.
- Pellegrini, F. (2012), "Scotch and LibScotch 6.0 User's Guide."
- Perry, F. J. (1987), "Aerodynamics of the Helicopter World Speed Record," 43<sup>rd</sup> Annual National Forum of the American Helicopter Society, pp. 3-15.
- Pierce, G. A., Kunz, D. L., Malone, J. B. (1978), "Effect of varying freestream velocity on airfoil dynamic stall characteristics," *Journal of the American Helicopter Society*, **23**(2), pp 27-33.

- Poinsot, T. J. Lele, S. K. (1992), "Boundary Conditions for Direct Simulations of Compressible Viscous Flows," *Journal of Computational Physics*, **101**, pp. 104-129.
- Pope, S. (2000), *Turbulent Flows*, Cambridge University Press, New York.
- Reynolds, O. (1883), "An Experimental Investigation of the Circumstances Which Determine Whether the Motion of Water Shall Be Direct or Sinuous, and the Law of Resistance in Parallel Channels", *Philosophical Transactions of the Royal Society of London*, **174**, pp. 935-982.
- Saxena, L. S., Fejer, A. A. and Morkovin, M. V. (1978), "Features of Unsteady. Flows over Airfoils," AGARD CP-227, pp. 22-1 – 22-11.
- Schlichting, H. (1979), *Boundary Layer Theory*, 7<sup>th</sup> Ed., McGraw-Hill, Inc., United States of America.
- Schreck, S. J., Helin, H. E. (1994), "Unsteady Vortex Dynamics and Surface Pressure Topologies on a Finite Pitching Wing", *Journal of Aircraft*, **31**(4), pp. 899-907.
- Sharma, D. M. and Poddar, K. (2010), "Experimental Investigations of Laminar Separation Bubble for a Flow Past an Airfoil," *Proceedings of ASME Turbo Expo 2010: Power for Land, Sea and Air*, Glasgow, UK.

- Shi, Z. And Ming, X. (2008), "Effects of Unsteady Freestream on Aerodynamic Characteristics of Pitching Delta Wing," *Journal of Aircraft*, **45**(11), pp. 2182-2185.
- Shi, Z. And Ming, X. (2009), "Experimental Investigation on a Pitching Motion Delta Wing in Unsteady Freestream," *Modern Physics Letters B.*, **23**(3), pp. 409-412.
- Somers, D.M. (1997), "Design and Experimental Results for the S805 Airfoil," National Renewable Energy Laboratory, NREL/SR-440-6917.
- Spentzos, A., Barakos, G., Baddock, K., Richards, B. (2005), "Investigation of Three-Dimensional Stall Using Computational Fluid Dynamics," *AIAA Journal*, **43**(5), 1023-1033.
- Sumner, J. and Masson, C. (2012), "k- $\epsilon$  simulations of the neutral atmospheric boundary layer: analysis and correction of discretization errors on practical grids," *International Journal for Numerical Methods in Fluids*, **70**, pp. 724-741.
- Sutherland, W. (1893), "The Viscosity of Gases and the Molecular Force," *The London, Edinburgh and Dublin philosophical magazine and journal of science series 5*, **36**(223), pp. 507-531.
- Theodorsen, T. (1934), "General Theory of Aerodynamic Instability and the Mechanism of Flutter," NACA Report 496.

- Tran, C. T., Petot, D. (1981), "Semi-Empirical Model for the Dynamic Stall of Airfoils in View of the Application to the Calculation of Responses of a Helicopter Blade in Forward Flight," *Vertica*, 5, pp. 35-53.
- Versteeg, H. K., Malalasekera, W. (2007), *An Introduction to Computational Fluid Dynamics: The Finite Volume Method*, Second Edition, Bell & Blain Limited, Glasgow.
- Visbal, M. R., Shang, J. S. (1989), "Investigation of the Flow Structure Around a Rapidly Pitching Airfoil," *AIAA Journal*, 27(8), pp. 1044-1051.
- Ward, J. W. (1963), "The Behaviour and Effects of Laminar Separation Bubbles on Aerofoils in Incompressible Flow," *Journal of the Royal Aeronautical Society*, 67, pp. 783-790.
- Watrln, D., Dimitriadis, G., Perry, T. and Smith, M. J. (2012), "Computational Considerations for the Prediction of Stall Flutter," 53<sup>rd</sup> AIAA/ASME/ASCE/AHS/ASC Structures, Structural Dynamics and Materials Conference, AIAA 2012-1706, Honolulu, Hawaii.
- Wilcox, D. C. (1994), *Turbulence Modeling for CFD*, 1<sup>st</sup> ed., DCW Industries, Inc, California.

- 
- Wong, J. G., Mohebbian, A., Kriesgseis, J., Rival, D. E. (2013), “Rapid Flow Separation for Transient Inflow Conditions Versus Accelerating Bodies: An Investigation into Their Equivalency”, *Journal of Fluids and Structures*, **40**, pp. 257-268.

## **Appendix A**

### **OpenFOAM Input Files**

The following files, listed in Table A.1, fully define the variable freestream OpenFOAM 2.3.0 case when used with the “blockMeshDoubleGrading” contribution from the OpenFOAM community, available on the OpenFOAM wiki. The contents of these files are in the sections that follow. Note that the complete contents of the “blockMeshDict” file are not shown as the file is extremely large due to the definition of many splines which form the curved patches of the mesh; the ellipsis is used to indicate where lines were removed. The vin.dat file is also very large; the first 50 lines are shown here to illustrate the concept, without the complete file.

**Table A.1:** List of files and folder structure for the variable freestream OpenFOAM case.

<b>Directory Name File Name</b>	<b>File Contents</b>
\ vin.dat	Time-dependent inlet airspeed boundary condition
\0  k omega mut p T U rho	Initial and boundary conditions for:  Turbulent kinetic energy Turbulent dissipation rate Eddy viscosity Pressure Temperature Velocity Density
\constant  RASProperties thermodynamicProperties thermophysicalProperties transportProperties turbulenceProperties	Turbulence model and associated parameter selection Definition of thermodynamic properties Definition of thermophysical properties Definition of transport properties Selection of laminar/URANS/LES simulation
\constant\polyMesh  blockMeshDict	Definition of mesh for use with “blockMesh” mesh generator
\system  controlDict decomposeParDict fvSchemes fvSolution sampleDict	Control of time, reading and writing data Parameters controlling mesh decomposition Discretization schemes definition Equation solvers, residual tolerances defined Identification of sampling locations and parameters for post-processing

## A.1 Contents of File vin.dat

```

( //Time  Ux      Uy      Uz      AlphaIn  SpeedIn  AzimuthIn
(0.000000 (157.720233 42.261009 0.000000) // 15.000000 163.284000 180.000000
(0.000197 (157.054701 42.267331 0.000000) // 15.062832 162.642880 180.360005
(0.000394 (156.389372 42.272245 0.000000) // 15.125662 162.001785 180.720011
5 (0.000591 (155.724274 42.275750 0.000000) // 15.188487 161.360741 181.080016
(0.000788 (155.059437 42.277848 0.000000) // 15.251305 160.719773 181.440021
(0.000985 (154.394887 42.278538 0.000000) // 15.314112 160.078905 181.800026
(0.001182 (153.730654 42.277823 0.000000) // 15.376907 159.438165 182.160032
(0.001379 (153.066766 42.275704 0.000000) // 15.439688 158.797576 182.520037
10 (0.001576 (152.403252 42.272182 0.000000) // 15.502451 158.157164 182.880042
(0.001773 (151.740139 42.267259 0.000000) // 15.565194 157.516955 183.240047
(0.001970 (151.077457 42.260937 0.000000) // 15.627914 156.876973 183.600053
(0.002167 (150.415232 42.253218 0.000000) // 15.690610 156.237244 183.960058
(0.002364 (149.753494 42.244106 0.000000) // 15.753279 155.597793 184.320063
15 (0.002561 (149.092270 42.233601 0.000000) // 15.815918 154.958646 184.680068
(0.002758 (148.431588 42.221708 0.000000) // 15.878525 154.319827 185.040074
(0.002955 (147.771477 42.208430 0.000000) // 15.941097 153.681362 185.400079
(0.003152 (147.111965 42.193769 0.000000) // 16.003632 153.043276 185.760084
(0.003349 (146.453078 42.177730 0.000000) // 16.066127 152.405594 186.120089
20 (0.003546 (145.794846 42.160316 0.000000) // 16.128580 151.768341 186.480095
(0.003743 (145.137296 42.141531 0.000000) // 16.190989 151.131543 186.840100
(0.003940 (144.480456 42.121379 0.000000) // 16.253351 150.495225 187.200105
(0.004137 (143.824353 42.099866 0.000000) // 16.315663 149.859411 187.560111
(0.004334 (143.169014 42.076995 0.000000) // 16.377923 149.224127 187.920116
25 (0.004531 (142.514468 42.052772 0.000000) // 16.440129 148.589398 188.280121
(0.004728 (141.860742 42.027201 0.000000) // 16.502278 147.955249 188.640126
(0.004925 (141.207863 42.000287 0.000000) // 16.564367 147.321705 189.000132
(0.005122 (140.555859 41.972038 0.000000) // 16.626395 146.688791 189.360137
(0.005319 (139.904757 41.942457 0.000000) // 16.688359 146.056532 189.720142
30 (0.005516 (139.254583 41.911551 0.000000) // 16.750256 145.424953 190.080147
(0.005713 (138.605365 41.879326 0.000000) // 16.812084 144.794079 190.440153
(0.005910 (137.957131 41.845789 0.000000) // 16.873840 144.163934 190.800158
(0.006107 (137.309906 41.810945 0.000000) // 16.935523 143.534544 191.160163
(0.006304 (136.663718 41.774803 0.000000) // 16.997129 142.905934 191.520168
35 (0.006501 (136.018594 41.737368 0.000000) // 17.058656 142.278128 191.880174
(0.006698 (135.374559 41.698648 0.000000) // 17.120102 141.651151 192.240179
(0.006895 (134.731642 41.658650 0.000000) // 17.181464 141.025027 192.600184
(0.007092 (134.089867 41.617382 0.000000) // 17.242740 140.399783 192.960189
(0.007289 (133.449262 41.574852 0.000000) // 17.303927 139.775441 193.320195
40 (0.007486 (132.809853 41.531067 0.000000) // 17.365024 139.152027 193.680200
(0.007683 (132.171667 41.486035 0.000000) // 17.426027 138.529566 194.040205
(0.007880 (131.534728 41.439766 0.000000) // 17.486934 137.908081 194.400211
(0.008077 (130.899064 41.392268 0.000000) // 17.547744 137.287599 194.760216
(0.008274 (130.264700 41.343548 0.000000) // 17.608452 136.668142 195.120221
45 (0.008471 (129.631662 41.293617 0.000000) // 17.669058 136.049735 195.480226
(0.008668 (128.999975 41.242483 0.000000) // 17.729558 135.432404 195.840232
(0.008865 (128.369666 41.190156 0.000000) // 17.789951 134.816172 196.200237
(0.009062 (127.740760 41.136645 0.000000) // 17.850233 134.201063 196.560242
(0.009259 (127.113282 41.081960 0.000000) // 17.910403 133.587102 196.920247
50 (0.009456 (126.487257 41.026110 0.000000) // 17.970458 132.974313 197.280253

```

## A.2 Contents of File \0\k

```

/*-----*- C++ -*-----*\
|=====|
| \\      / F i e l d      | OpenFOAM: The Open Source CFD Toolbox
| \\      / O p e r a t i o n | Version: 2.3.0
5 | \\      / A n d           | Web:      www.OpenFOAM.org
| \\      / M a n i p u l a t i o n |
\*-----*-
FoamFile
{
10   version      2.0;
    format        ascii;
    class         volScalarField;
    location      "0";
    object        k;
15 }
// *****

dimensions      [0 2 -2 0 0 0 0];

20 internalField  uniform 1.5;

boundaryField
{
25   inlet
    {
        type          fixedValue;
        value          uniform 1.5;
    }
    topAndBottom
30   {
        type          fixedValue;
        value          uniform 1.5;
    }
    outlet
35   {
        type          zeroGradient;
    }
    wing
40   {
        type          compressible::kqRWallFunction;
        value          uniform 1.5;
    }
    frontAndBack
45   {
        type          empty;
    }
}

// *****

```

### A.3 Contents of File \0\omega

```

/*-----*- C++ -*-----*\
|=====|
|  \ \ /  F i e l d      | OpenFOAM: The Open Source CFD Toolbox |
|  \ \ /  O p e r a t i o n | Version: 2.3.0 |
5 |  \ \ /  A n d           | Web:      www.OpenFOAM.org |
|  \ \ /  M a n i p u l a t i o n |
\*-----*-
FoamFile
{
10   version      2.0;
    format       ascii;
    class        volScalarField;
    location     "0";
    object       omega;
15 }
// *****

dimensions      [0 0 -1 0 0 0 0];

20 internalField  uniform 52.074;

boundaryField
{
25   inlet
    {
        type          fixedValue;
        value          uniform 52.074;
    }
    topAndBottom
30   {
        type          fixedValue;
        value          uniform 52.074;
    }
    outlet
35   {
        type          zeroGradient;
    }
    wing
40   {
        type          compressible::omegaWallFunction;
        Cmu           0.09;
        kappa         0.41;
        E             9.8;
        beta1         0.075;
45   value          uniform 0.0035;
    }
    frontAndBack
    {
50   type          empty;
    }
}

// *****

```

## A.4 Contents of File \0\mut

```

/*-----*- C++ -*-----*\
|=====|
|  \ \   /  F i e l d      | OpenFOAM: The Open Source CFD Toolbox
|  \ \   /  O p e r a t i o n | Version:  2.3.0
5 |  \ \   /  A n d           | Web:      www.OpenFOAM.org
|  \ \   /  M a n i p u l a t i o n |
\*-----*- C++ -*-----*\
FoamFile
{
10   version      2.0;
    format       ascii;
    class        volScalarField;
    object       mut;
}
15 // ***** //

dimensions      [1 -1 -1 0 0 0 0];

internalField   uniform 0.14;

20 boundaryField
{
    "(inlet|topAndBottom)"
25   {
        type          calculated;
        value         uniform 0.14;
    }
    outlet
30   {
        type          calculated;
        value         uniform 0.14;
    }

    wing
35   {
        type          mutkWallFunction;
        Cmu           0.09;
        kappa         0.41;
        E             9.8;
40   value         uniform 0.14;
    }

    frontAndBack
45   {
        type          empty;
    }
}

// ***** //

```

## A.5 Contents of File \0\p

```

/*-----* C++ *-----*\
|=====|
|  \ \ /  F i e l d      | OpenFOAM: The Open Source CFD Toolbox
|  \ \ /  O p e r a t i o n | Version: 2.3.0
5 |  \ \ /  A n d           | Web:      www.OpenFOAM.org
|  \ \ /  M a n i p u l a t i o n |
\*-----*\
FoamFile
{
10   version      2.0;
     format      ascii;
     class       volScalarField;
     object      p;
}
15 // ***** //

dimensions      [1 -1 -2 0 0 0];

internalField   uniform 101325;

20 boundaryField
{
    "(inlet|topAndBottom)"
25   {
       type      zeroGradient;
   }

    outlet
30   {
       type      waveTransmissive;
       field     p;
       phi      phi;
       rho      rho;
       psi      thermo:psi;
35   gamma     1.4;
       fieldInf  101325;
       lInf     1;
       value     $internalField;
   }
40   wing
   {
       type      zeroGradient;
   }
45   frontAndBack
   {
       type      empty;
   }
50 }

// ***** //

```

## A.6 Contents of File \0\T

```

/*-----*- C++ -*-----*\
|=====|
| \ \ / F i e l d | OpenFOAM: The Open Source CFD Toolbox |
| \ \ / O p e r a t i o n | Version: 2.3.0 |
5 | \ \ / A n d | Web: www.OpenFOAM.org |
| \ \ / M a n i p u l a t i o n |
\*-----*\
FoamFile
{
10   version      2.0;
    format       ascii;
    class        volScalarField;
    object       T;
}
15 // ***** //

dimensions      [0 0 0 1 0 0 0];

internalField   uniform 288.0;
20
boundaryField
{
    "(inlet|topAndBottom)"
25   {
        type          inletOutlet;
        inletValue    uniform 288.0;
        value         uniform 288.0;
    }

30   outlet
    {
        type          zeroGradient;
    }

35   wing
    {
        type          zeroGradient;
    }

40   frontAndBack
    {
        type          empty;
    }
}
45 // ***** //

```

## A.7 Contents of File \0\U

```

/*-----* C++ *-----*\
|=====|
|  \ \ /  F i e l d      | OpenFOAM: The Open Source CFD Toolbox
|  \ \ /  O p e r a t i o n | Version: 2.3.0
5 |  \ \ /  A n d           | Web:      www.OpenFOAM.org
|  \ \ /  M a n i p u l a t i o n |
\*-----*\
FoamFile
{
10   version      2.0;
     format      ascii;
     class       volVectorField;
     object      U;
}
15 // ***** //

dimensions      [0 1 -1 0 0 0 0];

internalField   uniform (157.720233 42.261009 0);
20
boundaryField
{
    "(inlet|topAndBottom)"
25     {
        type      uniformFixedValue;
        uniformValue tableFile;
        tableFileCoeffs
        {
30             fileName      "vin.dat";
             outOfBounds    clamp;
        }
    }

    outlet
35     {
        type      zeroGradient;
    }

    wing
40     {
        type      fixedValue;
        value     uniform (0 0 0);
    }

    frontAndBack
45     {
        type      empty;
    }
}
50 // ***** //

```

## A.8 Contents of File \0\rho

```

/*-----*- C++ -*-----*\
|=====|
|  \ \   /  F i e l d      | OpenFOAM: The Open Source CFD Toolbox
|  \ \   /  O p e r a t i o n | Version:  2.3.0
5 |  \ \   /  A n d           | Web:      www.OpenFOAM.org
|  \ \   /  M a n i p u l a t i o n |
\*-----*-
FoamFile
{
10   version      2.0;
    format       ascii;
    class        volScalarField;
    object       rho;
}
15 // *****

dimensions      [1 -3 0 0 0 0 0];

internalField   uniform 1.225;

20 boundaryField
{
    "(inlet|topAndBottom)"
25   {
    type         fixedRho;
    value        $internalField;
    }

    outlet
30   {
    type         zeroGradient;
    }

    wing
35   {
    type         zeroGradient;
    }

    frontAndBack
40   {
    type         empty;
    }
}

45 // *****

```

## A.9 Contents of File \constant\RASProperties

```

/*-----*- C++ -*-----*\
|=====|
|  \ \ /  F i e l d      | OpenFOAM: The Open Source CFD Toolbox |
|  \ \ /  O p e r a t i o n | Version: 2.3.0 |
5 |  \ \ /  A n d           | Web: www.OpenFOAM.org |
|  \ \ /  M a n i p u l a t i o n |
/*-----*- C++ -*-----*\
FoamFile
{
10   version      2.0;
    format       ascii;
    class        dictionary;
    location     "constant";
15   object       RASProperties;
}
// *****

RASModel      kOmegaSST;

20 turbulence  on;

printCoeffs  on;

kOmegaSSTCoeffs
25 {
    alphaK1      0.85034;
    alphaK2      1;
    alphaOmega1  0.5;
    alphaOmega2  0.85616;
30   Prt         1;
    gamma1      0.5532;
    gamma2      0.4403;
    beta1       0.075;
    beta2       0.0828;
35   betaStar    0.09;
    a1          0.31;
    c1          10;
}

40 // *****

```

## A.10 Contents of File `\constant\thermodynamicProperties`

```

/*-----*- C++ -*-----*\
|=====|
|  \ \ /  F i e l d      | OpenFOAM: The Open Source CFD Toolbox
|  \ \ /  O p e r a t i o n | Version:  2.3.0
5 |  \ \ /  A n d           | Web:      www.OpenFOAM.org
|  \ \ /  M a n i p u l a t i o n |
\*-----*\
FoamFile
{
10   version      2.0;
    format       ascii;
    class        dictionary;
    location     "constant";
15   object       thermodynamicProperties;
}
// *****

20 Cv          Cv [ 0 2 -2 -1 0 0 0 ] 718.0;

R           R [ 0 2 -2 -1 0 0 0 ] 287;

// *****

```

## A.11 Contents of File `\constant\thermophysicalProperties`

```

/*-----* C++ *-----*\
|=====|
|  \ \ /  F i e l d      | OpenFOAM: The Open Source CFD Toolbox
|  \ \ /  O p e r a t i o n | Version:  2.3.0
5 |  \ \ /  A n d           | Web:      www.OpenFOAM.org
|  \ \ /  M a n i p u l a t i o n |
\*-----*\
FoamFile
{
10   version      2.0;
    format       ascii;
    class        dictionary;
    location     "constant";
    object       thermophysicalProperties;
15 }
// *****

thermoType
{
20   type          hePsiThermo;
    mixture       pureMixture;
    transport     sutherland;
    thermo        hConst;
    equationOfState perfectGas;
25   specie        specie;
    energy        sensibleEnthalpy;
}

mixture
30 {
    specie
    {
        nMoles      1;
        molWeight   28.9;
35   }
    thermodynamics
    {
        Cp      1005;
        Hf      50;
40   }
    transport
    {
        As      1.458e-06;
        Ts      110.4;
45   Pr      0.707;
    }
}

// *****

```

## A.12 Contents of File `\constant\transportProperties`

```

/*-----*- C++ -*-----*\
|=====|
|  \ \ /  F i e l d      | OpenFOAM: The Open Source CFD Toolbox
|  \ \ /  O p e r a t i o n | Version: 2.3.0
5 |  \ \ /  A n d           | Web:      www.OpenFOAM.org
|  \ \ /  M a n i p u l a t i o n |
\*-----*\
FoamFile
{
10   version      2.0;
    format        ascii;
    class         dictionary;
    location      "constant";
15   object       transportProperties;
}
// ***** //

transportModel Newtonian;

20 rho          rho [ 1 -3 0 0 0 0 ] 1.225;

nu           nu [ 0 2 -1 0 0 0 ] 1.477551e-05;

// ***** //

```

### A.13 Contents of File `\constant\turbulenceProperties`

```

/*-----* C++ *-----*\
|=====|
|  \ \ /  F i e l d      | OpenFOAM: The Open Source CFD Toolbox
|  \ \ /  O p e r a t i o n | Version: 2.3.0
5 |  \ \ /  A n d           | Web:      www.OpenFOAM.org
|  \ \ /  M a n i p u l a t i o n |
\*-----*/
FoamFile
{
10   version      2.0;
    format        ascii;
    class         dictionary;
    location      "constant";
15   object        turbulenceProperties;
}
// *****

simulationType  RASModel;

20 // *****

```

## A.14 Contents of File \constant\polyMesh\blockMeshDict

```

/*----- C++ -----*/
|=====|
| \ \ / F i e l d | OpenFOAM: The Open Source CFD Toolbox |
| \ \ / O p e r a t i o n | Version: 2.3.0 |
5 | \ \ / A n d | Web: www.OpenFOAM.org |
| \ \ / M a n i p u l a t i o n |
/*-----*/
FoamFile
{
10   version      2.0;
    format      ascii;
    class      dictionary;
    object     blockMeshDict;
}
15 // * * * * *

convertToMeters 1;

vertices
20 (
    (-7.464571e-01 -2.897777e+00 0.000000e+00) //0
    (-7.464571e-01 -2.897777e+00 3.000000e-02) //1
    (3.000000e-02 -1.404037e-02 0.000000e+00) //2
    (3.000000e-02 -1.404037e-02 3.000000e-02) //3
25 (3.000000e-02 -1.396857e-02 0.000000e+00) //4
    (3.000000e-02 -1.396857e-02 3.000000e-02) //5
    (3.000000e-02 1.396857e-02 0.000000e+00) //6
    (3.000000e-02 1.396857e-02 3.000000e-02) //7
    (3.000000e-02 1.404037e-02 0.000000e+00) //8
30 (3.000000e-02 1.404037e-02 3.000000e-02) //9
    (-7.464571e-01 2.897777e+00 0.000000e+00) //10
    (-7.464571e-01 2.897777e+00 3.000000e-02) //11
    (6.000000e-01 -3.000000e+00 0.000000e+00) //12
    (6.000000e-01 -3.000000e+00 3.000000e-02) //13
35 (3.000000e-01 -7.152440e-05 0.000000e+00) //14
    (3.000000e-01 -7.152440e-05 3.000000e-02) //15
    (3.000000e-01 0.000000e+00 0.000000e+00) //16
    (3.000000e-01 0.000000e+00 3.000000e-02) //17
    (3.000000e-01 7.152434e-05 0.000000e+00) //18
40 (3.000000e-01 7.152434e-05 3.000000e-02) //19
    (6.000000e-01 3.000000e+00 0.000000e+00) //20
    (6.000000e-01 3.000000e+00 3.000000e-02) //21
    (3.000000e+00 -3.000000e+00 0.000000e+00) //22
    (3.000000e+00 -3.000000e+00 3.000000e-02) //23
45 (3.000000e+00 -3.540760e-04 0.000000e+00) //24
    (3.000000e+00 -3.540760e-04 3.000000e-02) //25
    (3.000000e+00 0.000000e+00 0.000000e+00) //26
    (3.000000e+00 0.000000e+00 3.000000e-02) //27
    (3.000000e+00 3.540760e-04 0.000000e+00) //28
50 (3.000000e+00 3.540760e-04 3.000000e-02) //29
    (3.000000e+00 3.000000e+00 0.000000e+00) //30
    (3.000000e+00 3.000000e+00 3.000000e-02) //31
);

55 blocks
(
    hex ( 4 6 8 2 5 7 9 3) (80 1 1) edgeGrading (1.000000e+00 1.000000e+00
1.000000e+00 1.000000e+00 1.000000e+00 1.000000e+00 1.000000e+00 1 1 1

```

```

1)
60   hex ( 2 14 16 4 3 15 17 5) (80 1 1) edgeGrading (8.000000e+00 8.000000e+00
8.000000e+00 8.000000e+00 1.000000e+00 1.000000e+00 1.000000e+00 1.000000e+00 1 1 1
1)
      hex ( 6 16 18 8 7 17 19 9) (80 1 1) edgeGrading (8.000000e+00 8.000000e+00
8.000000e+00 8.000000e+00 1.000000e+00 1.000000e+00 1.000000e+00 1.000000e+00 1 1 1
65 1)
      hex ( 2 8 10 0 3 9 11 1) (80 79 1) edgeGrading (1.000000e+00 -5.000000e+00
-5.000000e+00 1.000000e+00 3.851253e+03 3.851253e+03 3.851253e+03 3.851253e+03 1 1 1
1)
      hex ( 0 12 14 2 1 13 15 3) (80 79 1) edgeGrading (1.250000e-01 8.000000e+00
70 8.000000e+00 1.250000e-01 2.596557e-04 2.596557e-04 2.596557e-04 2.596557e-04 1 1 1
1)
      hex ( 12 22 24 14 13 23 25 15) (120 79 1) edgeGrading (8.000000e+00
8.000000e+00 8.000000e+00 8.000000e+00 2.596557e-04 1.298279e-03 1.298279e-03
2.596557e-04 1 1 1 1)
75   hex ( 14 24 26 16 15 25 27 17) (120 1 1) edgeGrading (8.000000e+00
8.000000e+00 8.000000e+00 8.000000e+00 1.000000e+00 1.000000e+00 1.000000e+00
1.000000e+00 1 1 1 1)
      hex ( 16 26 28 18 17 27 29 19) (120 1 1) edgeGrading (8.000000e+00
8.000000e+00 8.000000e+00 8.000000e+00 1.000000e+00 1.000000e+00 1.000000e+00
80 1.000000e+00 1 1 1 1)
      hex ( 18 28 30 20 19 29 31 21) (120 79 1) edgeGrading (8.000000e+00
8.000000e+00 8.000000e+00 8.000000e+00 3.851253e+03 7.702506e+02 7.702506e+02
3.851253e+03 1 1 1 1)
      hex ( 8 18 20 10 9 19 21 11) (80 79 1) edgeGrading (8.000000e+00 1.250000e-01
85 1.250000e-01 8.000000e+00 3.851253e+03 3.851253e+03 3.851253e+03 3.851253e+03 1 1 1
1)
    );

edges
90  (
    arc 0 10 (-3.000000e+00 0 0)
    arc 1 11 (-3.000000e+00 0 0.030000)
    polyLine 8 2 (
95      (2.919000e-02 1.390307e-02 0.000000e+00)
      ...
      (2.949012e-02 -1.395439e-02 0.000000e+00)
    )
    polyLine 6 4 (
100      (2.920200e-02 1.383328e-02 0.000000e+00)
      ...
      (2.950200e-02 -1.388458e-02 0.000000e+00)
    )
    polyLine 9 3 (
105      (2.919000e-02 1.390307e-02 3.000000e-02)
      ...
      (2.949012e-02 -1.395439e-02 3.000000e-02)
    )
    polyLine 7 5 (
110      (2.920200e-02 1.383328e-02 3.000000e-02)
      ...
      (2.950200e-02 -1.388458e-02 3.000000e-02)
    )
    polyLine 16 4 (
115      (2.971020e-01 -4.086749e-04 0.000000e+00)
      ...
      (3.010200e-02 -1.398559e-02 0.000000e+00)
    )
    polyLine 17 5 (
120      (2.971020e-01 -4.086749e-04 3.000000e-02)
      ...
      (3.010200e-02 -1.398559e-02 3.000000e-02)

```

```
)
polyLine 14 2 (
125   (2.971020e-01 -4.801824e-04 0.000000e+00)
      ...
      (3.010200e-02 -1.405739e-02 0.000000e+00)
)
polyLine 15 3 (
130   (2.971020e-01 -4.801824e-04 3.000000e-02)
      ...
      (3.010200e-02 -1.405739e-02 3.000000e-02)
)
polyLine 16 6 (
135   (2.971020e-01 4.086749e-04 0.000000e+00)
      ...
      (3.010200e-02 1.398559e-02 0.000000e+00)
)
polyLine 17 7 (
140   (2.971020e-01 4.086749e-04 3.000000e-02)
      ...
      (3.010200e-02 1.398559e-02 3.000000e-02)
)
polyLine 18 8 (
145   (2.971020e-01 4.801823e-04 0.000000e+00)
      ...
      (3.010200e-02 1.405738e-02 0.000000e+00)
)
polyLine 19 9 (
150   (2.971020e-01 4.801823e-04 3.000000e-02)
      ...
      (3.010200e-02 1.405738e-02 3.000000e-02)
)
polyLine 12 0 (
155   (2.700000e-01 -3.000000e+00 0.000000e+00)
      ...
      (-7.464571e-01 -2.897777e+00 0.000000e+00)
)
polyLine 13 1 (
160   (2.700000e-01 -3.000000e+00 3.000000e-02)
      ...
      (-7.464571e-01 -2.897777e+00 3.000000e-02)
)
polyLine 20 10 (
165   (2.700000e-01 3.000000e+00 0.000000e+00)
      ...
      (-7.464571e-01 2.897777e+00 0.000000e+00)
)
polyLine 21 11 (
170   (2.700000e-01 3.000000e+00 3.000000e-02)
      ...
      (-7.464571e-01 2.897777e+00 3.000000e-02)
)
);

175 patches
    (
      patch inlet
      (
180         (0 1 11 10)
      )
      patch topAndBottom
      (
        (10 11 21 20)
        (20 21 31 30)
      )
    )
  )
```

```
185         (0 1 13 12)
           (12 13 23 22)
        )
    patch outlet
    (
190         (22 23 25 24)
           (24 25 27 26)
           (26 27 29 28)
           (28 29 31 30)
        )
195    wall wing
    (
           (4 5 7 6)
           (4 5 17 16)
           (6 7 17 16)
200    )
    empty frontAndBack
    (
           (0 2 8 10)
           (1 3 9 11)
205         (2 4 6 8)
           (3 5 7 9)
           (0 12 14 2)
           (1 13 15 3)
           (2 14 16 4)
210         (3 15 17 5)
           (12 22 24 14)
           (13 23 25 15)
           (14 24 26 16)
           (15 25 27 17)
215         (16 26 28 18)
           (17 27 29 19)
           (18 28 30 20)
           (19 29 31 21)
           (6 16 18 8)
220         (7 17 19 9)
           (8 18 20 10)
           (9 19 21 11)
        )
    );
225    mergePatchPairs
    (
    );

// ***** //
```

## A.15 Contents of File \system\controlDict

```

/*-----* C++ *-----*\
|=====|
|  \ \ /  F i e l d      | OpenFOAM: The Open Source CFD Toolbox
|  \ \ /  O p e r a t i o n | Version:  2.3.0
5 |  \ \ /  A n d           | Web:      www.OpenFOAM.org
|  \ \ /  M a n i p u l a t i o n |
\*-----*/
FoamFile
{
10   version      2.0;
    format        ascii;
    class         dictionary;
    location      "system";
    object        controlDict;
15 }
// *****

application      rhoCentralFoam;

20 startFrom        startTime;

    startTime      0;

    stopAt         endTime;
25 endTime         4.925028;

    deltaT         0.000001;

30 writeControl    adjustableRunTime;

    writeInterval  0.001970;

    purgeWrite     0;
35 writeFormat     binary;

    writePrecision 6;

40 writeCompression uncompressed;

    timeFormat     fixed;

    timePrecision  6;
45 runTimeModifiable no;

// *****

```

## A.16 Contents of File `\system\decomposeParDict`

```
/*-----*- C++ -*-----*\
| ===== |
| \\      / F i e l d      | OpenFOAM: The Open Source CFD Toolbox
| \\      / O peration    | Version: 2.3.0
5 | \\      / A nd         | Web:      www.OpenFOAM.org
| \\      / M anipulation |
|-----*\
FoamFile
10 {
    version      2.0;
    format       ascii;
    class        dictionary;
    object       decomposeParDict;
15 }
// ***** //

numberOfSubdomains 4;

method          scotch;
20
// ***** //
```

## A.17 Contents of File `\system\fvSchemes`

```

/*-----*- C++ -*-----*\
| ===== |
| \\      / F i e l d      | OpenFOAM: The Open Source CFD Toolbox
| \\      / O peration    | Version:  2.3.0
5 | \\      / A nd          | Web:      www.OpenFOAM.org
| \\      / M anipulation |
\*-----*- C++ -*-----*\
FoamFile
{
10   version      2.0;
    format       ascii;
    class        dictionary;
    object       fvSchemes;
}
15 // ***** //
fluxScheme      Kurganov;

ddtSchemes
{
20   default backward;
}

gradSchemes
{
25   default      cellLimited leastSquares 1.0;
}

divSchemes
{
30   default      Gauss linear;
}

laplacianSchemes
{
35   default      Gauss linear corrected;
}

interpolationSchemes
{
40   default      linear;
    interpolate(U) linear;
    reconstruct(rho) vanLeer;
    reconstruct(U) vanLeerV;
    reconstruct(T) vanLeer;
45 }

snGradSchemes
{
    default      corrected;
50 }

fluxRequired
{
    default      no;
55   p;
}

// ***** //

```

## A.18 Contents of File `\system\fvSolution`

```

/*----- C++ -----*\
|=====|
|  \ \ /  F i e l d      | OpenFOAM: The Open Source CFD Toolbox
|  \ \ /  O p e r a t i o n | Version:  2.3.0
5 |  \ \ /  A n d           | Web:       www.OpenFOAM.org
|  \ \ /  M a n i p u l a t i o n |
\*-----*\
FoamFile
{
10   version      2.0;
     format       ascii;
     class        dictionary;
     object       fvSolution;
}
15 // ***** //

solvers
{
20   "(rho|rhoU|rhoE)"
     {
         solver      diagonal;
     }

25   "(U|k|omega)"
     {
         solver      smoothSolver;
         smoother    GaussSeidel;
         nSweeps     2;
         tolerance   1e-09;
30     relTol       0;
     }

     h
     {
35     $U;
         tolerance   1e-10;
         relTol     0;
     }
}
40

relaxationFactors
{
45   h      0.25;
}

// ***** //

```

## A.19 Contents of File `\system\sampleDict`

```

/*-----* C++ *-----*\
|=====|
|  \ \ /  F i e l d      | OpenFOAM: The Open Source CFD Toolbox
|  \ \ /  O p e r a t i o n | Version:  2.3.0
5 |  \ \ /  A n d           | Web:      www.OpenFOAM.org
|  \ \ /  M a n i p u l a t i o n |
/*-----*\

FoamFile
10 {
    version      2.0;
    format       ascii;
    class        dictionary;
    location     system;
15    object      sampleDict;
}

// ***** //

20 surfaceFormat raw;

interpolationScheme cellPoint;

fields
25 (
    p
    wallShearStress
    rho
);
30
surfaces
(
    wall
35    {
        type      patch;
        patches   (wing);
    }
);
40 // ***** //

```

## **Appendix B**

### **Flow Visualization Animations**

This appendix lists the flow visualization animations that were provided with this thesis. All animations show the results of Case 2, for one the last azimuth of rotation. The files are available at the office of the thesis advisor.

1. Velocity vectors (case2\_velVectors.avi);
2. Streamlines and Mach contours (case2\_streamlines.avi);
3. Vorticity (case2\_vorticity.avi);
4. Pressure in colour (case2\_pressure\_colour.avi); and
5. Pressure (case2\_pressure.avi).